Titre: Title:	Transitional Flow Prediction in High Reynolds Flows Over Hydrofoils
Auteur: Author:	Shayan Amiri
Date:	2020
Type:	Mémoire ou thèse / Dissertation or Thesis
Référence: Citation:	Amiri, S. (2020). Transitional Flow Prediction in High Reynolds Flows Over Hydrofoils [Ph.D. thesis, Polytechnique Montréal]. PolyPublie. https://publications.polymtl.ca/5501/

POLYTECHNIQUE MONTRÉAL

affiliée à l'Université de Montréal

Transitional flow prediction in high Reynolds flows over hydrofoils

SHAYAN AMIRI

Département de Génie Mécanique

Thèse présentée en vue de l'obtention du diplôme de *Philosophiæ Doctor*

Génie Mécanique

Novembre 2020

POLYTECHNIQUE MONTRÉAL

affiliée à l'Université de Montréal

Cette thèse intitulée:

Transitional flow prediction in high Reynolds flows over hydrofoils

présentée par **Shayan AMIRI**

en vue de l'obtention du diplôme de *Philosophiae Doctor*

a été dûment acceptée par le jury d'examen constitué de :

Éric LAURENDEAU, président
François GUIBAULT, membre et directeur de recherche
Ricardo CAMARERO, membre et codirecteur de recherche
André GARON, membre
Marius PARASCHIVOIU, membre externe

DEDICATION

This dissertation is dedicated to my parents, who have always inspired and encouraged me through my life. I also dedicate this thesis to my love, Shayesteh, for all her supports and sacrifices.

ACKNOWLEDGEMENTS

I would like to express my deepest gratitude to my supervisor Professor François Guibault. It has been an honor pursuing my Ph.D. degree under his supervision. Your professionalism in research and continuous support, patience, advises and motivation during my Ph.D. career made you a great mentor for me.

I would like to take this opportunity to express my sincere gratitude to my co-supervisor, Professor Ricardo Camarero. I appreciate all your contributions of time, suggestions and advise during my Ph.D. study.

I gratefully acknowledge Dr. Christophe Devals for his contributions and providing valuable expertise and helps during my study. I warmly thank Dr. Julien Domierre for the helpful comments and suggestions.

Computations are made on the "Briarée" supercomputer from "Université de Montréal", managed by Calcul Québec and Compute Canada. The operation of this supercomputer is funded by the Canada Foundation for Innovation (CFI), the ministère de l'Économie, de la science et de l'innovation du Québec (MESI) and the Fonds de recherche du Québec - Nature et technologies (FRQ-NT).

RÉSUMÉ

Dans une turbine hydraulique, les aubes fixes et les aubes directrices fonctionnent dans un large éventail de conditions et peuvent rencontrer différents régimes d'écoulement, y compris une transition du régime laminaire au régime turbulente. Dans un écoulement en transition, les propriétés de l'écoulement changent par des mécanismes complexes qui provoquent un passage du comportement laminaire à des caractéristiques turbulentes d'écoulement chaotiques. De plus, ces composants peuvent être soumises à des fréquences d'excitation en raison des forces fluctuantes transversales à l'écoulement qui résultent du détachement de vortex asymétriques. Pour éviter toute situation destructrice due à ces fréquences d'excitation, il est important de prévoir l'effet du comportement de l'écoulement en transition sur les composants mécaniques de la turbine pour différentes conditions de fonctionnement. C'est un défi que les outils modernes tels que la dynamique des fluides computationnelle (CFD) peuvent relever, en donnant un aperçu complémentaire aux approches expérimentales du comportement de l'écoulement dans diverses conditions.

Cette thèse propose et évalue la mise en œuvre d'un modèle de turbulence de transition en couplant un modèle de transition avancé, $\gamma - \widetilde{Re}_{\theta t}$, avec le modèle de turbulence dynamiquement adapté SST-SAS pour capturer les caractéristiques des écoulements en transition et la fréquence de détachement sur le profil NACA0009. Le modèle de turbulence transitionnelle a été implémenté dans un code CFD open source basé sur des volumes finis, OpenFOAM. Le modèle mis en œuvre a d'abord été vérifié et validé pour différents écoulements en transition, y compris la transition naturelle et de dérivation sur une plaque plane. Les résultats numériques ont été comparés aux données expérimentales pour le calcul du coefficient de frottement et de l'intensité de la turbulence. Un très bon accord a été observé entre l'étude en cours et les données disponibles.

Le principal résultat de la présente étude était d'évaluer l'emplacement du début de la transition et la fréquence de détachement des tourbillons sur des profils bidimensionnels dans des écoulements visqueux à des nombres de Reynolds élevés. Les propriétés de l'écoulement telles que la fréquence de détachement et l'emplacement de début de la transition ont été évaluées pendant le processus de validation. En général, un très bon accord a été observé par rapport aux données expérimentales disponibles. Les résultats ont déterminé que la présente méthodologie a

pu améliorer la précision des simulations numériques par rapport à un modèle de transition similaire couplé au modèle de turbulence, SST.

Une large gamme de vitesses d'écoulement avec deux configurations de bord de fuite différentes a été évaluée pour étudier la réponse du modèle de turbulence de transition mis en œuvre sur la prédiction de la fréquence de détachement et l'emplacement du début de la transition en fonction de différentes conditions de fonctionnement et géométries. Les résultats montrent que le modèle mis en œuvre prédit une relation linéaire entre la vitesse d'entrée et la fréquence de détachement tandis que les données expérimentales montrent une relation quasi linéaire. Le modèle de turbulence transitionnelle mis en œuvre a également montré qu'il pouvait distinguer les couches laminaires, de transition laminaire-turbulente et les couches limites turbulentes. Un bon accord a été observé pour la prédiction de l'emplacement au début de la transition par rapport à l'expérience.

ABSTRACT

In hydraulic turbines, stay vanes and guide vanes operate in a wide range of conditions and could encounter different flow regimes including laminar to turbulent transition. In a transitional flow, the flow properties change through a complex procedure and whereby the laminar behavior of the flow transforms into chaotic turbulent characteristics. In addition, these turbine components can experience excitation frequencies due to the fluctuating forces transverse to the flow that result from asymmetric vortex shedding. To prevent any destructive situation due to these excitation frequencies, it is important to predict the behavior of the transitional flow and its impact on the mechanical components of a hydraulic turbine in various operating conditions. This is a challenge that modern tools such as Computational Fluid Dynamics (CFD) can address by giving a complementary insight into the flow behavior under various conditions.

This thesis has proposed and evaluated the implementation of a transitional turbulence model by coupling an advanced transitional model, $\gamma - \widetilde{Re}_{\theta t}$, with the dynamically adapted turbulence model SST-SAS to capture the transitional flow features and shedding frequency over a NACA0009 hydrofoil. The transitional turbulence model was implemented within an open-source finite volume-based CFD code, OpenFOAM. The implemented model was first verified and validated with different transitional flows including natural and bypass transition over flat plate. Numerical results were compared to experimental data on calculation of friction coefficient and turbulence intensity. A very good agreement was observed between the current investigation and available data.

The main outcome of the current investigation was to investigate the transition onset location and shedding frequency of two-dimensional hydrofoils in URANS viscous flows at high Reynolds numbers. Flow properties such as shedding frequency and transition onset location were evaluated during the validation process. In general, very good agreement was observed compared to available experimental data. Results determined that the present methodology has been able to improve the accuracy of the numerical simulations compared to a similar transitional model coupled with the URANS turbulence model, SST.

A wide range of flow velocities for two different trailing edge configurations have been evaluated to investigate the response of the implemented transitional turbulence model on shedding frequency prediction and transition onset location with respect to different operating conditions

and geometries. Results show that the implemented model predicts a linear relationship between the inlet velocity and shedding frequency while, experimental data shows a quasi-linear relation. The implemented transitional turbulence model has also shown that it can distinguish laminar, laminar-turbulent transition and turbulent boundary layers. A good agreement has been observed for the prediction of the transition onset location compared to the experiments.

TABLE OF CONTENTS

LIST OF TABLES

LIST OF FIGURES

LIST OF SYMBOLS AND ABBREVIATIONS

α	Constant
β	Constant
BEP	Best efficiency point
c_{a1}	Constant
c_{a2}	Constant
c_{e1}	Constant
c_{e2}	Constant
C_f	Skin friction coefficient
Cl	Lift coefficient
CFD	Computational fluid dynamics
C_{ref}	Inlet reference velocity, m/s
$c_{\theta t}$	Constant
δ	Boundary layer thickness
δ_1	Displacement thickness
δ_2	Momentum thickness
DNS	Direct numerical simulation
ε	Dissipation rate of turbulence kinetic energy, m^2/s^3
f	Frequency, Hz
FFT	Fast Fourier transforms
γ	Intermittency
γ_{eff}	Effective intermittency
h	Body thickness, m
h_m	Maximum body thickness, m

H_{12}	Shape factor
κ	von Karman constant
k	Turbulence kinetic energy, m^2/s^2
λ_θ	Pressure gradient number
$L_{v\kappa}$	von Karman length scale
LES	Large eddy simulation
μ	Dynamic viscosity, $Pa.s$
μ_t	Turbulent viscosity,
ν	Kinematic viscosity, m^2/s
Ω	Vorticity magnitude, $1/s$
ω	Specific turbulence dissipation rate, $1/s$
PDE	Partial differential equations
ρ	Density, kg/m^3
RANS	Reynolds averaged Navier-Stokes
Re	Reynolds number
$Re_{\theta t}$	Transition onset momentum thickness Reynolds number
$\widetilde{Re}_{\theta t}$	Local transition onset momentum thickness Reynolds number
$Re_{\theta c}$	Critical momentum thickness Reynolds number
Re_v	Vorticity Reynolds number
R_ω	Dimensionless parameter
R_T	Viscosity ratio
R_y	Wall-distance-based turbulent Reynolds number
S	Absolute value of strain rate
s_1	Constant

SAS	Scale adaptive simulation
SST	Shear stress transport
St	Strouhal number
σ_f	Constant
σ_ω	Constant
$\sigma_{\omega 2}$	Constant
σ_ϕ	Constant
$\sigma_{\theta t}$	Constant
τ_w	Wall shear stress, N/m^2
θ	Momentum thickness
TE	Trailing edge
Tu	Turbulence intensity
U	Free-stream velocity, m/s
U_τ	Friction velocity, m/s
U^+	Dimensionless velocity
y^+	Dimensionless distance
ζ_2	Constant

LIST OF APPENDICES

CHAPTER 1 INTRODUCTION

This chapter describes fundamental concepts of flows in hydraulic turbines. It introduces the problematic that hydraulic turbine components, such as stay vanes and guide vanes, can encounter during various flow regimes. Different numerical approaches are discussed, including methods that have the potential to capture laminar to turbulent transitional flow characteristics. The goal of the current thesis as well as its structure are also described.

1.1 Hydroelectric turbines

A hydraulic turbine converts potential and kinetic energy of a flow into mechanical energy through runner rotation under the dynamic action of water. The design of a water turbine is mainly based on the available water head on the machine, the specific speed of the turbine and the quantity of water that can be utilized for continuous power generation.

Francis and Kaplan turbines are considered the two most important types of reaction turbines. In these turbines, power is generated by taking advantage of velocity and pressure variation through the reaction of the fluid on the rotating component of the turbine. Due to its very high efficiency for a wide range of operating conditions, Francis turbines are most often selected as the heart of hydroelectric power generation stations.

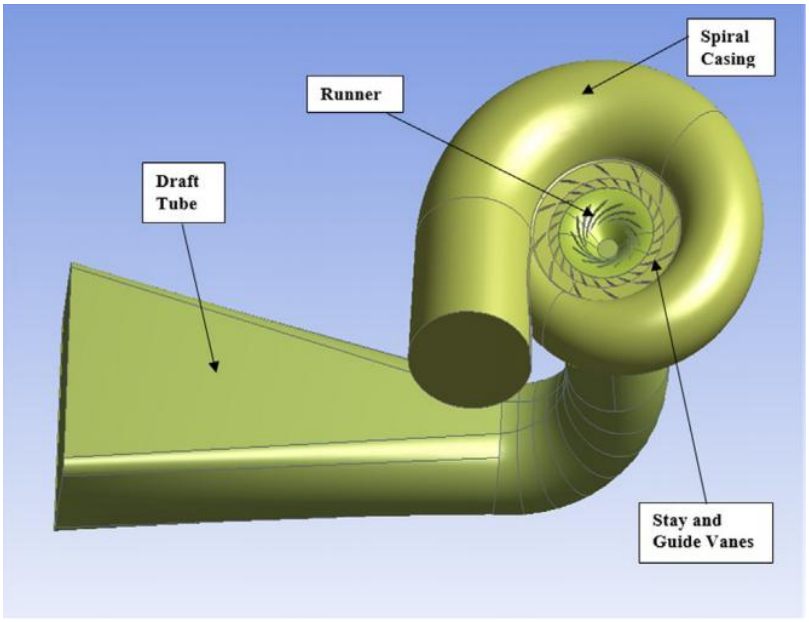

Figure 1.1 Scheme of Francis turbine (Aslam Noon & Kim, 2017)

A Francis turbine consists of five main components; spiral casing, stay vanes, guide vanes, runner and draft tube (see Figure 1.1). The water stored behind the dam is directed toward the spiral casing through the penstock, a pipeline leading to the turbine from the high-altitude reservoir. In the spiral casing, the axial flow is transformed into radial flow and then distributed uniformly through the stay vanes.

The guide vanes control the flow rate and angular momentum by adjusting the inlet area and angle of attack. The runner spins in reaction to the torque exerted by the incoming water on the runner blades. The mechanical energy is converted to electrical power through the runner shaft connected to the generator. The draft tube is the connection between the runner exit and lower reservoir. It reduces the kinetic energy of the discharged water by converting it to potential energy, to maximize the effective head of the turbine.

1.2 Problematic

The Best Efficiency Point (BEP) is defined as the point at which the turbine operates at its highest or optimum working efficiency. When a turbine operates under a mass flow rate conditions greater than or less than that of the BEP, it is called an off-design operating condition. These conditions may occur due to significant changes in flow rate or water head and also during turbine start-up or shut-down, which can change the physics of the flow, greatly impact the machine performance and lead to recurring maintenance issues (Goyal & Gandhi, 2018; Trivedi, 2015; Zhang, Liu, Xian, & Du, 2018). Damage in any part of a hydraulic turbine is dangerous from safety and maintenance perspectives, and also expensive to repair. Moreover, repairing leads to considerable loss of power generation, which represents direct economic losses for the operator.

Stay vanes and guide vanes operate in a wide range of conditions and are subjected to different flow regimes, including laminar to turbulent transition. Transitional flow also has a considerable impact on the functioning of various other types of mechanical devices such as airplane wings, hydraulic blades and wind turbines. This flow type has been a major focus in different studies, either theoretical, experimental or computational during the last decades (Sheng, 2016). In a transitional flow, the flow properties change through a complex process and cause the laminar behavior of the flow to transform and display chaotic turbulent characteristics. In the transition

process, boundary layer region and free stream flow interact with different linear and nonlinear dynamics. It also comprises broad flow time and length scales (Sheng, 2016). As a result, it is important to predict the behavior of transitional flows on the mechanical components. This can help the design process, improve the performance, and prevent any destructive situation.

Due to its complex nature, it is difficult to predict transitional mechanisms using current analytical methods. Although, experimental studies can provide a good perspective about flow mechanisms in transitional regions, they require expensive equipment. This is a challenge that modern tools such as Computational Fluid Dynamics (CFD) can address by giving a complementary insight into the flow behavior under various conditions. The current CFD methods provide an alternative to complement costly experimental testing by using high performance supercomputers and massively parallel processors to simulate complex fluid flows.

1.3 CFD modeling

Classical CFD modeling suggests two options for capturing very small as well as large-scale phenomena in complex fluid flows. One approach is applying a high-fidelity CFD solution such as Large Eddy Simulation (LES) or Direct Numerical Simulation (DNS). In the past years, the interest to use these methods has increased due to improvement in parallel computation. Even though these methods present good accuracy in numerical computations, they encounter difficulties in specifying initial and boundary conditions as well as incurring very high computational costs at high Reynolds number, due to the fine meshes needed. The second possibility is using turbulence models in combination with Reynolds Averaged Navier-Stokes (RANS) approaches. These methods have some advantages related to the cost and solution time, especially for the computational modeling of industrial applications, because it is not necessary to have extremely fine meshes in the whole domain.

It is recognized that RANS based models are effective in resolving large-scale flow structures originating from strong internal forces (Gavrilov, Sentyabov, Dekterev, & Hanjalić, 2017). Numerous researches have been devoted to enhance sensitivity of these models to better predict fluctuating eddies by introducing additional turbulence scales to resolve flow features in the high frequency spectral region, e.g.: multi-scale models (Cadiou, Hanjalić, & Stawiarski, 2004), and scale-adaptive simulations (SAS) (Menter & Egorov, 2010). The SAS concept stemmed from the

introduction of the von Karman length-scale into the turbulence scale equation (Mehdizadeh, Foroutan, Vijayakumar, & Sadiki, 2014). The information that is delivered by the von Karman length-scale allows the SAS turbulence model to dynamically adapt and resolve flow structures. The formulation of the SAS model differs from those of the Shear Stress Transport (SST) turbulence model by the additional SAS source term in the transport equation for the turbulence eddy frequency.

Laminar to turbulent transition mechanism occurs as a natural phenomenon, which can include notable effects on the flow properties such as skin friction drag and flow separation. Accurate prediction of this phenomenon has been one of the major challenges and a very important subject within the CFD framework. Although recently developed turbulence models such as SAS have presented acceptable performance in predicting and resolving the unsteady wake flow structures, their performance mainly depends on the base URANS turbulence models close to the wall boundary. Consequently, these turbulence models are unable to resolve and capture the transitional flow properties inside the boundary layer, when they operate on the basis of a fully-turbulent flow (You & Kwon, 2013).

Many investigations have focused on numerical simulations of transitional flows using RANS methods (Langtry & Menter, 2009; Walters & Cokljat, 2008). One of the methods that has attracted much attention and has been used in a wide variety of transitional simulation studies is the two-equation local correlation-based model, introduced by (Langtry et al., 2004). It includes two transport equations, one for intermittency, γ, and the other for the transition onset momentum thickness Reynolds number, $\widetilde{Re}_{\theta t}$. This model is primarily defined to be coupled with the two-equation SST turbulence model. The transitional model was modified by Langtry and Menter (2009). Its functionality has been tested in general transitional flows such as natural and bypass transition and in several applications including turbo-machinery (Dick & Kubacki, 2017). The transitional model was then successfully integrated with the SST-SAS turbulence model by You and Kwon (You & Kwon, 2012, 2013). Their results showed that combination of the SST-SAS model with the $\gamma - \widetilde{Re}_{\theta t}$ transitional model could predict much higher force and frequencies for flow around a circular cylinder than those from the SST combined with the $\gamma - \widetilde{Re}_{\theta t}$ transitional model.

1.4 Research goal

Laminar to turbulent transition is a very local phenomenon that happens in the boundary layer. Special care must be taken for the spatial discretization including the boundary layer mesh, and mesh resolution in the core domain. Numerous computational methods and techniques have been developed and implemented to provide precise prediction of laminar to turbulence transitional features. However, to the best of the authors' knowledge, there is no available work specifying the effect of the SST-SAS turbulence model combined to the $\gamma - \widetilde{Re}_{\theta t}$ transitional model to capture the force and shedding frequencies and transition onset locations over hydrofoils with different trailing edges in high Reynolds unsteady transitional flows using open source software.

The first goal of this research is to implement and couple the $\gamma - \widetilde{Re}_{\theta t}$ with the SST-SAS turbulence model using the C++ based open source CFD software OpenFOAM. Different meshes as well as discretization of the divergence terms on the implemented model using a natural transition test case will be studied. The implemented model is also validated using different steady state transitional regimes such as natural and bypass transitions over a flat plate. The results are compared with available experimental data. Furthermore, the implemented model is used to study shedding frequency of unsteady transitional flows in a wide range of Reynolds number over a NACA0009 hydrofoil. Two different shapes of trailing edge have been tested using the implemented model. The accuracy of the implemented model is compared to experimental data, in order to investigate its effects on the prediction of transition onset location and shedding frequency.

1.5 Thesis structure

This thesis consists of six chapters. Following the current introductory chapter, Chapter 2 presents a literature review on boundary layers, transitional flows, mesh and discretization analysis, and turbulence and transitional models.

Chapter 3 provides a fundamental description of the turbulence models used and contains a mathematical definition of the transitional model. It also covers mesh convergence and scheme analysis evaluation as well as validation with experimental data. Chapter 4 encompasses details regarding validation of the implemented model with unsteady transitional flows over NACA0009 hydrofoils. Chapter 5 presents results and discussion about accuracy of the implemented model

for various geometrical and flow conditions over the hydrofoil. Finally, Chapter 6 presents the conclusions and summarizes the contributions of the thesis followed by some recommendations for future works.

CHAPTER 2 LITERATURE REVIEW

This chapter presents a brief description of flow-induced excitation mechanisms in hydraulic turbines. It includes a literature review of the boundary layer concept and describes different boundary layer mechanisms with a focus on transitional boundary layer flows. Various criteria of a CFD solution to capture a laminar to turbulent transition are also studied. It details the specific objectives of the current investigation.

2.1 Excitation mechanisms in hydroturbines

Vortices are typical flow features in hydraulic turbines that lead to numerous types of instabilities such as pressure fluctuations (T. Chen, Zhang, & Li, 2016; Zhang, Chen, Li, & Yu, 2017), undesirable noise (Shi, Xu, & Gong, 2008), vibration and cavitation (Zhang, Qian, Ji, & Wu, 2016), etc. In this section various sources of excitation in hydraulic turbine components are described.

2.1.1 Flow-induced excitation

Several types of mechanical responses may be induced by the action of transient flow on structural components of a turbine, which are broadly categorized as flow-induced excitation. It is one of the practical and important phenomena that commonly occur at off-design condition, which imply potentially destructive effects on the hydraulic turbine system. Various definitions are available for the description of this phenomenon in the reviews of Rockwell (1998), Bearman (1984), Williamson and Govardhan (2004), Anagnostopoulos (2003), Sarpkaya (2004) and Dorfler, Sick and Coutu (2013). In their book, Dorfler, Sick and Coutu (2013) have evaluated different factors and elements for the phenomenon.

Under-prediction of the excitation sources can cause considerable damage in a hydraulic system. Instability-induced excitation is initiated from the interaction of the solid body with the fluid flow. It imposes a force on the structure and is important to be predicted. Depending on the type and amplitude, the nature of the mechanisms that control the oscillations are described as: fluid-dynamic, fluid-elastic or fluid-resonant. In fluid-dynamic control, the oscillating load only depends on the fluid flow conditions. The other two cases can lead to resonating body or fluid oscillator, respectively. These resonating controls can be potentially intense and dangerous for

the system, because they intensify the oscillating force within a certain range of flow velocities (Ausoni, 2009) and (Naudascher & Rockwell, 1994).

2.1.2 Lock-in

Lock-in or frequency synchronization is described as the frequency where the oscillation frequency and vortex shedding frequency coincide with the natural frequency of the solid structure. A Lock-in condition can occur not only close to the natural frequency of the structure, but also over a wide range of free-stream velocities (Sarpkaya, 2004). Bearman (1984) explained that the velocity range for which the lock-in condition occurs is dependent on the amplitude of the oscillation. When displacement of the oscillator structure is large enough to coordinate with the vortices along the body span, solid structure motion rises into higher displacement amplitude. It results in a steady state oscillation where the wake frequency is controlled by the structure movement. The response amplitude can rise and potentially lead to intense cycle fatigue, significant noise, and early solid structure failure (Hoskoti, Misra, & Sucheendran, 2018).

Anagnostopoulos and Bearman (1992) carried out water based experiments to evaluate excitation frequency on a cylinder at small Reynolds number flows. It was found that there is a direct relation between Reynolds number and the excitation frequency. It was observed that shedding frequency synchronizes with the natural frequency of the cylinder by increasing the Reynolds number. This behavior continues until the flow stream reaches a large enough Reynolds number, where lock-off occurs, where cortex shedding and structure vibration are no longer synchronized.

Experimental investigation of flow over a hydrofoil with a truncated trailing edge in a wide range of uniform high Reynolds number was conducted by Ausoni (2009). Higher maximum velocity (tangential to the flow direction) was observed during lock-in condition compared to that for lock-off. In the case of lock-off, the vortex shedding presented strong instabilities and displacements normal to flow stream. A significant enhancement of vortex strength is also detected for lock-in condition. Zobeiri (2012) carried out an experimental investigation of vortex shedding dynamics in the wake of hydrofoils with truncated, oblique and Donaldson trailing edges. Zobeiri (2012) provided an analysis that can help optimize the trailing edge shape.

2.2 Boundary layer

Since Prandtl has introduced the concept of boundary layer, several studies have specifically concentrated on the topic (Squire, 1991). Identifying the boundary layer structures and how they contribute to the dynamics and development of the vortex streets have long been primary aspects of vortex shedding research (Bernard, 2013). Consequently, the combination will be explored in this section.

2.2.1 Concept of boundary layer

Generally, in a viscous fluid flow at a high Reynolds number on a solid surface, e.g.: a flat plate, river bed, or wall of a pipe, the motion of the fluid is retarded in a thin layer near the solid body due to the frictional forces. This thin layer is called a boundary layer where fluid velocity builds up from zero at the solid wall to the free stream velocity that corresponds to frictionless flow (Schlichting & Gersten, 1979; Weyburne, 2006).

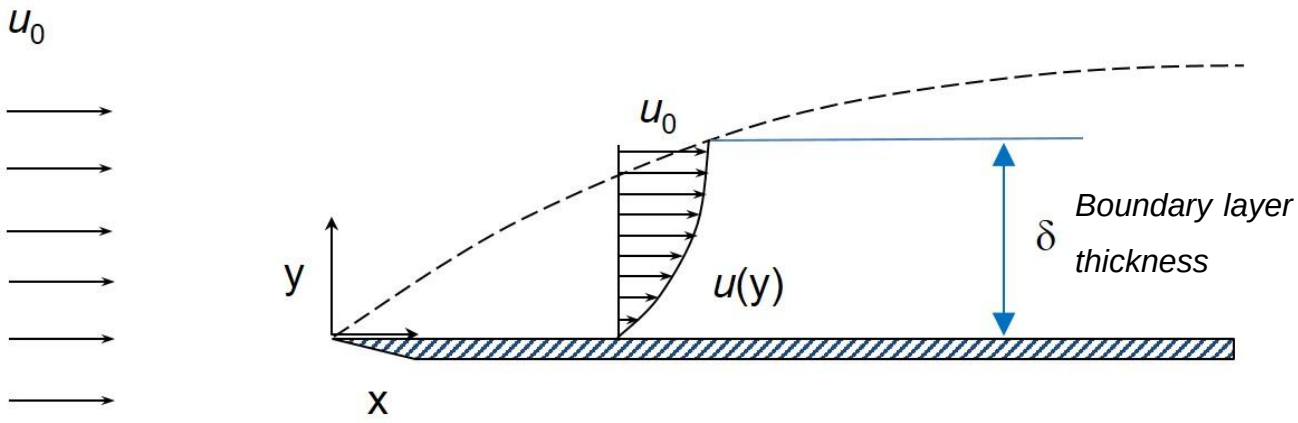

Figure 2.1 Scheme of boundary layer velocity profile (Weyburne, 2016)

The boundary layer thickness δ is typically defined as the distance along the boundary layer from the solid surface to a location where the flow speed reaches 99% of the free stream velocity.

Displacement thickness can provide a better measure of the hydrodynamic effect of the boundary layer. It stands for the distance by which the external free stream is shifted outward by the viscous flow velocity in the boundary layer. For an incompressible flow it is defined by,

$$\delta_1 = \int_0^{\delta} \left(1 - \frac{U_x}{U_{ref}}\right) dy \tag{2.1}$$

where U_x represents the tangential fluid velocity and U_{ref} is given as the free-stream velocity. The momentum thickness is then given as:

$$\delta_2 = \int_0^{\delta} \left(1 - \frac{U_x}{U_{ref}}\right) \frac{U_x}{U_{ref}} dy \tag{2.2}$$

The shape factor is usually employed to define the shape of the flow profile. It is derived using boundary layer displacement thickness and momentum thickness as:

$$H_{12} = \frac{\delta_1}{\delta_2} \tag{2.3}$$

Wall shear stress is described as the tangential force per unit area occurring between a flowing fluid and a solid surface. The magnitude is related to the gradient of the velocity close to the wall. The wall shear stress is given by,

$$\tau_w(x) = \mu \left(\frac{\partial U_x}{\partial y}\right)_w \tag{2.4}$$

2.2.2 Laminar boundary layer

Mathematical definition of the laminar boundary layer will generally result in differential equations. Although these equations can be solved numerically, analytical solution of the laminar flow is also available in specific conditions. For example, an incompressible flow over a flat plate at zero incidence and constant free stream velocity (see Figure 2.1) results in the analytical Blasius solution. In this case, over a specific range of Reynolds number, a simple boundary-layer flow is a uniform free stream velocity and considered as laminar, which comprises small velocity gradient and very low shear stress. The boundary-layer thickness increases monotonically with plate length (*x*) (Schlichting & Gersten, 1979).

2.2.3 Transient boundary layer

Transition is a sophisticated phenomenon that includes various mechanisms in different applications. Its nature is correlated to the origin of the turbulence phenomenon, which itself has a practical influence in understanding and design of engineering applications e.g.: aerospace, automobiles, hydraulic and wind turbines, ships, etc. Several comprehensive reviews on the

laminar to turbulent transition boundary layer have been conducted, (Dick & Kubacki, 2017; Kachanov, 1994; Reshotko, 2001; Schlichting & Gersten, 1979; Sheng, 2017). Even though there have been a great deal of studies identifying the laminar-turbulent transition types during the last decades, the mechanism is still under investigation.

The main mechanisms that are identified for laminar to turbulent transition in boundary layer flows maybe classified as Natural Transition, Bypass Transition and Separated-Flow Transition (Mayle, 1991; Walker, 1993). Wake-induced transition is also identified mostly in turbomachinery applications (Dick & Kubacki, 2017). Figure 2.2 presents the inception of instability in the boundary layer and the subsequent development of transitional flow into turbulence.

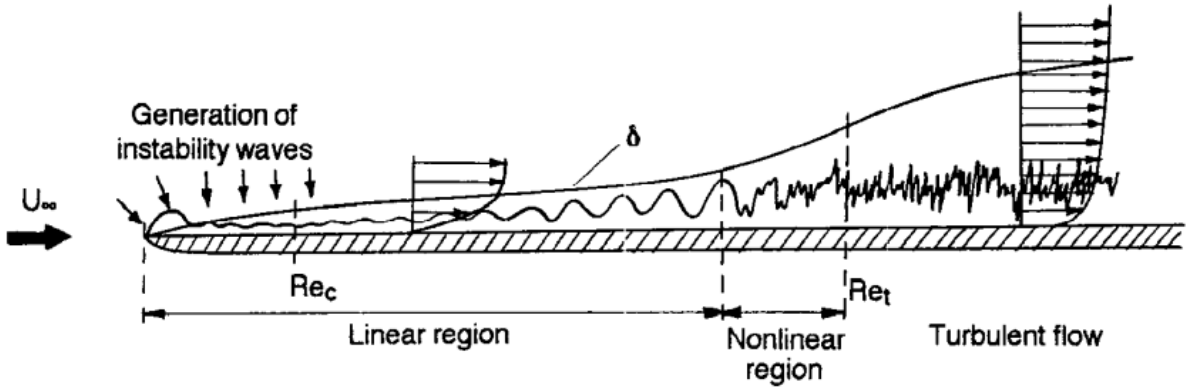

Figure 2.2 Scheme of the process of turbulence onset in a boundary layer (Kachanov, 1994)

- **Natural Transition**: It is usually detected at low levels of mean flow turbulence. This originates from the occurrence of two-dimensional viscosity dependent Tollmien-Schlichting instability waves in the laminar boundary layer. The next phase is the development of a three-dimensional instability which leads to the establishment of vorticity in the flow direction. This is followed by the inception of turbulent spots from regions of maximum shear. They ultimately merge to create a continuously turbulent flow. The natural transition process may interact with two-dimensional spatial and temporal disturbances (e.g.: surface roughness or free-stream instabilities) leading to perturbation of the boundary layer profile and changing the amplitude of the Tollmien-Schlichting wave (Dick & Kubacki, 2017; Mayle, 1991).

- **Bypass Transition**: It is described as the direct production of the streamwise disturbances in the boundary layer, which is a consequence of a high level of mean-flow turbulence in the free-stream. The disturbances are also called streaks or Klebanoff distortions (Zaki, 2013; Zaki & Durbin, 2005). The streaks result from deep penetration of low-frequency perturbations, whereas high-frequency perturbations are strongly damped by the laminar shear layer. In this transition type, the early 2D instability stage of the natural transition is bypassed but similar impacts may be prompted by specific sets of 3D surface roughness.
- **Separation-Induced Transition**: Transition can be initiated by inviscid Kelvin-Helmholtz instability of the laminar free shear layer, where the boundary layer is affected by laminar separation and low or moderate mean-flow turbulence levels. This leads to the production of span wise vortices. These span wise disturbances force the rotating vortices to be unstable and break as they flow downstream. This process takes place slowly and is sensitive to most types of perturbations under very low mean-flow turbulence. Many researchers have investigated the fundamentals and mechanisms of separation-induced transition, both experimentally and numerically (Lardeau, Leschziner, & Zaki, 2012; Medic, Zhang, Wang, Joo, & Sharma, 2016; Volino & Hultgren, 2000; Wheeler et al., 2016).
- **Wake-Induced Transition**: This type of transition is usually observed in turbomachinery applications. The transition happens due to wakes, which are generated around an earlier blade and transfers to the subsequent one in a blade row. Halstead et al. (Halstead et al., 1997a, 1997b, 1997c, 1997d) have conducted several tests on a wide range of Reynolds number aiming to capture the wake-induced transition in turbomachinery applications. The tested flows mostly included a strong level of turbulence intensity.

2.2.4 Turbulent boundary layer

In high Reynolds number flows, the stream-wise velocity profile of the boundary layer is distinguished by mixing of different scales of unsteady swirling flows or random eddies. Exchange of mass, momentum and energy that occur in a turbulent boundary layer are much greater than the ones in a laminar boundary layer due to a high level of mixing (Wilcox, 1994). As depicted in Figure 2.3, the velocity profile in the turbulent boundary layer is characterized by three main zones using dimensionless velocity U^+ and distance y^+.

The dimensionless velocity is given by,

$$U^+ = \frac{U_x}{U_\tau} \tag{2.5}$$

and dimensionless distance is defined as:

$$y^+ = \frac{yU_\tau}{\nu} \tag{2.6}$$

where ν is the kinematic viscosity of the fluid given by:

$$\nu = \frac{\rho}{\mu} \tag{2.7}$$

The friction velocity is defined using the wall shear stress τ_w as (Hink, 2015):

$$U_\tau = \sqrt{\frac{\tau_w}{\rho}} \tag{2.8}$$

According to Figure 2.3, the turbulent boundary layer consists of three main regions; the viscous sublayer, the log-law region and the defect layer.

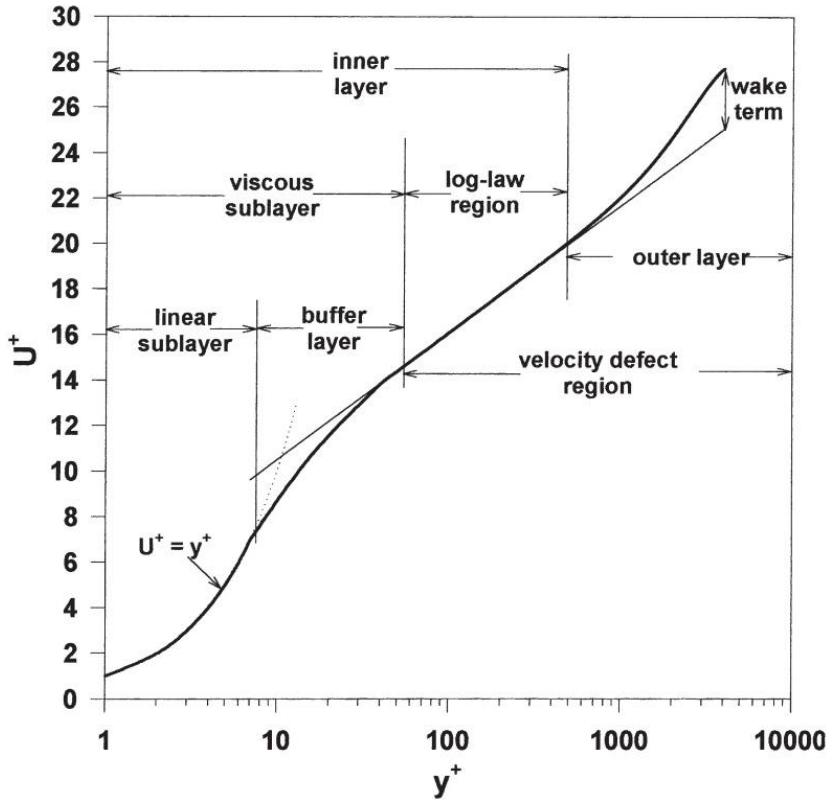

Figure 2.3 Velocity profile in a turbulent boundary layer including zones that make up the boundary layer (Schultz, Finlay, Callow, & Callow, 2003)

- **Viscous sublayer**

The viscous sublayer is described as the region between the wall and the log-law region, where the viscosity forces are dominant. Due to the no-slip boundary condition at the solid wall, there is a linear correlation between U^+ and y^+ for $y^+ < 5$ as:

$$U^+ = y^+ \tag{2.9}$$

The region where $5 < y^+ < 30$ is called buffer layer.

- **Log-law region**

In this region, the velocity follows a logarithmic profile with distance from the wall as (Marusic, Monty, Hultmark, & Smits, 2013):

$$U^+ = \frac{1}{\kappa}\log(y^+) + A \tag{2.10}$$

where κ represents the von Karman constant, and A is a parameter that relates to the surface roughness.

- **Defect layer**

The region that lies between the log-law zone and the edge of the boundary is known as the defect layer. The velocity profile presents a significant variation from the one in the log-law region (Coles, 1956).

2.3 Numerical modeling

During the last couple of decades, Computational Fluid Dynamics (CFD) tools have been developed and advanced in such a way that they can now be considered as a replacement for the table-look up and inflow model approach and costly experimental investigations (Bahrami, 2015). CFD analyses are conventionally employed to reach the following objectives (Castro, Ferretti, & Devinar, 2008):

- Prediction of hydraulic turbine efficiency in design and off-design conditions
- Modeling and understanding fluid flow phenomena such as unsteady vortex shedding, flow instabilities and cavitation that require specialized approaches due to their inherent complexity
- Accurately predicting transient pressure loading at the origin of fatigue

- Avoiding expensive empirical surveys in the laboratories or on sites.

A proper CFD tool can be chosen based on various criteria in each problem such as computational resources, time constraints, flow physics, accuracy, turbulence model, computational mesh, etc. In a numerical simulation, each criterion has its own value that should be evaluated and selected carefully.

2.3.1 Spatial discretization

One of the initial steps of a CFD simulation is to generate a valid mesh discretizing the fluid flow domain. An engineer has to find out what is the desired level of discretization to reach a mesh independent flow solution (Devals, Vu, Zhang, Dompierre, & Guibault, 2016; Schilling, 2009). There are several alternative techniques to generate grids in complex domains, however the most often used in three-dimensional CFD modeling of turbomachinery are based on tetrahedral or hexahedral volumes and/or combination of both of them. A grid that comprises mainly tetrahedral elements is normally known as an unstructured grid, whereas a structured grid consists of only hexahedral elements connected through an implicit connectivity. In addition, a mesh that includes both tetrahedral and hexahedral elements is referred to as a hybrid mesh (Choi et al., 2013; Kovenya, Cherny, Sharov, Karamyshev, & Lebedev, 2001).

2.3.1.1 Structured grid

Many practitioners of CFD in hydraulic turbine modeling rely on structured grids (Gong, Trivedi, Dahlhaug, & Nielsen, 2017; Magnan et al., 2014; Teran, Larrahondo, & Rodríguez, 2016). Gong et al. (2017) investigated global and local parameters of a high head Francis turbine using several geometrical and interface modeling approaches. Using hexahedral meshes, they studied mesh convergence on the computation of efficiency, torque, head and pressure of the turbine. The aim of the project was to figure out suitable plans for designers to simulate hydraulic turbines to balance the numerical accuracy and the requirement of computational resources. Sosa et al. (2015) generated a structured mesh for the draft tube domain using an in-house software named as draft tube mesher. The numerical analyses were based on the steady state condition of the turbine component flows for various opening angles of guide vanes and multiple modified draft tubes. The CFD solutions were validated using hydroelectric plant measurements.

Feng et al. (2014) employed hexahedral structured grids to analyze the resonance between the draft tube vortex frequency and the natural frequency of a prototype turbine under partial load conditions. In order to decrease the fluctuations of power output, various measures were investigated using CFD methods. The results were analyzed and validated to examine the effects on pressure fluctuations and vortex rope shape in the draft tube. Using structured hexahedral grids, pressure fluctuations due to the interaction of stationary and rotary components of a Francis turbine was studied by Schilling (2009). Stay vanes, guide vanes and runner blades were meshed using IDS software, while the spiral casing and the draft tube were discretized using the commercial code ICEM from ANSYS. Numerical results were compared with experimental data and showed that the transient simulations offer the possibility to predict pressure oscillations in a high-speed Francis turbine. Devals et al. (2016) conducted a mesh convergence study for turbulent flow in a hydraulic turbine draft tube using structured grids. Several parameters were investigated such as mesh distance and expansion factor from the wall, skin thickness, maximum mesh size in the core flow and global mesh resolution. Simulations were performed with the $k-\varepsilon$ turbulence model using wall functions, with a strict control of the y^+ and grid expansion factor from the wall boundary. They reached the conclusion that an acceptable mesh convergence could be reached with grid size beyond four million vertices. They also found that the skin thickness factor shows little effect on the draft-tube loss and the element size factor in the core domain presents considerable effects for full load and BEP, but not for part load conditions.

Fontanals et al. (2014) investigated boundary layer effect on the vortex shedding of a NACA0009 Donaldson-type hydrofoil using structured grids. Although the boundary layer profile along the trailing edge of the 2D hydrofoil chord was evaluated under lock-off conditions, they did not present any information regarding the boundary layer mesh characteristics. The numerical results were compared with available experimental data from Zobeiri (2012). The same hydrofoil but with a blunt trailing edge has been numerically investigated by Chen et al. (2018). They employed a fine hexahedral mesh (approximately 5.0 million elements) to simulate transitional flow on the hydrofoil with inlet velocity of 20 m/s. The mesh was designed to reach the average y^+ equal to 0.6 on the whole hydrofoil surface. The predicted transition process was validated by comparing the computed boundary layer velocity profiles, thicknesses and shape factors with the experimental data of Ausoni (2009).

2.3.1.2 Unstructured grid

It is recognized that generating a structured multi-block grid is a time-consuming task and requires a considerable level of expertise to obtain good quality meshes. The introduction of unstructured meshes in the turbomachinery modeling is often applied to complex geometries, where creating multi-block configuration grids can take time up to a month (Magnan et al., 2014; Tysell, 2010).

The main advantage of unstructured meshes is that the mesh generation process can be automated to a higher level than for multi-block meshes, which considerably reduces the grid generation time. Although using unstructured grids can lead to increase of computation time, the capability for this type of grid to provide efficient adaptive and locally refined grid is not negligible (Tysell, 2010). Several researchers have taken advantage of unstructured grids for the simulation of fluid flow in hydraulic turbines (Maruzewski et al., 2010; Menezes, 2016; Qian, Yang, & Huai, 2007; Saeed, 2015)

Large scale simulations of the flow-induced stresses in a Francis turbine runner were conducted by Saeed, Galybin and Popov (2010). Unstructured 3D tetrahedral meshing was used with the finite volume method. Mesh dependence analyses were carried out by refining the mesh. The entire computational mesh consisted of more than 2 million elements. It was found that the high stress zones are located at the trailing edge of the turbine runner. Designing a Francis turbine runner blade, Kocak, Karaaslan, Yucel and Arundas (2017) performed numerical simulations using unstructured tetrahedral grids. The mesh was generated using the ANSYS meshing tool. A single blade was designed using the Bovet design approach. Results showed that there was less than 1% difference between numerical computation and Bovet approach.

2.3.1.3 Hybrid grid

Hybrid meshes can combine the benefits of structured meshes for near-wall regions, where there is a need for highly stretched elements in the boundary layer to compute viscous effect, with easy mesh modification characteristics of unstructured meshes (Tysell, 2010). As discussed by Magnan et al. (2014), different good quality meshes can result in different flow solutions. In the mesh generation context, various parameters such as mesh size, distance of the first cell near wall

boundary (y^+ value), boundary layer mesh skin thickness, etc. influence the accuracy of the flow solution (Devals et al., 2016).

The rotor dynamic stability analysis of a Francis turbine has been conducted by (Gong, Wang, Liu, Shu, & Li, 2013) taking advantage of hybrid grids. The mesh was generated using the ICEM grid generator and grid independence was examined. The final mesh included 4.5×10^6 nodes. D'Agostini Neto and Saltara (2009) investigated the effect of 13 trailing edge geometries on a NACA64014A stay vane profile using hybrid grids. 2D simulations were conducted to determine characteristics of excitation forces for all geometries and their respective dynamic behaviors when simulated as a free-oscillating system. Vu et al. (2007) presented a CFD methodology to predict excitation frequency due to the von Karman vortex shedding on a NACA0009 stay vane by means of quasi-3D (with one element extrusion in the 3rd direction) transient computations. Even though a hybrid mesh was used for the numerical analysis aiming to have y^+ less than 1 due to the need of the SST turbulence model, they did not provide details regarding the mesh dependency of the solution for boundary layer and far field through the domain. They found that the precision was within ±18% without considering the lock-in effect. In addition, they showed that the effect of the lock-in contributes up to about ±15% of uncertainty.

2.3.1.4 Finite volume discretization

Different types of meshes such as structured and unstructured meshes can be used within the finite volume method framework. An extra degree of freedom shows up due to the way that we connect the control volumes to the grid. This affects the points location, where the function values are described (Hirsch, 2007). The two arrangements that are most common in the community within the control volume methods are a) cell-centered, b) vertex-centred. The earlier is the most popular approach and is used in the OpenFOAM solver (Moukalled, Mangani, & Darwish, 2016).

2.3.1.4.1 Cell-centered approach

The unknown variables are defined at the centers of grid cells or elements. Therefore, elements and discretization elements (control volumes) are identical. Generally, this approach is second order accurate and all the variables are calculated at the grid cells centroids, in which the difference between the unknown solution value and its average value is second order accurate.

This approach also gives the freedom to use general polygon elements without the requirement to define shape functions. One of its disadvantages relates to the manner it treats the skew elements, which affects its accuracy. The other shortcoming is linked to the way the diffusion term is discretized on non-orthogonal elements, which influences this approach's robustness. More details on the pros and cons of this approach were described by Moukalled et al. (2016) and Hirsch (2007).

2.3.1.4.2 Vertex-centered approach

In this approach, the unknowns are defined at the cell vertices or grid points, where the elements are created around the vertex location using a dual mesh and cells concept. There are two main methods for dual mesh construction. In two-dimensional space, one method is to join the centers of the cells, which have a shared vertex. The other method is to connect the centers of the elements with a shared point to the center of their faces. These processes can also be adapted in three-dimensional space.

The vertex-centered approach allows that unknown variables be computed using shape function or interpolation profiles. The face fluxes are presented with an accurate resolution for different mesh structures; however, it could include lower order accuracy for integrated values over an element due to the fact the vertices are not necessarily located at the elements' center. This approach also requires high storage since it creates a larger matrix. It could include residual storage at the solid wall boundaries, which induces a discrepancy and increases the discretization error compared to the cell-centered approach (Moukalled et al., 2016).

2.3.2 Temporal discretization

Solution time is one of the main challenges that transient simulations of hydraulic turbines has raised over the years. The goal is to reach an optimum solution time that is a compromise between the requirements for computational time and numerical accuracy (Gong et al., 2017).

To capture time dependent flow features, a time step analysis is normally conducted to ensure the accuracy of transient modeling (Tysell, 2010). Effect of the time step size on the vortex shedding frequency is studied by Vu et al. (2007). Their results indicated that a minimum time step of about 100 time-steps per vortex shedding period was needed to reach sufficient accuracy within 1% error using the ANSYS CFX solver. Fontanals et al. (2014) performed a time step sensitivity

analysis for modeling vortex shedding of transitional flow over a NACA0009 hydrofoil with Donaldson type trailing edge. They showed that a time step equal to 10^{-5} s is sufficient for transient modeling using backward Euler implicit scheme in ANSYS-FLUENT 13 solver.

In frequency analysis, the distribution of signal intensity with regards to frequency is investigated and normally presented as a frequency spectrum. This is while amplitudes are obtained by calculating values directly coming from the samples. Frequency is usually computed using the fast Fourier transform (FFT) of sampled time series of the signal (Dörfler et al., 2013).The shedding frequency is usually given in a non-dimensional form known as Strouhal number, St, equation 2.11.

$$St = \frac{fh}{U_{ref}} \tag{2.11}$$

where f is the shedding frequency, h is the body thickness and U_{ref} represents the free stream velocity.

Many researchers have used Fourier analysis for frequency studies in hydraulic turbine (D'Agostini Neto & Saltara, 2009; Feng et al., 2014; Fontanals et al., 2014; Gong et al., 2017; Laín, García, Quintero, & Orrego, 2013; Lee, Lee, & Suh, 2015b). Stoessel and Nilsson (2015) computationally modeled the flow in the scale model of a high-head Francis Turbine at part load and performed a Fourier analysis on transient simulations. Their results indicated a slight frequency shift compared to the experimental results.

2.3.3 Turbulence

Strong turbulent variations of velocity and pressure take place whenever considerable amounts of energy are dissipated. A principal feature of turbulent flow is its randomness. Whereas the details of turbulent stream are arbitrary and have chaotic nature, there are, yet, overall characteristics of the turbulence which may be defined in terms of probability. For instance, the distribution of sizes of eddies in the flow, variations of the kinetic energy, or the typical frequencies of flow fluctuations, may be evaluated on the basis of their occurrence probability (Dörfler et al., 2013). Due to the complex nature of turbulence, selection of a turbulence modeling approach is one of the essential features of CFD simulations, which has to be investigated.

2.3.3.1 Turbulence models

Computing solutions for a turbulent flow is not an easy task, due to its complex nature. Through the years, turbulence models have been developed and a proper one can be chosen based on the specifications related to each problem, such as physics, time constraint and computational resources. The governing equations for motion of incompressible viscous fluids are described by the Navier–Stokes equations, Eq. 2.12.

$$\frac{\partial u}{\partial t} + u.\nabla u - \nu\nabla^2 u = -\frac{1}{\rho}\nabla P + g \tag{2.12}$$

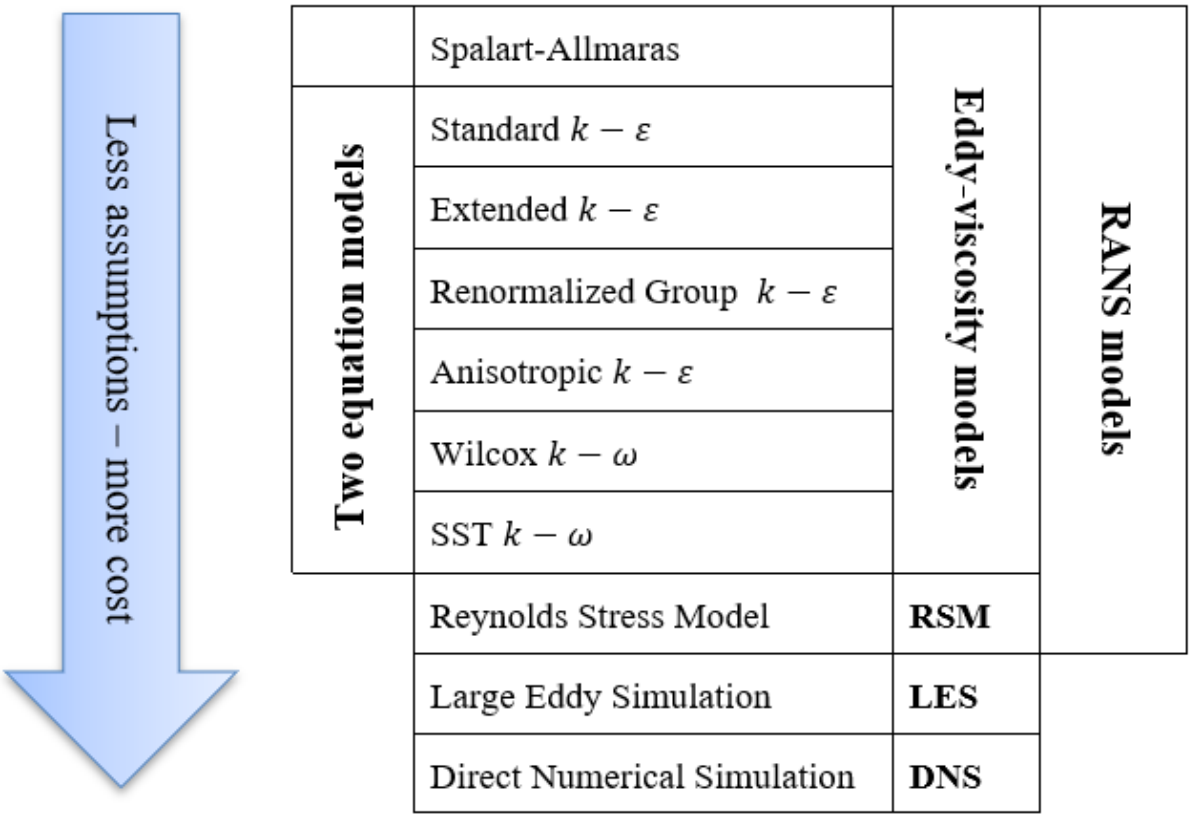

Figure 2.4 Turbulence approaches (Bahrami, 2015)

Solving the Navier-Stokes equations for complex geometries and high Reynolds flows using high resolution approaches (e.g.: Direct Numerical Simulation (DNS) or Large Eddy Simulation (LES)) requires extremely fine meshes to resolve very small flow features. This makes the DNS and LES approaches largely unfeasible because of their excessively high computational cost. The need for simple turbulence models such as algebraic or zero-equation has been significantly reduced, since the development of modern techniques to compute the partial differential

equations (PDE). Unsteady Reynolds Averaged Navier-Stokes (URANS) models emerged over the past decade as the most popular and cost-effective CFD framework in turbomachinery simulations (Gavrilov et al., 2017). Figure 2.4 sorted several turbulence models in terms of complexity and computational costs (Bahrami, 2015).

The SST model was developed by (Menter, 1994) as a compromise between the robustness and accuracy of the Wilcox $k-\omega$ model in the near wall region, and the advantage of the $k-\varepsilon$ model in the free stream region. It is able to account for the transport of the principal turbulent shear stress in adverse pressure gradient boundary layers. The standard equations of the SST model are as follows (Minakov, Platonov, Dekterev, Sentyabov, & Zakharov, 2015):

$$\frac{\partial(\rho k)}{\partial t}+\frac{\partial}{\partial x_j}\left(\rho u_j k\right)=\frac{\partial}{\partial x_j}\left(\Gamma_k \frac{\partial k}{\partial x_j}\right)+P_k-D_k \tag{2.13}$$

$$\frac{\partial(\rho \omega)}{\partial t}+\frac{\partial}{\partial x_j}\left(\rho u_j \omega\right)=\frac{\partial}{\partial x_j}\left(\Gamma_\omega \frac{\partial \omega}{\partial x_j}\right)+P_\omega-D_\omega+D_{SST} \tag{2.14}$$

where k represents the turbulent kinetic energy, D_k represents the dissipation of k, the term P_k defines the production of turbulent kinetic energy, ω denotes the specific dissipation rate, D_ω represents the dissipation of ω, P_ω denotes the production of ω, Γ_k and Γ_ω give the effective diffusivity of k and ω, respectively, and D_{SST} is the cross-diffusion term that blends the two turbulence models ($k-\varepsilon$ and $k-\omega$) together.

It is recognized that URANS models are effective in resolving large scale flow structures originating from strong internal forces, e.g.: vortex shedding, strong buoyancy or other body forces (Gavrilov et al., 2017). Several investigations have been devoted to increase sensitivity of the URANS models to detailed time variation of fluctuating eddies by introducing additional turbulence scales corresponding to higher frequency spectral region, e.g.: multi-scale models (Cadiou et al., 2004), and scale-adaptive simulations (SAS) (Menter & Egorov, 2010).

The SAS concept stemmed from the introduction of the von Karman length-scale into the turbulence scale equation (Mehdizadeh et al., 2014). The information that is delivered by the von Karman length-scale allows the SAS turbulence model to dynamically adapt and resolve flow structures in a URANS simulation. It approaches the LES solution, however does not involve spatial filtering and thus is not so strictly limited by the grid resolution as LES (Gavrilov et al., 2017). The SST-SAS model is a modified URANS formulation that introduces the second

derivative of velocity into the SST transport equations, which allows the resolution of the turbulent large scale in unstable flow conditions. The formulation of the SST-SAS model differs from those of the SST turbulence model by the additional SAS source term Q_{SAS} in the transport equation for the turbulence eddy frequency as given by:

$$\frac{\partial(\rho\omega)}{\partial t} + \nabla.(\rho U\omega) = \alpha\frac{\omega}{k}P_k - \rho\beta\omega^2 + Q_{SAS} + \nabla.[(\mu + \sigma_\omega\mu_t)\nabla\omega] + (1 - F_1)\frac{2\rho}{\sigma_{\omega 2}\omega}\nabla k\nabla\omega \quad (2.15)$$

α, β, σ_ω and $\sigma_{\omega 2}$ are constants, P_k describes the generation of turbulence energy, μ_t is the turbulent viscosity, μ denotes the viscosity, F_1 is a blending function and Q_{SAS} is given as (Egorov & Menter, 2008):

$$Q_{SAS} = max\left[\rho\zeta_2\kappa S^2\left(\frac{L}{L_{\upsilon\kappa}}\right)^2 - C\frac{2\rho k}{\sigma_\phi}\max\left(\frac{|\nabla\omega|^2}{\omega^2}, \frac{|\nabla k|^2}{k^2}\right), 0\right] \quad (2.16)$$

ζ_2, σ_ϕ, C and κ are constant values. The above equation contains the turbulent length scale L and the von Karman length scale $L_{\upsilon\kappa}$. According to Rotta's theory (Rotta, 1972), $L_{\upsilon\kappa}$ is defined through the second derivative of the velocity field:

$$L_{\upsilon\kappa} = \kappa\left|\frac{\bar{U}'}{\bar{U}''}\right| \quad (2.17)$$

$$\bar{U}'' = \sqrt{\frac{\partial^2\bar{U}_i}{\partial x_k^2}\frac{\partial^2\bar{U}_i}{\partial x_j^2}}, \qquad \bar{U}' = S = \sqrt{2S_{ij}S_{ij}}\,, \qquad S_{ij} = \frac{1}{2}\left(\frac{\partial\bar{U}_i}{\partial x_j} + \frac{\partial\bar{U}_j}{\partial x_i}\right) \quad (2.18)$$

This formulation reduces the turbulent viscosity and consequently enables the resolution of unsteady flow structures in numerical simulations. Compared to the SST turbulence model, small scale eddies can be produced and the turbulence cascade goes down to grid limit (Krappel, Ruprecht, & Riedelbauch, 2013).

Various numerical approaches for the flow modeling of a Francis turbine at part load operating point have been compared by (Krappel, Ruprecht, Riedelbauch, Jester-Zuerker, & Jung, 2014). Simulation results were obtained for the steady state approach with the SST model. Those results were contrasted with transient solutions using SST and SST-SAS turbulence models. The SST-SAS model was able to resolve the turbulent flow behavior in more details compared to the SST. The investigations included comparison of the flow losses in different components of a Francis turbine.

To analyze the gap flow effect, a four-blade propeller turbine was computationally studied in a full load operation point by Bernd and Riedelbauch (2015). For the transient solutions, two turbulence models of SST and SST-SAS were applied on a turbine with and without the existence of the runner gap. Results showed that a straight vortex rope developed downstream of the runner hub in the draft tube of the machine using the SST turbulence model. When applying the SST-SAS model, a vortex rope in the shape of a corkscrew was reassembling downstream the runner hub in the middle of the draft tube, which was not captured by the SST model.

Fontanals et al. (2014) conducted a numerical investigation on the NACA0009 hydrofoil with a Donaldson type trailing edge. They have examined four different turbulence models including SST, SST-SAS, Large Eddy Simulation (LES) and Detached Eddy Simulation (DES). The minimum difference on calculation of the shedding frequency between computational results and experimental data of Zobeiri (2012) was 18.9% and computed by the most expensive LES solution.

2.3.3.2 Near -wall treatment

In the near-wall regions, the fluid flow presents high inhomogeneity and anisotropy in the viscous sublayer close to the wall (Dreeben & Pope, 1997). However, the turbulent kinetic energy increases toward the outer section of the boundary layer region due to strong gradients in the flow velocity.

Flow variables present strong gradient close to the wall, where momentum and scalar transports parameters contain rapid changes. Modeling of a wall-bounded turbulent flow has been a major focus in computational fluid dynamics. Solid wall boundaries are the dominant source of turbulent flows and their modeling directly influence the fidelity of the computational solution.

The two main approaches that traditionally have been used for wall-bounded turbulent problems can be divided into; a) wall functions, b) near wall solution (Bredberg, 2000). The first approach does not characterize the complex details of the flow close to the wall boundary. This approach requires less computational resource, since it avoids resolving the strong gradients in the boundary layer. Wall functions are semi-empirical correlations, which are used to link the viscous region near the wall boundary to the fully turbulent outer region. There are several wall functions customized for the available turbulence models. In the case of near wall solutions, a refined mesh

all the way to the solid boundary is used to resolve the flow characteristics that appear near the wall.

The $k-\varepsilon$ and its branched models and the RSM model are basically valid for the flows inside the core region of a domain. Therefore, one might need to consider an appropriate approach for the solution near to the wall boundary. The Spalart-Allmaras, the $k-\omega$, SST, and SST-SAS turbulence models are defined to be used for boundary layer included flows, which require a sufficient grid resolution near the wall.

In the current thesis, a high-resolution mesh the near wall is used, with regard to the use of the SST and SST-SAS turbulence models to capture and resolve the flow characteristics near the wall boundary.

2.3.3.3 Transitional models

Due to the importance of the transition and its relation to the turbulence onset, remarkable efforts have been dedicated to the transition and turbulence investigation over the recent decades. With the current development of high-performance computing architectures and computational solution algorithms, numerical modeling and simulation have progressively become significant tools both in scientific investigations and technological designs in these fields. Attempts of various research teams have led to a series of transition modeling methods that can be applied in different engineering fields with acceptable accuracy (Sheng, 2017).

Approaches to predict the transition phenomenon can be divided into three main groups. The first group comprises methods that are based on the stability theory focusing on prediction of the natural transition. An example of this category is the e^N method that is introduced by Smith and Gamberoni (1956). The second group includes DNS and LES methods to calculate transition processes directly in order to avoid or minimize the utilization of turbulence closure models. Durbin, Jacobs and Wu (2002) developed a method to simulate bypass transition using DNS. Lee et al. (2015b) conducted numerical studies of vortex shedding from truncated and oblique trailing edges of 2D NACA0009 hydrofoil using the LES approach. They used a hybrid particle-mesh method and the vorticity-based sub-grid scale model to simulate transitional and wake flows.

Approaches in the third category are based on statistical modeling of RANS formulations aiming to capture bypass and separation-induced transitions. These methods include the majority of

transition modeling investigations in the CFD community today (Dick & Kubacki, 2017; Sheng, 2017). One of the main approaches that is developed under this category is the Local Correlation-based Transition method that is known as the $\gamma - \widetilde{Re}_{\theta t}$ model, developed by Menter et al. (2004) and extended by (Langtry & Menter, 2009). The $\gamma - \widetilde{Re}_{\theta t}$ model includes two equations; one for intermittency (γ), and another for transition momentum-thickness Reynolds number ($\widetilde{Re}_{\theta t}$). The $\gamma - \widetilde{Re}_{\theta t}$ model is not considered to satisfy the Galilean invariance. This limits the transitional model to be used for walls that are moving (Sheng, 2017). As boundary layer transition process is always relative to the domain walls, this is an issue when moving walls are used in a single computational domain (Langtry & Menter, 2009).

The formulation of the transitional model is not limited to one specific transition mechanism. It is designed to cover different mechanisms that are commonly encountered in industrial CFD simulations including bypass and natural transition (Langtry, 2006). Application of this method, which was first combined with the SST turbulence model, was tested in different engineering fields by Langtry et al. (2004). All simulations were computed using the ANSYS-CFX 5 solver.

Vu et al. (2007) used the SST turbulence model with the $\gamma - \widetilde{Re}_{\theta t}$ transition model to simulate the laminar-turbulence transition flow around a NACA0009 hydrofoil. They used the ANSYS-CFX 10 commercial solver for their analysis. Fontanals et al. (2014) have used the transitional model integrated with the SST turbulence model for shedding frequency analysis on the NACA0009 hydrofoil with a Donaldson type trailing edge. The computational simulations were performed using ANSYS-FLUENT 13. They compared the numerical results with other turbulence models such as SST, SST-SAS and LES. However, the minimum difference between computational model and experimental data on shedding frequency obtained by the LES method gave a 18.9% difference compared to the experiment. The $\gamma - \widetilde{Re}_{\theta t}$ transitional model was then successfully integrated with the SST-SAS turbulence model by (You & Kwon, 2012, 2013). Their results showed that the combination of the SST-SAS model with $\gamma - \widetilde{Re}_{\theta t}$ could predict much higher force and frequencies on a flow around a circular cylinder than those from the SST combined with $\gamma - \widetilde{Re}_{\theta t}$ model. The $\gamma - \widetilde{Re}_{\theta t}$ model was later combined with the one-equation Spalart-Allmaras turbulence model by (Wang & Sheng, 2014, 2015). Flow over a flat plate was used to calibrate the transition model, and series of 2D airfoil cases were numerically tested and compared to experiments. The skin friction profiles, transition onset location and the length of

transition for a wide range of Reynolds numbers and angles of attack were captured reasonably well. Solutions of a realistic helicopter rotor indicated that the transition model remarkably improved the prediction accuracy for the lift and drag coefficients.

Literature survey in this topic shows some progresses in finding the transitional flow features effects on shedding frequency calculation. However, there still lacks a knowledge on the influence of the combination of the most recent transitional turbulence models with cost-effective turbulence models on shedding frequency calculation.

2.3.4 Computational solver

Simulation of high Reynolds flows over hydraulic turbine components requires considerable computational resources. Solving a transient hydraulic problem takes a very long time using only one central processing unit (CPU). Computational power can be enhanced by using parallel processing and solving different portions of the numerical model on several CPUs, which will result in an increase of the computational speed. Commonly, utilization of a commercial software (e.g.: ANSYS-CFX, ANSYS-FLUENT, Siemens-Simcenter and Siemens-STARCCM+) for parallel processing solutions requires many licenses, which tend to be costly (Petit, 2012). However, commercial softwares provide some details about their implementation but they do not allow the user to have full control.

The OpenFOAM CFD tool is a C++ object-oriented based software, that will be used as the computational solver in the present work. It is released as an open-source software under GNU General Public License, and it can be used at no cost. The open-source structure also gives the opportunity to have complete control and insight into the code, which is necessary for scientific investigations. It is a very powerful tool for solving PDE's used in CFD (D'Alessandro, Binci, Montelpare, & Ricci, 2018). The OpenFOAM users community is growing each year by contributing to the implementation, development, verification and validation of the software (Petit, 2012). Review of the previous studies indicates that the OpenFOAM toolbox is as accurate as commercial softwares for various engineering fields (Eichhorn, Doujak, & Waldner, 2016; Geng, Yuan, Li, & Du, 2017; Stefan & Rudolf, 2015).

2.4 Summary

Transitional fluid flow modeling, specifically in turbomachinery, is an active field of research, for which a great deal of effort is needed to enhance flow prediction and help design engineers with accurate and robust simulation approaches. Different types of methods and models, which can be selected to analyze transitional fluid flow in hydraulic turbines, have been extensively investigated in the literature. For CFD study of the shedding frequency in transitional flows, particularly at high Reynolds number, the local properties of the boundary layer flows can have a strong effect on the excitation frequency. Hence, numerical methods should be able to accurately capture the boundary layer transitional features and satisfy the accuracy of the vortex shedding prediction, simultaneously.

According to the presented literature review, controlling the flow environment around a solid body for proper and cost-effective CFD simulations of the laminar to turbulent transition in high Reynolds flows is a necessity. This has immediate effects in accurate prediction of the transitional flow features. It appears that the integration of transitional models with the most recent turbulence models is still required. In this regard, the advanced $\gamma - \widetilde{Re}_{\theta t}$ transitional model will be investigated by integrating into the scale-adaptive turbulence model (SST-SAS) using the OpenFOAM open source CFD software.

- **Objectives**.

The goal of this research is to implement and couple the $\gamma - \widetilde{Re}_{\theta t}$ with the SST-SAS turbulence model using the C++ based open source CFD software and validate its capacity to predict transition flows over hydrofoils.

This leads to three specific objectives:

1. Investigation of scheme and convergence analysis and validation of the implemented transitional model using different transitional flows over a flat plate.
2. Investigate the effect of the implemented transitional model on shedding frequency prediction by comparing the results to experiments and numerical results using the $\gamma - \widetilde{Re}_{\theta t}$ model coupled with the SST turbulence model.

3. Demonstrate the successful implementation of the transitional model in capturing shedding frequency and transition onset location with different trailing edge geometries for a wide range of Reynolds numbers.

The first specific objective of this study is to investigate validation and verification of the implemented transitional model using different transitional flows over flat plate. The following phases are identified to accomplish this objective:

- Investigate the effect of discretization schemes on divergence terms and perform mesh convergence study using standard meshes.
- Perform validation of the implemented model using various experimental data of natural and bypass transition regimes over a flat plate.

The second objective is to investigate the effect of the implemented transitional model on shedding frequency prediction by comparing the results to experiments and numerical results using the $\gamma - \widetilde{Re}_{\theta t}$ model coupled with the SST turbulence model. The following phases are identified to accomplish the second objective:

- Investigate validation of the implemented model using available experimental data of flow over a NACA0009 hydrofoil.
- Compare results with numerical results of the $\gamma - \widetilde{Re}_{\theta t}$ model coupled with the SST turbulence model.
- Study mesh convergence of the implemented model and compare results with a similar transitional model coupled with SST model.

The third objective focuses on the investigation of the successful implementation of the transitional model in capturing shedding frequency and transition onset location for different trailing edge geometries and a wide range of Reynolds numbers:

- Compute the flow over a hydrofoil with a blunt trailing edge for a wide range of inlet velocities from 6 m/s to 28 m/s and compare to experimental data.
- Compute the flow over hydrofoil with an oblique trailing edge for inlet velocities from 6 m/s to 28 m/s and compare results with experimental data.

CHAPTER 3 MODEL DESCRIPTION, VERIFICATION AND VALIDATION

Numerous investigations have been recently conducted to decrease the limitations of the URANS models in industrial applications (e.g.: hybrid RANS/LES approach and second generation URANS models, such as the DES and SAS models). However, DES and SAS have demonstrated strong performance in terms of accuracy and capturing the transient vortex structures, which highly depends on the base URANS models close to the wall boundary. Consequently, those models are limited to appropriately resolve transitional structures underlying the boundary layer when the base models function in a fully-turbulent form (You & Kwon, 2013).

This chapter focuses on validation and verification of Local Correlation-based Transition Model combined with the SAS turbulence model for flows over a flat plate.

3.1 Local correlation-based transition model

Two statistical approaches are commonly used for transition prediction in engineering: one is the low-Reynolds number turbulence models and another, which is favored by industry, is the use of experimental correlations. Low-Reynolds models are based on transport equations, where the wall damping functions in the turbulence model prompt the transition process. Investigations show that this concept presents a lack of reliability for capturing influential parameters on transition phenomenon such as freestream turbulence, pressure gradients and separation, turbulent length scale and streamline curvature (Menter et al., 2004; Suzen, Huang, Hultgren, & Ashpis, 2003).

One of the most notable models under the correlation-based approach category is the Local Correlation-based Transition Model, also known as the $\gamma - \widetilde{Re}_{\theta t}$ model (Sheng, 2017). This model includes two transport equations. The first equation is for intermittency (γ), to trigger the transition process. Intermittency provides the probability for a given point in space to lie within the turbulent zone. It is the fraction of time that the flow is turbulent during the transition process. The range of the intermittency factor is defined between zero and one, with a zero value being the pre-transitional laminar stream and a value of one represents a fully turbulent flow. The second transport equation is defined in terms of the momentum thickness Reynolds number ($\widetilde{Re}_{\theta t}$). This

equation is formulated using experimental correlations that are based on freestream turbulence intensity or pressure gradient. This equation is essential for the sake of capturing the nonlocal effect of the turbulence intensity, which changes due to the alteration of velocity and decay of turbulence kinetic energy outside of the boundary layer (Menter et al., 2004).

3.1.1 Intermittency equation

The intermittency equation is given as:

$$\frac{\partial(\rho\gamma)}{\partial t}+\frac{\partial(\rho U_j\gamma)}{\partial x_j}=P_{\gamma1}-E_{\gamma1}+P_{\gamma2}-E_{\gamma2}+\frac{\partial}{\partial x_j}\left[\left(\mu+\frac{\mu_t}{\sigma_f}\right)\frac{\partial\gamma}{\partial x_j}\right] \tag{3.1}$$

The source terms for transition are:

$$P_{\gamma1}=F_{length}\rho S[\gamma F_{onset}]^{c_{a1}} \tag{3.2}$$

$$E_{\gamma1}=c_{e1}P_{\gamma1}\gamma \tag{3.3}$$

where S represents the magnitude of the strain rate. F_{length} is an empirical correlation that controls the length of the transition region (Langtry & Menter, 2009).

$$F_{length}=\begin{cases}398.189\times10^{-1}+(-119.270\times10^{-4})\widetilde{Re}_{\theta t}+(-132.567\times10^{-6})\widetilde{Re}_{\theta t}^{\,2}, & \widetilde{Re}_{\theta t}<400\\ 263.404+(-123.939\times10^{-2})\widetilde{Re}_{\theta t}+\left(194.548\times10^{-5}\right)\widetilde{Re}_{\theta t}^{\,2} & \\ \quad+(-101.695\times10^{-8})\widetilde{Re}_{\theta t}^{\,3}, & 400\le\widetilde{Re}_{\theta t}<596\\ 0.5-(\widetilde{Re}_{\theta t}-596.0)\times3.0\times10^{-4}, & 596\le\widetilde{Re}_{\theta t}<1200\\ 0.3188, & 1200\le\widetilde{Re}_{\theta t}\end{cases} \tag{3.4}$$

F_{onset} is a formulation to control the transition onset:

$$\begin{cases}Re_v=\frac{\rho y^2 S}{\mu}\\ F_{onset1}=\frac{Re_v}{2.193Re_{\theta c}}\end{cases} \tag{3.5}$$

$$F_{onset2}=min[\max(F_{onset1},F_{onset1}^4),2.0] \tag{3.6}$$

$$R_T = \frac{\rho k}{\mu \omega} \tag{3.7}$$

$$F_{onset3} = \max\left[1 - \left(\frac{R_T}{2.5}\right)^3, 0\right] \tag{3.8}$$

$$F_{onset} = \max(F_{onset2} - F_{onset3}, 0) \tag{3.9}$$

In high Reynolds flows, $\widetilde{Re}_{\theta t}$ will decrease to small values in the boundary layer, which will result in a local increase of the source term for the intermittency due to the relation between F_{length} and $\widetilde{Re}_{\theta t}$. This condition can be eliminated by bounding F_{length} to its maximum value in the viscous sublayer (Langtry & Menter, 2009).

$$F_{sublayer} = e^{-\left(\frac{R_\omega}{0.4}\right)^2} \tag{3.10}$$

$$R_\omega = \frac{\rho y^2 \omega}{500\mu} \tag{3.11}$$

$$F_{length} = F_{length}\left(1 - F_{sublayer}\right) + 40.0 \times F_{sublayer} \tag{3.12}$$

The modification to predict the separation induced transition is given by:

$$\gamma_{sep} = min\left(s_1\, max\left[0, \left(\frac{Re_v}{3.235 Re_{\theta c}}\right) - 1\right] F_{reattach}, 2\right) F_{\theta t} \tag{3.13}$$

$$F_{reattach} = e^{-\left(\frac{R_T}{20}\right)^4} \tag{3.14}$$

$$\gamma_{eff} = \max(\gamma, \gamma_{sep}) \tag{3.15}$$

where $s_1 = 2$.

$Re_{\theta c}$ in Eq. (3.5) is the critical Reynolds number that is connected to the transition Reynolds number using an empirical correlation:

$$Re_{\theta c} = \begin{cases} \widetilde{Re}_{\theta t} - 369.035 \times 10^{-2} + 120.656 \times 10^{-4}.\widetilde{Re}_{\theta t} - 868.23 \times 10^{-6}.\widetilde{Re}_{\theta t}{}^2 \\ \qquad +696.506 \times 10^{-9}.\widetilde{Re}_{\theta t}{}^3 - 174.105 \times 10^{-12}.\widetilde{Re}_{\theta t}{}^4, & \widetilde{Re}_{\theta t} \le 1870 \\ \widetilde{Re}_{\theta t} - \left(593.11 + \left(\widetilde{Re}_{\theta t} - 1870.0\right) \times 0.482\right), & \widetilde{Re}_{\theta t} > 1870 \end{cases} \tag{3.16}$$

The destruction/relaminarization sources are defined as follows:

$$P_{\gamma 2} = c_{a2} \rho \Omega \gamma F_{turb} \tag{3.17}$$

$$E_{\gamma 2} = c_{e2} P_{\gamma 2} \gamma \tag{3.18}$$

These terms are used to make sure that intermittency stays zero in the laminar boundary layer and also allow the model to predict relaminarization. Ω is the vorticity magnitude and F_{turb} is defined as:

$$F_{turb} = e^{-(R_T/4)^4} \tag{3.19}$$

The constants for the intermittency formulation are given as:

$$c_{e1} = 1.0; \quad c_{a1} = 0.5; \quad c_{a2} = 0.03; \quad c_{e2} = 50; \quad \sigma_f = 1.0 \tag{3.20}$$

Intermittency (γ) boundary condition at a wall boundary is equal to zero normal flux, whereas at an inlet γ is 1. Menter et al. (2004) suggested that the grid must be fine enough to have $y^+ \approx 1$ in order to properly capture the laminar and transitional boundary layers.

3.1.2 Momentum thickness Reynolds number equation

The transport equation for the transition momentum thickness Reynolds number, $\widetilde{Re}_{\theta t}$, is given by:

$$\frac{\partial(\rho \widetilde{Re}_{\theta t})}{\partial t} + \frac{\partial(\rho U_j \widetilde{Re}_{\theta t})}{\partial x_j} = P_{\theta t} + \frac{\partial}{\partial x_j}\left[\sigma_{\theta t}\left((\mu + \mu_t)\frac{\partial \widetilde{Re}_{\theta t}}{\partial x_j}\right)\right] \tag{3.21}$$

where the source term $P_{\theta t}$ is defined to force the transported scalar value of $\widetilde{Re}_{\theta t}$ to match the local value of $Re_{\theta t}$ (defined using empirical correlation) as:

$$P_{\theta t} = c_{\theta t}\frac{\rho}{t}\left(Re_{\theta t} - \widetilde{Re}_{\theta t}\right)(1.0 - F_{\theta t}) \tag{3.22}$$

and t is defined as:

$$t = \frac{500\mu}{\rho U^2} \tag{3.23}$$

$F_{\theta t}$ is a blending function, which turns off $P_{\theta t}$ in the boundary layer and allows $\widetilde{Re}_{\theta t}$ to diffuse in the free-stream region:

$$F_{\theta t} = min\left\{max\left[F_{wake}e^{-(y/\delta)^4}, 1 - \left(\frac{\gamma - 1/c_{e2}}{1 - 1/c_{e2}}\right)^2\right], 1.0\right\} \tag{3.24}$$

$$\begin{cases} \theta_{BL} = \frac{\widetilde{Re}_{\theta t}\mu}{\rho U} \\ \delta_{BL} = \frac{15}{2}\theta_{BL} \\ \delta = \frac{50\Omega y}{U}\delta_{BL} \end{cases} \quad (3.25)$$

$$Re_{\omega} = \frac{\rho \omega y^2}{\mu} \quad (3.26)$$

$$F_{wake} = e^{-\left[Re_{\omega}/(1\times10^5)\right]^2} \quad (3.27)$$

the constants are:

$$\sigma_{\theta t} = 2.0; \quad c_{\theta t} = 0.03 \quad (3.28)$$

The boundary condition for the transition momentum thickness Reynolds number ($\widetilde{Re}_{\theta t}$) at a wall is equal to zero flux and at an inlet should be calculated form empirical correlation which is related to the inlet turbulent intensity.

Transition onset is defined based on an empirical correlation as:

$$\lambda_{\theta} = \frac{\rho\theta^2}{\mu}\frac{dU}{ds} \quad (3.29)$$

$$Tu = 100\frac{\sqrt{2k/3}}{U} \quad (3.30)$$

$$U = (u^2 + v^2 + w^2)^{\frac{1}{2}} \quad (3.31)$$

$$\begin{cases} \frac{dU}{dx} = \frac{1}{2}(u^2+v^2+w^2)^{-\frac{1}{2}} \times \left[2u\frac{du}{dx} + 2v\frac{dv}{dx} + 2w\frac{dw}{dx}\right] \\ \frac{dU}{dy} = \frac{1}{2}(u^2+v^2+w^2)^{-\frac{1}{2}} \times \left[2u\frac{du}{dy} + 2v\frac{dv}{dy} + 2w\frac{dw}{dy}\right] \\ \frac{dU}{dz} = \frac{1}{2}(u^2+v^2+w^2)^{-\frac{1}{2}} \times \left[2u\frac{du}{dz} + 2v\frac{dv}{dz} + 2w\frac{dw}{dz}\right] \end{cases} \quad (3.32)$$

$$\frac{dU}{ds} = \left[(u/U)\frac{dU}{dx} + (v/U)\frac{dU}{dy} + (w/U)\frac{dU}{dz}\right] \quad (3.33)$$

All correlation-based models which are related to the properties of the local freestream velocity (turbulence intensity in this model) violate the Galilean invariance. One may point that the use of a streamline direction is not Galilean invariant and can be considered as a deficiency of this model. However, this is not problematic, as the correlations are described with reference to a wall boundary layer and velocities in all directions are consequently relative to the wall (Langtry & Menter, 2009).

The empirical correlation for transition onset momentum thickness Reynolds number is defined as follows:

$$Re_{\theta t} = \left[1173.51 - 589.428Tu + \frac{0.2196}{Tu^2}\right] F(\lambda_\theta) \quad Tu \leq 1.3 \tag{3.34}$$

$$Re_{\theta t} = 331.50[Tu - 0.5658]^{-.0671} F(\lambda_\theta) \qquad Tu > 1.3 \tag{3.35}$$

$$F(\lambda_\theta) = 1 - \left[-12.986\lambda_\theta - 123.66\lambda_\theta^2 - 405.689\lambda_\theta^3\right] e^{-\left[\frac{Tu}{1.5}\right]^{1.5}} \quad \lambda_\theta \leq 0 \tag{3.36}$$

$$F(\lambda_\theta) = 1 + 0.275\left[1 - e^{-[35.0\lambda_\theta]}\right] e^{-\left[\frac{Tu}{0.5}\right]} \quad \lambda_\theta > 0 \tag{3.37}$$

Parameters of the empirical correlations is limited to:

$$-0.1 \leq \lambda_\theta \leq 0.1, Tu \geq 0.027, Re_{\theta t} \geq 20 \tag{3.38}$$

With a minimum turbulence intensity of 0.027%, the largest resulting transition momentum thickness Reynolds number is 1450, which was observed over flat plate transitional flow experiments (Langtry & Menter, 2009). These values need to be adjusted where larger transition Reynolds number occurs such as on an aircraft in flight. The empirical correlation is utilized in Eq. (3.22) of the transport equation for $\widetilde{Re}_{\theta t}$. Equations (3.34-37) are computed iteratively due to having the momentum thickness θ_t in both left- and right-hand sides of the pressure gradient parameter, λ_θ. An initial guess for the local value of θ_t can be obtained with respect to the zero pressure gradient solutions of Eqs. (3.34) and (3.35) and the local value of the U, ρ and μ.

3.1.3 Coupling with the SST-SAS turbulence Model

The $\gamma - \widetilde{Re}_{\theta t}$ transition model was first calibrated in conjunction with the SST turbulence model (Menter et al., 2004).

$$\frac{\partial}{\partial t}\begin{bmatrix}\rho k \\ \rho\omega\end{bmatrix} + \frac{\partial}{\partial x_j}\begin{bmatrix}\rho u_j k \\ \rho u_j \omega\end{bmatrix} - \frac{\partial}{\partial x_j}\begin{bmatrix}(\mu + \sigma_k \mu_t)\frac{\partial k}{\partial x_j} \\ (\mu + \sigma_\omega \mu_t)\frac{\partial \omega}{\partial x_j}\end{bmatrix} = \begin{bmatrix}\bar{P}_k - \bar{D}_k \\ P_\omega - D_\omega + D_{SST}\end{bmatrix} \tag{3.39}$$

$$\bar{P}_k = \gamma_{eff} P_k; \qquad \bar{D}_k = \min(\max(\gamma_{eff}, 0.1), 1.0) D_k \tag{3.40}$$

$$R_y = \frac{\rho y \sqrt{k}}{\mu}; \qquad F_3 = e^{-\left(\frac{R_y}{120}\right)^8}; \qquad F_1 = \max(F_{1orig}, F_3) \tag{3.41}$$

The P_k and D_k terms represent the production and destruction terms of the turbulent kinetic energy equation in the original formulation of the SST model and γ_{eff} is the parameter computed from Eqs. (3.13-15). Eq. (3.41) uses a new relation for the blending function, where F_{1orig} indicates the original value of F_1 in the basic formulation of the SST turbulence model.

The $\gamma - \widetilde{Re}_{\theta t}$ transition model modifies the source terms of the transport equation for the turbulent kinetic energy equation, Eq. (3.40). Behaviour of the effective intermittency, γ_{eff}, is computed in such a way that it changes rapidly only close to the wall region but remains constant away from the solid boundary. In the current investigation, the transition model is coupled with the SST-SAS turbulence model. Similar to the transition model, the SST-SAS turbulence model is adopted based on the SST model, which includes an additional source term of Q_{SAS} in the transport equation of the specific dissipation rate. The additional source term in the SST-SAS model, Q_{SAS}, is usually triggered in the wake region and resolves the flow unsteadiness. Therefore, the location where the modification of the source terms for the turbulent kinetic energy due to the $\gamma - \widetilde{Re}_{\theta t}$ are activated is different from where the Q_{SAS} source term comes into calculation. Since the terms in the two models do not reduce each other's effect, these models can be applied in the same formulation simultaneously (You & Kwon, 2013). Hereafter, the implemented turbulence model will be named as SAS-Transition turbulence model.

3.2 Verification and validation

Writing a CFD program includes several components that should be taken into account. Independent to the complexity of the mathematical model (from simple potential flow up to full Navier-Stokes models) that one might select for a problem, different topics can be evaluated in terms of their effect on the convergence behavior, results accuracy, and computation time. These topics can be branched into (Hirsch, 2007):

- The grid type, mesh density, cell-centred or cell-vertex methods.
- The numerical scheme, including space and time (for transient problems) discretization.
- The boundary conditions and their implementation.
- The resolution method of the algebraic system and nonlinearities treatment.

Verification and validation are essential steps to make sure that a CFD code works properly as well as assessing the accuracy dependence with different mesh densities and with numerical schemes. Different definitions can be extracted for the concepts of verification and validation among standards and committees. According to Hirsch (2007), a simple and clear synthesis for the verification definition is:

"The process of determining that a model implementation accurately represents the underlying mathematical model and its solutions."

It specifies the steps that a CFD programmer uses to verify that an implemented mathematical approach is correctly programmed. It is extended to the comparison of the numerical solution with the exact and analytical solution or method of manufactured solution. It helps to evaluate the correctness and accuracy of the numerical discretization and grid dependency of the code. As part of verification, grid convergence order can be assessed. Grid convergence order includes the behavior of the numerical solution error, which is defined based on the calculated difference between the numerical and the exact solutions as:

$$e = F(h) - F_{exact} = Ch^p + H.O.T \tag{3.47}$$

where, F is the solution, h is some measure of grid spacing, C is a constant, and p is the order of grid convergence. There is no exact analytical solution available for the transitional solution at the current time.

Validation concept can be defined as:

"The process of determining the degree to which a model is an accurate representation of the real world from the perspective of the intended uses of the model." (Hirsch, 2007)

It is subjected to the comparison of the numerical solution with experimental data, which helps to evaluate the accuracy of the assumptions one might use to solve a physical problem.

In this context, (Noriega, Guibault, Reggio, & Magnan, 2018a, 2018b) presented a series of verification studies using OpenFOAM CFD solvers over different types of grids. They used a method of manufactured solution for Poisson's equation and an analytical solution for the Navier-Stokes equation and evaluated different schemes in the software. They assessed different Dirichlet and Neumann boundary conditions on several types of grids. They found that the non-orthogonal grids at the boundaries result in a degradation of convergence order from 2 to 1 near

boundaries in cases where skewed meshes were used near the boundary. However, the second order accuracy was maintained in the core of the domain. These verification results provide a basis upon which the present work is constructed. The addition of a transitional modal to the OpenFOAM framework proposed in the present research relies on the same numerical schemes and equations that were verified in the work of Noriega et al. (Noriega et al., 2018a, 2018b). These verification tests will therefore not be further pursued in the present work. The current study will instead attempt to complement the previous verification results.

To extent their investigation, the current study focuses on the application of the Navier-Stokes equations using the implemented transitional turbulence model to investigate accuracy of the implemented model within the OpenFOAM environment. Since, there is no analytical solution available, the current investigation presents a scheme analysis and a grid convergence study using series of standard verification meshes. In addition, experimental results from several transitional flows over flat plates and flow over hydrofoils are evaluated to assess the appropriateness of the implemented model.

3.3 Verification

The purpose of verification is to assert that the model is implemented correctly and that the equations are solved right for the chosen boundary conditions. Results are compared with theoretical values of friction coefficient within laminar and turbulent regions. In addition, experimental data from the Schubauer-Klebanoff flat plate natural transition test case was also used to investigate convergence behavior of the implemented model using different schemes and meshes for the transition region. In a subsequent section, the appropriateness of the model to simulate a given physical problem is established through validation by determining the accuracy of the implemented model compared to experiment. Different experimental cases including bypass and natural transitional flows are studied. Results of the current investigation for the friction coefficient and the turbulent intensity are compared with the available data.

A discretization scheme analysis and convergence investigation to find an appropriate configuration for the discretization scheme is performed in this section. A mesh convergence study is then performed over a 2D zero pressure gradient flat plate using available meshes from the NASA turbulence modeling resources (NASA, 2019). All results are provided for the

Schubauer-Klebanoff flat plate natural transition. The Schubauer-Klebanoff (1956) experimental investigations aimed to present a study on the flow behavior in a boundary layer during the transition process from laminar to turbulent over a flat plate with low freestream turbulence intensity, which was originally conducted in 1950's. The inlet flow properties for the Schubauer-Klebanoff test case are shown in Table 3.1. In the table, Tu is the inlet turbulence intensity and μ_t/μ is the inlet viscosity ratio. The inlet velocity is 50.1 m/s. Due to the low turbulent intensity, the transition behavior is mainly natural. Domain, mesh and boundary conditions of the numerical simulations are presented in Fig. 3.1. The average y^+ value is less than 1, in accordance with the transitional model requirement.

Table 3.1 Inlet flow properties for Schubauer-Klebanoff flat plate

Schubauer-Klebanoff	**Velocity (m/s)**	$\boldsymbol{Tu}$ **(%)**	$\boldsymbol{\mu_t/\mu}$
Experiment	50.1	0.03	1

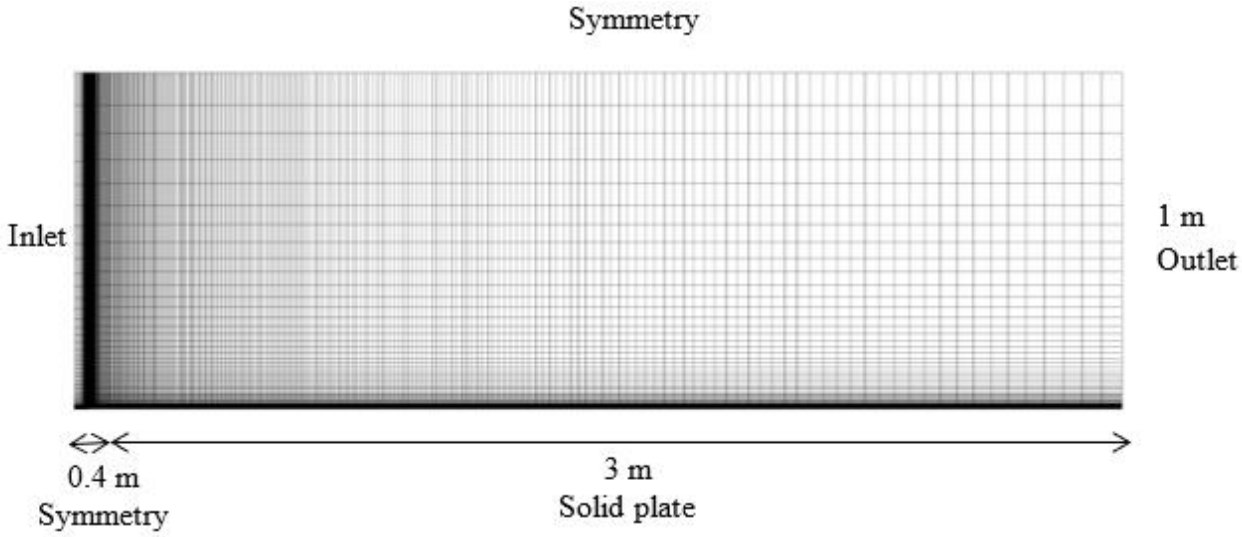

Figure 3.1 Domain and mesh for flat plate

3.3.1 Scheme analysis

First order upwind schemes are monotone. They include the flow direction properties and are appropriate to show the physical behavior of the flow given by (Moukalled et al., 2016):

$$\phi_f = \begin{cases} \phi_C \ \ if \ \ F \geq 0 \\ \phi_D \ \ if \ \ F < 0 \end{cases} \tag{3.42}$$

where ϕ is a general scalar property, f is the cell face, C represents the cell in question and D is the control volume to the downstream of C and F is the mass flow rates at the interface. However, the first order upwind scheme naturally introduces a high level of numerical diffusion due to its low order of accuracy. Still, understanding its behavior is important for numerical modeling as other discretization methods are based on it.

The ϕ value at face f for the second order upwind scheme is derived by interpolation at the cell face as:

$$\phi_f = \phi_C + \frac{\phi_C - \phi_U}{x_C - x_U}(x_f - x_C) \tag{3.43}$$

where C and U represent upstream and far upstream nodes, respectively. The second order upwind scheme is less diffusive and more accurate compared to the first order upwind scheme. However, it is expected to produce oscillatory results when used in high gradient flow regions (Moukalled et al., 2016).

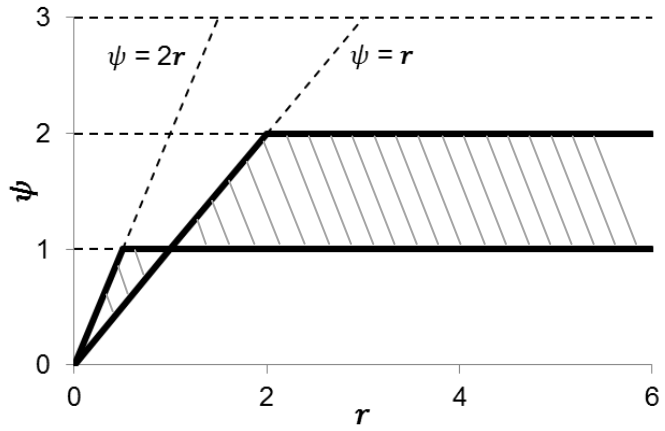

Figure 3.2 Regions of monotone and second order TVD scheme

Convection phenomena are modeled using a hyperbolic system of equations, which requires special treatment in their numerical modeling. With second order schemes, one might face wiggles in the numerical results (e.g. turbulent parameters such as k and ω) that can introduce negative unreal physical values and instability. This issue has been a major challenge in CFD history (Hirsch, 2007). To overcome it, nonlinear components known as limiters were proposed (Boris & Book, 1973; van Leer, 1973), even for very simple convection terms, which led to high

resolution schemes. High resolution schemes are monotone and second order accurate. It is suggested to use high resolution schemes for correlation-based transition models (Langtry, 2006).

Total Variation Diminishing (TVD) is one of the most notable high-resolution schemes. The general form for value at the cell face, ϕ_f, between the upstream node, C, and the downstream node, D, using TVD is presented as (Versteeg & Malalasekera, 2007):

$$\phi_f = \phi_C + \frac{1}{2}\psi(r)(\phi_D - \phi_C),\ r = \frac{\phi_C - \phi_U}{\phi_D - \phi_C} \tag{3.44}$$

where U is the upstream node to the C node and ψ is the limiter function with a nonnegative value to maintain the sign of the anti-diffusive flux.

Sweby (1984) has introduced the required conditions for a scheme to be considered as TVD based on the relation between limiter function, ψ, and ratio, r. The region for monotone and second order TVD schemes based on Sweby conditions are presented in Fig. 3.2 between the solid black lines.

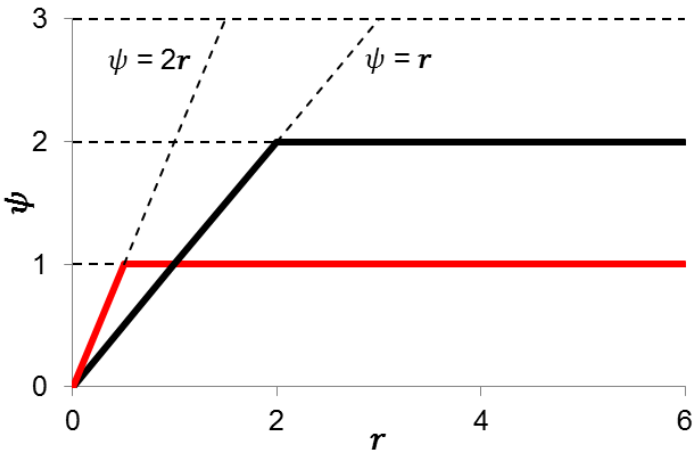

Figure 3.3 *limitedLinear* 1 on the Sweby diagram

The weak point of the limiters in TVD schemes is that they locally reduce the accuracy to first order. This is the price that has to be paid to suppress the oscillations; however, the first order schemes generally present a monotone solution. One of the TVD schemes available in OpenFOAM is *limitedLinear*. The limiter function for this scheme is defined as:

$$\psi(r) = \max\left(min\left(\frac{2r}{K}, 1\right), 0\right) \tag{3.45}$$

where K is a blending coefficient between 0 to 1. (Okuducu & Aral, 2018) studied the

performance of *limitedLinear 1*, meaning that $K = 1$, and compared to other second order schemes (i.e.: QUICK, MUSCL, second order upwind) using different type of meshes. They found that the *limitedLinear 1* scheme presents consistent results on different type of meshes. It is defined based on the central differencing method and limits the flux towards the first order upwind scheme in high gradient locations. Figure 3.3 shows the $r - \psi$ relation for the *limtedLinear 1* in Sweby diagram with a solid red line.

The following combination of discretization schemes are studied for convection terms of the velocity and turbulence parameters of k, ω, $\widetilde{Re}_\theta$ and γ over the Schubauer-Klebanoff (S-K) flat plate natural transition case:

I. First order upwind.
II. Second order upwind.
III. First order upwind for turbulence parameters and second order upwind for velocity.
IV. TVD *limitedLinear 1* for turbulence parameters and velocity.
V. TVD *limitedLinear 1* for turbulence parameters and second order upwind for velocity.

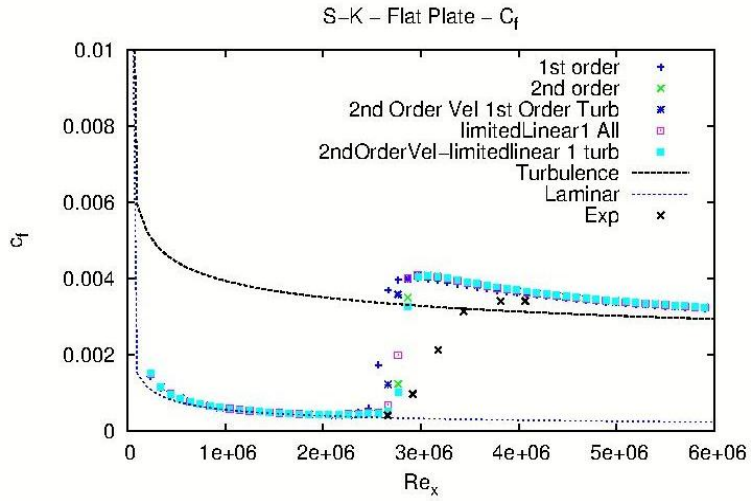

Figure 3.4 Scheme analysis over the S-K flat plate natural transition case

Fig. 3.4 shows the friction coefficient, C_f, results of different combinations for convection terms discretizations based on the local Reynolds number.

$$Re_x = \frac{\rho U x}{\mu} \tag{3.46}$$

where U is the reference velocity, ρ is density, μ is the viscosity and x is the distance from the leading edge of the flat plate.

When considering the transition onset location, higher order schemes generally produce more accurate results than the first order scheme. However, the difference between numerical results is low. With combinations I and III, where the first order upwind scheme was involved, an earlier transition onset location is predicted compared to other schemes that include only higher order schemes. Although the high order schemes predict a much closer value of the transition onset location with respect to experimental data, they show a sharp transition region, which does not reflect the smoother transition observed experimentally. This could be due to the mesh resolution, as will be shown in the mesh convergence study.

Combinations II, IV and V show closer values compared to the experiment on the prediction of the transition onset. However, the convergence of all schemes must be analyzed.

3.3.2 Convergence history

Convergence history of the considered schemes is now evaluated.

I. First order upwind

Convergence history of the first order upwind scheme used for the convection terms for velocity and all turbulence parameters is presented in Fig. 3.5. All the variables are converged to a residual below 10^{-5} and convergence behavior is monotonous for most variables.

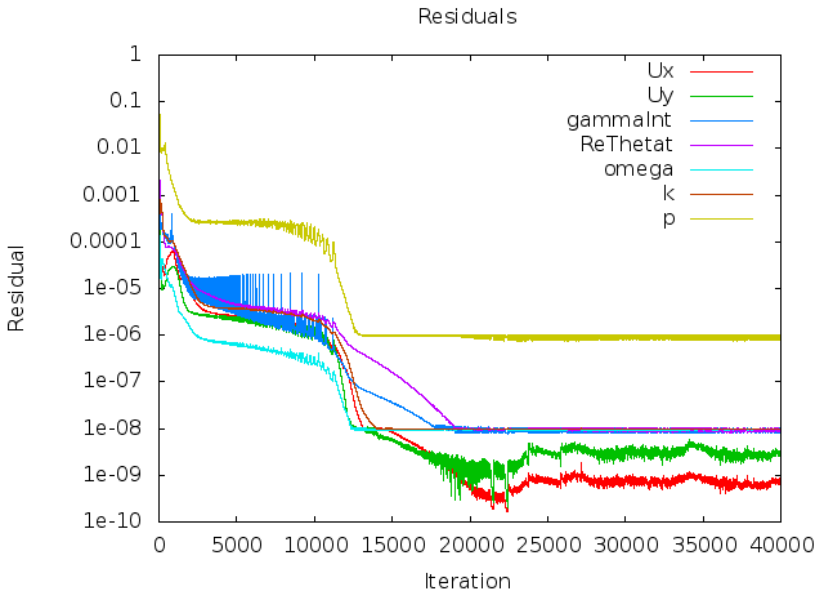

Figure 3.5 First order upwind for all variables

II. Second order for all variables

The convergence history of the second order upwind scheme used for the convection terms of velocity and all turbulence parameters is presented in Fig. 3.6. All variables show oscillatory residuals, which stay at higher values when compared to the first order upwind scheme.

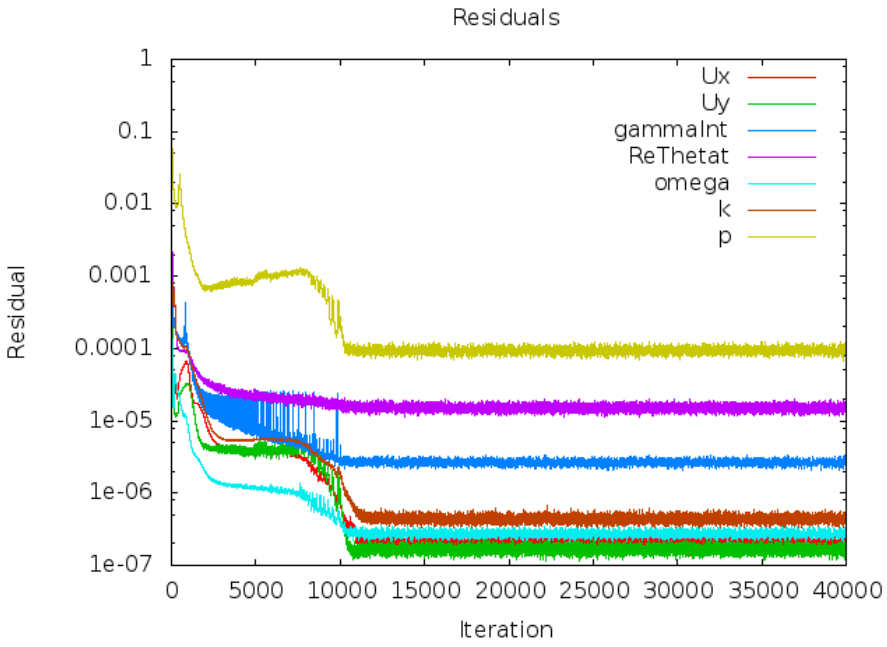

Figure 3.6 Second order upwind for all variables

The pressure residual converges roughly to 10^{-4} and Re_θ oscillates between 10^{-4} and 10^{-5}, while in the first order upwind all variables converged to residuals below 10^{-5}. This can be due to the negative unreal physical values that can introduce instability using second order schemes for turbulence equations, which generate wiggles in the solution.

III. First order turbulence and second order velocity

Figure 3.7 shows the convergence history of the combination of first order upwind for turbulence parameters and second order upwind for velocity convection terms. All variables converged to residuals below 10^{-5}.

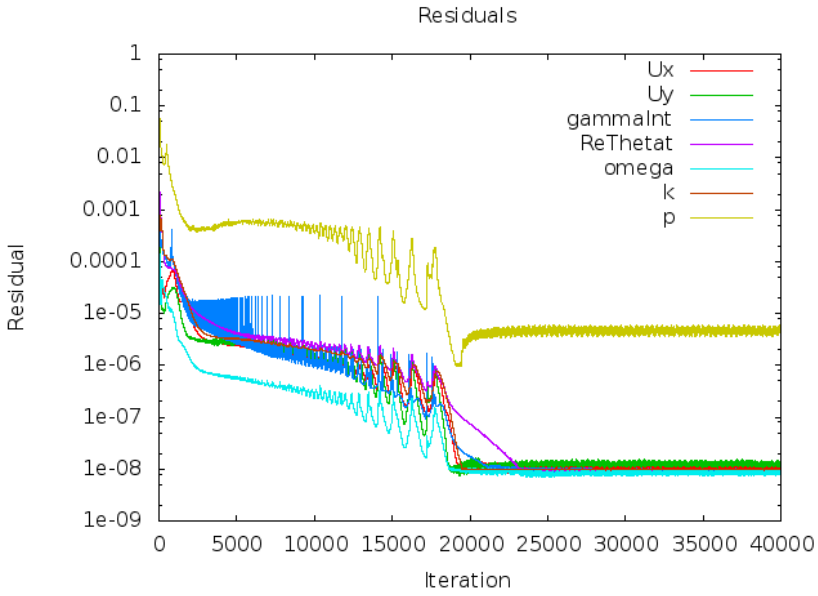

Figure 3.7 Second order turbulence and first order velocity

IV. TVD limited linear 1 for all variables

The convergence history of the *limitedLinear 1* scheme for all the convection terms of turbulence and velocity is presented in Fig. 3.8. As it shows, the residual is less oscillatory compared to other first and second order upwind schemes. However, the residuals remain at much higher values. For example, the pressure residual remains close to 10^{-3}.

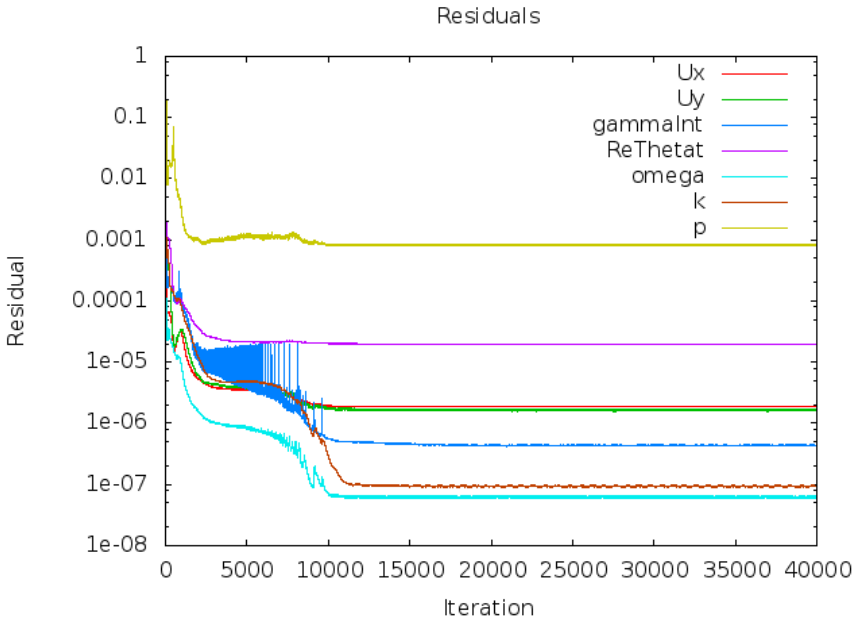

Figure 3.8 TVD *limitedlinear 1* for all variables

V. TVD *limitedLinear 1* for turbulence parameters and second order upwind for velocity

The convergence history of the *limitedLinear 1* TVD scheme for turbulence parameters and second order upwind for velocity is shown in Fig. 3.9. All the parameters are converged to 10^{-5}. The turbulence parameters are less oscillatory compared to the second order upwind scheme, Fig. 3.6, where pressure and Re_θ are not converged to 10^{-5}. The observation on convergence of this combination is in agreement with the suggestion of Langtry (2006) for using high resolution schemes for correlation-based transition models. Since all the parameters using this combination converged to 10^{-5} and it also presents better accuracy compared to other schemes, it will be used for further studies.

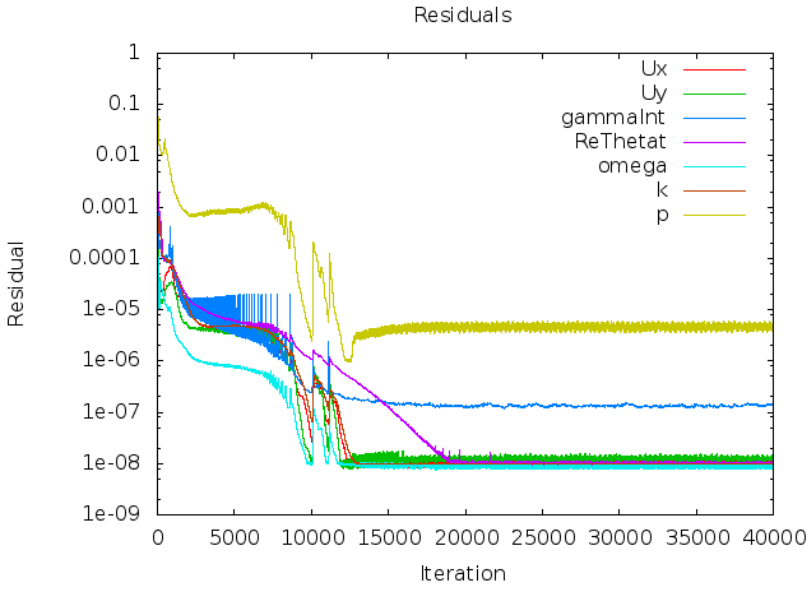

Figure 3.9 TVD *limitedLinear 1* for turbulence parameters and second order for velocity

3.3.3 Mesh convergence study

To perform a mesh convergence study in the this thesis, meshes available from the NASA turbulence modeling resource (NASA, 2019) for flat plate verification are used. It is aimed to investigate the capability of the current implementation on standard verification meshes. According to Langtry (2006), the correlation based transitional model can be sensitive to different grid discretization parameters including first cell height and number of cells in the tangential direction to the flow direction. The implemented transitional model requires special

grid treatment close to the wall boundary to capture the transitional flow physics in the boundary layer.

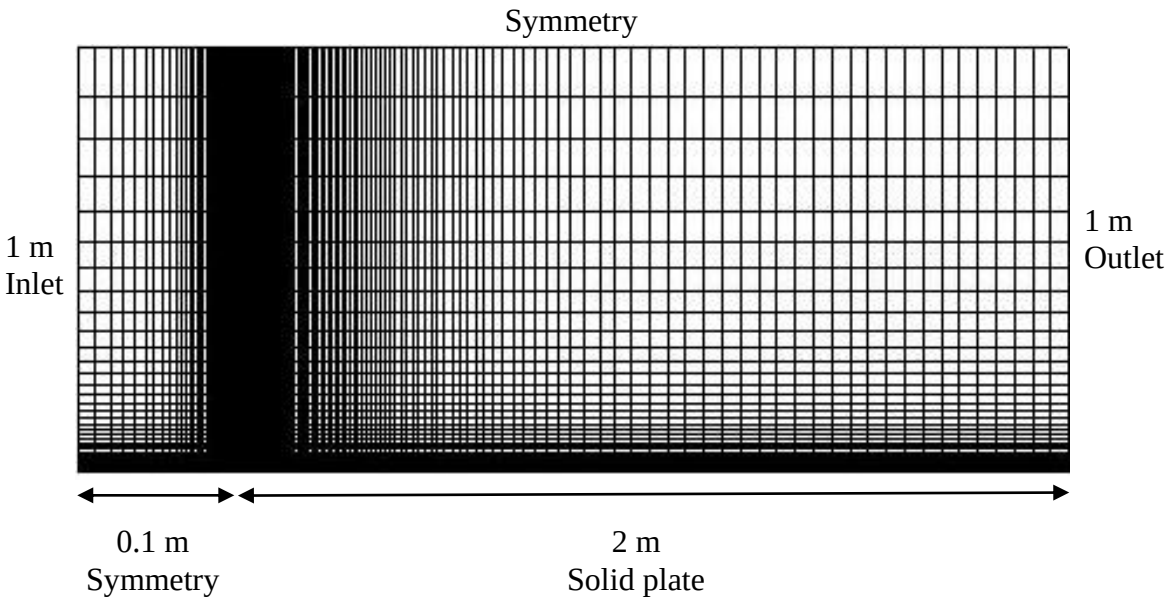

Figure 3.10 The domain for the NASA flat plate verification cases (mesh 2×137×97)

To investigate the mesh convergence over the implemented model, five different meshes from coarse to fine resolutions are tested. These grids are basically designed for analysis of 2D zero pressure gradient flat plate as a resource to verify the implemented CFD models. The domain for the NASA flat plate is shown in Fig. 3.10. The mesh properties are detailed in Table 3.2.

Table 3.2 Meshes from NASA turbulence modeling resource (NASA, 2019)

Mesh	Cells on the plate
2×35×25	29
2×69×49	57
2×137×97	113
2×273×193	225
2×545×385	449

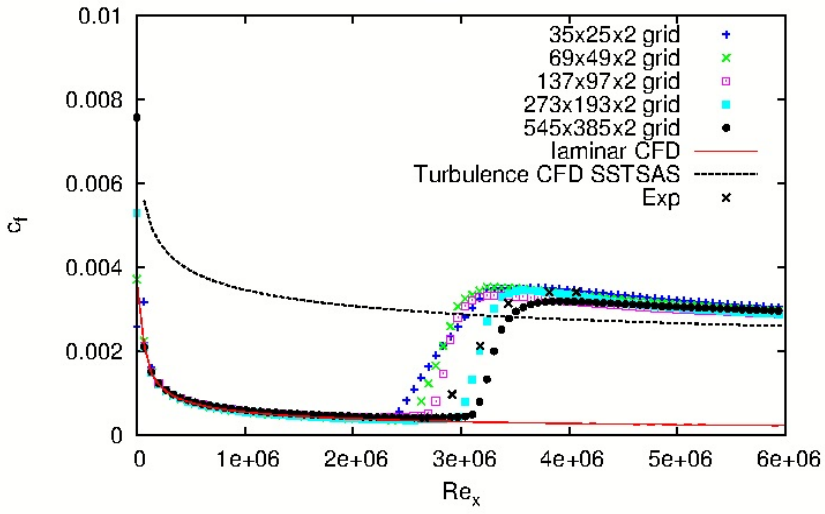

Figure 3.11 Mesh refinement study on the Schubauer-Klebanoff flat plate natural transition data

The results for the implemented SAS-Transition model with different mesh refinements are presented in Fig. 3.11. The uncertainty of the experimental data is not known. Generally, all the meshes predict the transition region, even the coarse mesh with few cells in the flow direction. Prediction of the transition onset location is moving downstream (from lower to higher local Reynolds number) as the grid is refined. However, this movement is damped between the two finest grids, one can observe an overshoot of the transition onset location for the finest mesh. Overall, results show that there is a mesh dependency in the calculation of transition onset location over the flat plate, in which the transition onset location shifts to higher Reynolds number with respect to the mesh refinement. The reason for this dependency is not identified as the meshes used from the NASA database lack specific information for mesh characteristics such as the expansion ratios normal to the wall and in the flow direction in order to be produce finer meshes. Kujansuu (2017) verified a one-equation intermittency correlation based transition model combined to the SST turbulence model using the same geometry and mesh from the NASA turbulence modeling resource. Similar to the current results, his mesh convergence study showed there is a mesh dependency, when meshes are refined for capturing the transition onset location over the S-K flat plate. A large overshoot for the coarsest mesh was identified in his convergence study, while in the current investigation it presents an undershoot for the same coarse mesh. Due to the mesh resolution, the slope of the predicted transition region is more in-line with the experimental data, compared to the results computed in the scheme analysis section.

Overall, this verification study shows that using a TVD scheme for turbulence parameters of the SAS-Transition model can lead to less oscillation during the convergence. In addition, the mesh convergence study shows that the mesh resolution can be a source of error in capturing the transition onset location and its region, which should be further investigated with finer meshes.

3.4 Validation

The implemented transitional model is examined with four different experimental transitional flows over flat plates including, T3A, T3A-, T3B and Schubauer-Klebanoff (S-K). The T3 experimental series were performed by Rolls Royce and are known as the ERCOFTAC flat plate validation data. Due to rapid change of freestream turbulence along the flat plate, the T3 test cases are difficult to model (Langtry, 2006). The Schubauer-Klebanoff flat plate experiment was performed in the 1950's and is a benchmark for validation of natural transition flows with low turbulence intensity. In contrast, the T3 experiment series include high level of turbulence intensity, in which the bypass transitional flow is dominant. In the bypass transitional flows, the initial natural transition stage is bypassed at early stages of the transition that is usually due to the high turbulence intensity or roughness of the wall boundary. Four validation cases of flow over flat plates are detailed in Table 3.3.

Table 3.3 Details of flat plate validation case (Langtry, 2006)

Case	**Transition regime**	**Inlet velocity (m/s)**	$\boldsymbol{Tu}$ **(%)**	**Viscosity ratio**
S-K	Natural	50.1	0.03	1
T3A	Bypass	5.18	3.3	12
T3A-	Bypass	19.8	0.9	8
T3B	Bypass	9.4	6.2	90

3.4.1 Numerical domain

All the cases are tested on the same domain as presented in Fig. 3.1. The meshes on the domain are defined to satisfy the requirement for the y^+ less than 1 for all the cases.

3.4.2 Validation results

Distribution of skin friction along the flat plate for all the validation cases is presented in Fig. 3.12. The numerical results using the implemented transitional model are compared to experimental data and numerical data of Langtry (2006) using the SST-Transition model in each case.

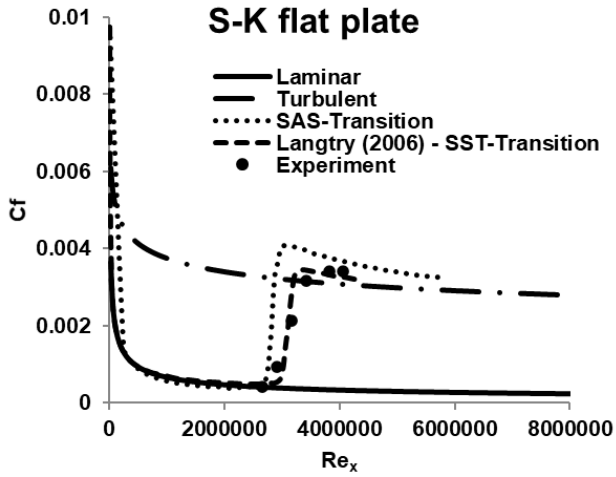

I. Schubauer-Klebanoff

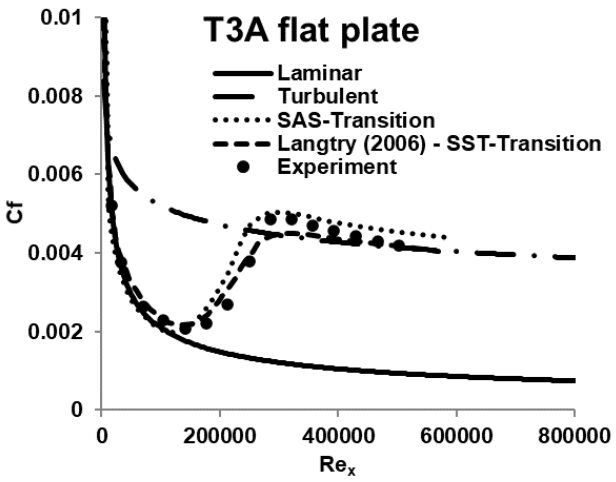

II. T3A

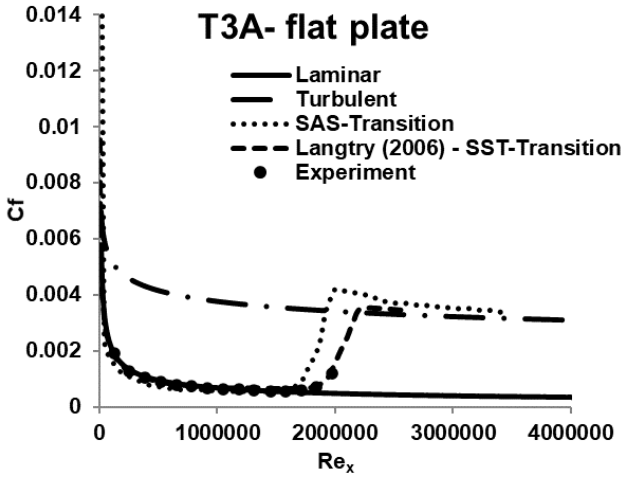

III. T3A-

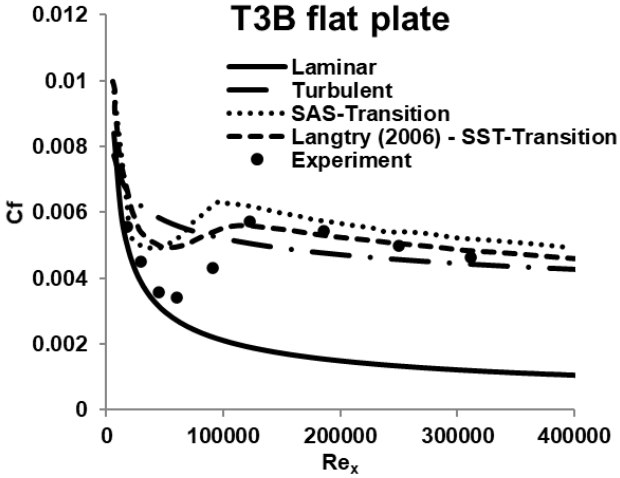

IV. T3B

Figure 3.12 Skin friction distribution along the zero-pressure gradient flat plate

The inlet boundary conditions are used to calculate the local friction coefficient with the following theoretical expressions (White & Corfield, 2006) for laminar and fully turbulent flows over flat plate, respectively.

$$C_f = \frac{0.664}{\sqrt{Re_x}} \tag{3.48}$$

$$C_f = \frac{0.027}{{Re_x}^{1/7}} \tag{3.49}$$

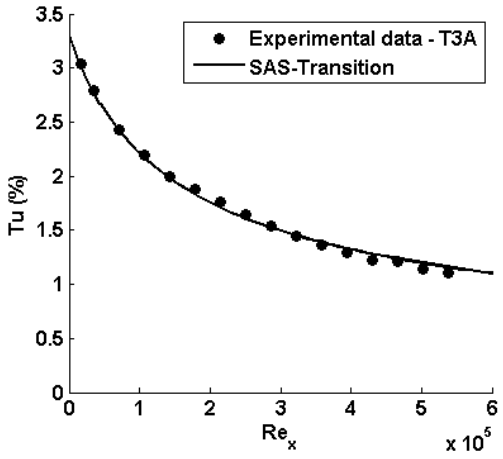

I. T3A

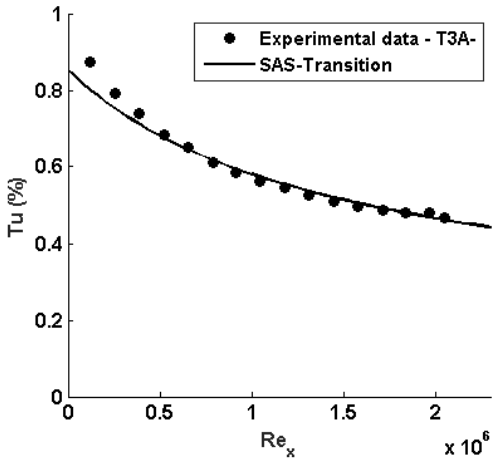

II. T3A-

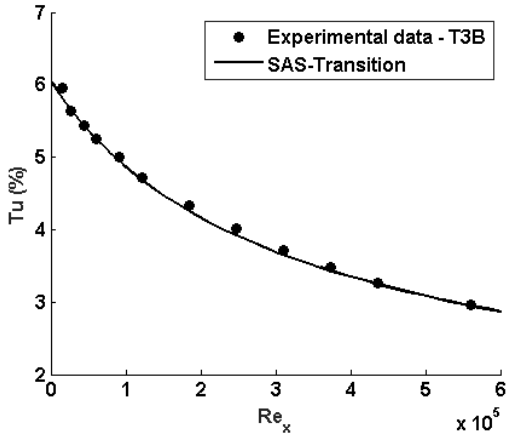

III. T3B

Figure 3.13 Turbulence intensity decay along the T3 flat plate series

The implemented model shows an adequate agreement compared to the theoretical calculations, however in the turbulent region, a slight over prediction of the friction coefficients is observed. Compared to the experimental data, results show that the implemented model can approximately predict the transition starting location for S-K, T3A and T3A- cases but there is a considerable difference in calculation of transition region for the T3B test case, which involves the highest

turbulence intensity of 6.2%. The same behavior was also predicted for the T3B case by Langtry (2006) using the SST turbulence model combined with the $\gamma - \widetilde{Re}_{\theta t}$ transition model. According to Langtry (2006), the over-prediction of friction coefficient for the T3B case is due to high values of eddy viscosity that has to be computed in order to capture the turbulence intensity decay rate along the flat plate.

The transition starting location moves upstream as the inlet turbulent intensity increases. The slope of the predicted transition region using the implemented model is higher than both experimental data and numerical results of Langtry (2006). The slope difference could be due to the mesh near the wall boundary; however, Langtry's numerical solutions shows a better agreement with the experiments. The domain dimension in his thesis was 1.5 m long and 0.22 m wide with 236×90 cells, while the domain used in the current investigation is 3.04 m long and 1 m wide with 240×80 cells.

Figure 3.13 shows a comparison of the results for the current implementation with experimental data on decay of turbulence intensity along the flat plate for the ERCOFTAC T3 series. There is not any available data for decay of turbulence intensity over the Schubauer-Klebanoff transitional test case. For the cases, an excellent agreement between the implemented transitional model and experimental data is observed.

3.5 Summery

The mathematical formulation of the $\gamma - \widetilde{Re}_{\theta t}$ transitional model was introduced. The transitional model was coupled with the SST-SAS turbulence model within the OpenFOAM simulation framework. The implemented model was tested for different flat plat test cases as steps of a verification and validation study. Results were compared to analytical solutions for the laminar and turbulent flow regions. The predicted slope of the transition region is higher than the one observed in the experimental data, which could be due to the mesh discretization.

CHAPTER 4 TRANSITION FLOW OVER A TRUNCATED HYDROFOIL

This chapter evaluates the effect of the Local Correlation-based Transition Model combined with the SAS turbulence model on the calculation of the shedding frequency in a high Reynolds flow using the OpenFOAM CFD software. First, the geometry of the experimental model and numerical domain will be described. The implemented transition model will then be applied to the truncated NACA0009 hydrofoil, and numerical results will be compared to both experimental data and numerical results of the SST turbulence model coupled with the same transition model. A mesh convergence study is also performed to compare the results between the implemented SAS-Transition and the SST- Transition.

4.1 Geometry

The NACA0009 hydrofoil is considered based on Ausoni's (2009) experimental study. The complete geometry specification of the hydrofoil is NACA0009- 7.8 45/1.93, where the first extension defines the leading-edge radius, the second describes the chord wise location of the maximum thickness (45%), and the last extension is the slope at the trailing edge (1.93). The original chord length is $110\ mm$, which is truncated at $L = 100\ mm$ and the resulting trailing edge thickness *h* is 3.22 mm. The angle of attack is set to $\alpha = 0^o$. The foil thickness distribution is given by Eqs. (4.1) and (4.2), where x and y represent stream-wise and transverse coordinates.

$$\begin{cases} 0 \le \frac{y}{L_0} \le 0.5 & \frac{y}{L_0} = a_0\left(\frac{x}{L_0}\right)^{1/2} + a_1\left(\frac{x}{L_0}\right) + a_2\left(\frac{x}{L_0}\right)^2 + a_3\left(\frac{x}{L_0}\right)^3 \\ 0.5 \le \frac{y}{L_0} \le 1 & \frac{y}{L_0} = b_0 + b_1\left(1 - \frac{x}{L_0}\right) + b_2\left(1 - \frac{x}{L_0}\right)^2 + b_3\left(1 - \frac{x}{L_0}\right)^3 \end{cases} \tag{4.1}$$

where L_0 denotes the original chord length and:

$$\begin{cases} a_0 = +0.1737 \\ a_1 = -0.2422 \\ a_2 = +0.3046 \\ a_3 = -0.2657 \end{cases}, \quad \begin{cases} b_0 = +0.0004 \\ b_1 = +0.1737 \\ b_2 = -0.1898 \\ b_3 = +0.0387 \end{cases} \tag{4.2}$$

The hydrofoil geometry is presented in Fig. 4.1.

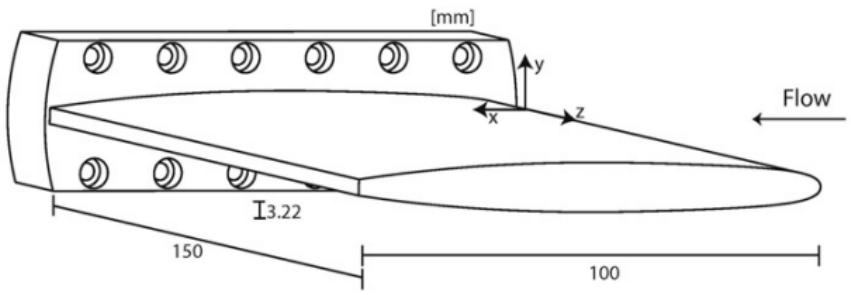

Figure 4.1 Truncated NACA0009 hydrofoil (Zobeiri, Ausoni, Avellan, & Farhat, 2012)

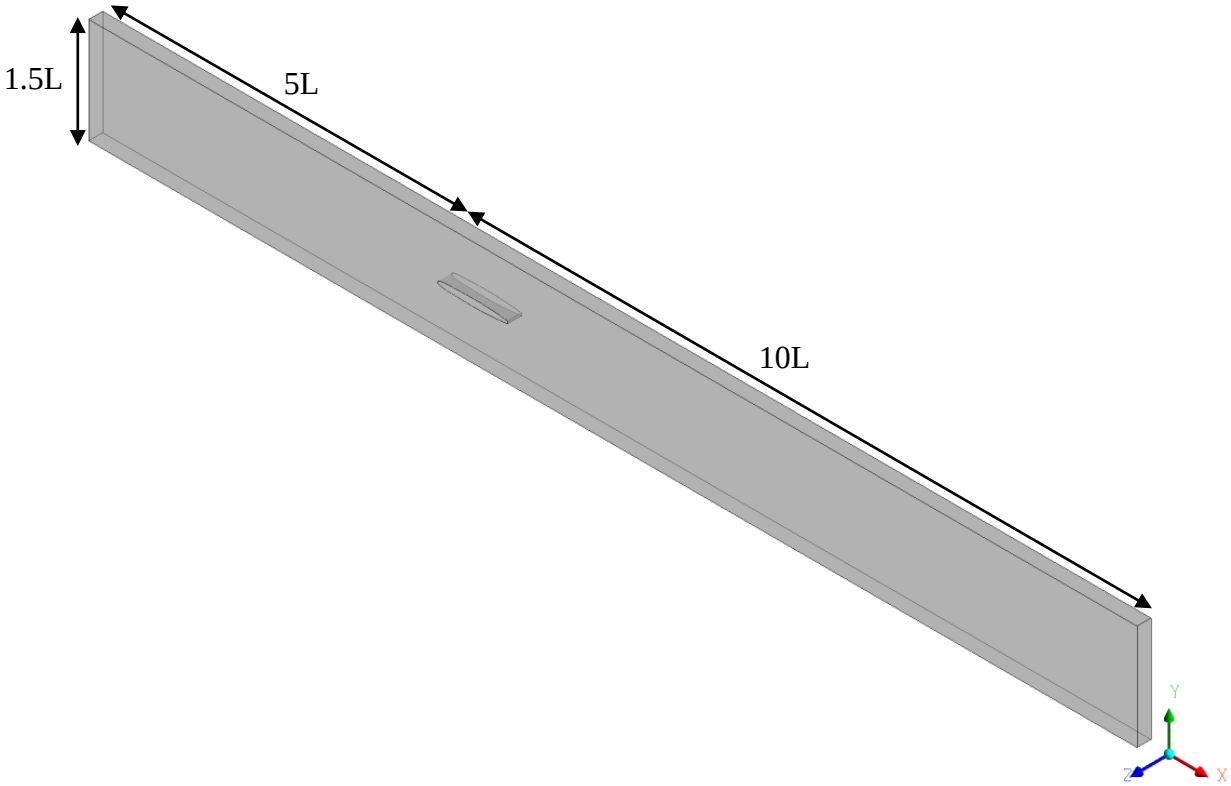

Figure 4.2 Domain of the CFD model

This geometry is selected because several studies are available in the literature that have numerically and experimentally investigated the fluid flow over this type of hydrofoil (Aït Bouziad, 2005; Ausoni, 2009; J. Chen et al., 2018; Di Domenico, Groth, Wade, Berg, & Biancolini, 2018; Fontanals et al., 2014; Lee, Lee, & Suh, 2015a; Lee et al., 2015b; Vu et al., 2007; Yao, Wang, Dreyer, & Farhat, 2014; Zobeiri, 2012; Zobeiri et al., 2012). The experimental investigations of Ausoni (2009) and Zobeiri (2012) on the NACA0009 hydrofoil will be the main references for the current study.

4.2 Numerical domain

The 3D experimental geometry is modeled by a quasi 3D domain, with one-layer extrusion in the span wise direction, shown in Fig. 4.2. The CFD model is 1.5 m long and 0.15 m tall. The distance between the inlet of the domain and the leading edge is $5L$ and the distance between the leading edge and the outlet is set to $10L$. The foil chord is located in the middle of the domain in the y direction. The density and dynamic viscosity of water, which is the flowing fluid are $\rho = 997\ kg/m^3$ and $\mu = 8.9 \times 10^{-4}\ kg/(ms)$, respectively.

4.3 Boundary conditions

Inlet boundary conditions

The inlet boundary conditions are commonly defined either on the incoming fluid velocity profile or its mass flow rate. In this study, the boundary velocity profile will be used and its components are defined with a value into the computational domain as: $\vec{U} = U_x\vec{\imath} + U_y\vec{\jmath} + U_z\vec{k}$. A constant inlet velocity of 17 m/s is considered for the mesh convergence study, while a wide range of inlet velocities will be investigated in the next chapter.

The inlet turbulent quantities of kinetic energy (k) and specific dissipation rate (ω), are estimated using the relationship between those quantities and turbulent intensity Tu (defined as root-mean-square of the velocity fluctuations, u', to the mean flow velocity, u_{avg}). The turbulent intensity for flows around the NACA0009 hydrofoil is around 1%, according to Ausoni (2009). Expressions for the calculation of k and ω are given as:

$$k_{inlet} = \frac{3}{2}(Tu.U)^2 \tag{3.3}$$

$$\omega_{inlet} = \frac{k_{inlet}^{1/2}}{C_\mu^{1/4} l} \tag{3.4}$$

where C_μ is an empirical constant equals to 0.09 and l is the turbulence length scale. An initial value of turbulent length scale equal to 0.001 m is used for the steady state simulations (Aït Bouziad, 2005).

Pressure outlet boundary condition

The relative static pressure over the boundary is typically prescribed at the outlet boundary. In order to prevent the disturbance of the flow in the outlet region, the outlet static pressure is constrained by defining an average value. In addition, for incompressible fluid flow, the pressure value is always relative, P/ρ, which is also known as kinematic pressure. Therefore, an averaged value of $P/\rho = 0$ Pa is prescribed for pressure at the outlet of the computational domain.

Symmetry boundary condition

The symmetry boundary condition defines constraints where the physical geometry of interest and the expected flow pattern of the solution present mirror symmetry. The perpendicular velocity component, U_n, and scalar variable gradient normal to symmetry plane boundary, $\frac{\partial \emptyset}{\partial n}$, are set to be equal to zero. Two XY and two XZ planes are considered as symmetry boundaries in the fluid domain, Fig. 4.2.

Wall boundary condition

The hydrofoil is kept as a smooth wall with no-slip condition (for the mass and momentum calculation). The pressure gradient at the wall boundary is set to zero. An experimental review by Fernholz and Finleyt (1996) presented that the assumption produces acceptable results throughout the boundary layer. To investigate the boundary layer mesh effect on the calculation of the shedding frequency, wall functions will not be used in the wall treatment.

4.4 Numerical scheme

Simulations will be performed using the open source CFD solver OpenFOAM-1706. The SAS-Transition and SST-Transition models are examined to perform mesh convergence study on the domain. A steady state solution is used as an initial condition for the URANS computations, with a target residual convergence criterion set to 10^{-5} for all primitive variables. The second order backward implicit scheme is used for time discretization of all transient computations. Boundary layer mesh specification are provided in Appendix A. The total simulation time is 0.45 seconds, which covers more than five time periods needed by the flow to cross the domain from inlet to outlet with inlet velocity of 17 m/s. The TVD *limitedlinear 1* scheme is used to discretize gradient terms of turbulence and transitional parameters.

4.5 Temporal analysis

Time step control is a significant aspect of transient CFD simulations to capture the time dependent features of the flow. Ideally, small time step would increase the chance of capturing smaller time dependent phenomena, while it increases the cost of the solution. Therefore, it is needed to analyze the time step effect to find a balance between the numerical accuracy and computational cost. Temporal analysis was done by comparing shedding frequency results using the SST and SST-SAS turbulence models.

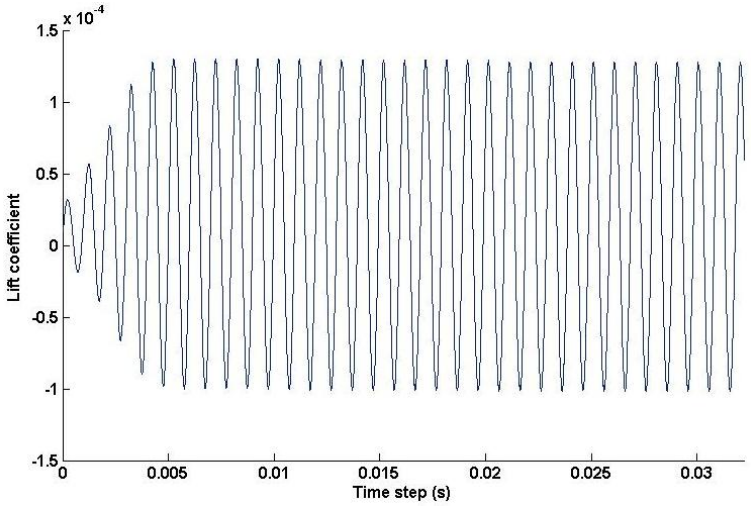

Figure 4.3 Fluctuation of the lift force coefficient

For transient simulations, lift coefficient on the hydrofoil is monitored for computation of shedding frequency, as illustrated in Fig. 4.3. Initialized by a steady state solution, the transient computational solution reaches the periodic behaviour in its early stages. After about 0.005 seconds from the beginning of the transient solution, the lift coefficient presents a fully developed periodic nature due to the vortex shedding phenomena.

In frequency analysis, the frequency spectrum is commonly evaluated as the distribution of signal magnitude with reference to frequency using FFT. The fluctuation variable is sampled N times with identical time steps t_s. The FFT calculation will yield an array of N/2 spectral values. The resulting frequency range will be from zero to $F = \frac{f_s}{2} = \frac{1}{2t_s}$, and the frequency interval or resolution is defined as $\Delta f = \frac{f_s}{N}$ (Dörfler et al., 2013). The more the samples, the higher the

frequency resolution, increase the accuracy of the calculated frequency. Series of sampling analysis are conducted during time step evolution using the SST and SST-SAS turbulence models, as shown in Figs. 4.4 and 4.5. In Fig 4.4 and time step 0.0001 *s*, there is up to 6% difference in the frequency calculation between the maximum calculated frequency and the one with the highest frequency resolution. Comparison between Figs. 4.4 and 4.5 show that SST-SAS model predicts higher shedding frequency than the SST turbulence model for the same time steps and resolutions.

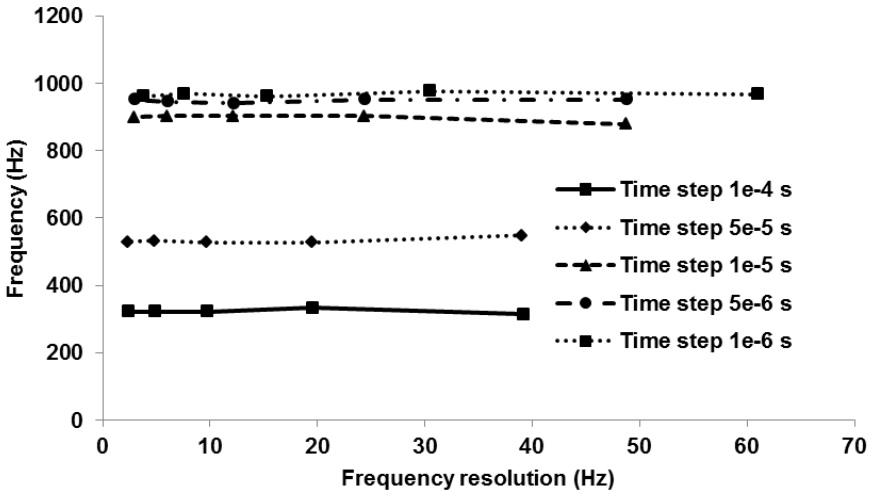

Figure 4.4 Sampling analysis using the SST turbulence model

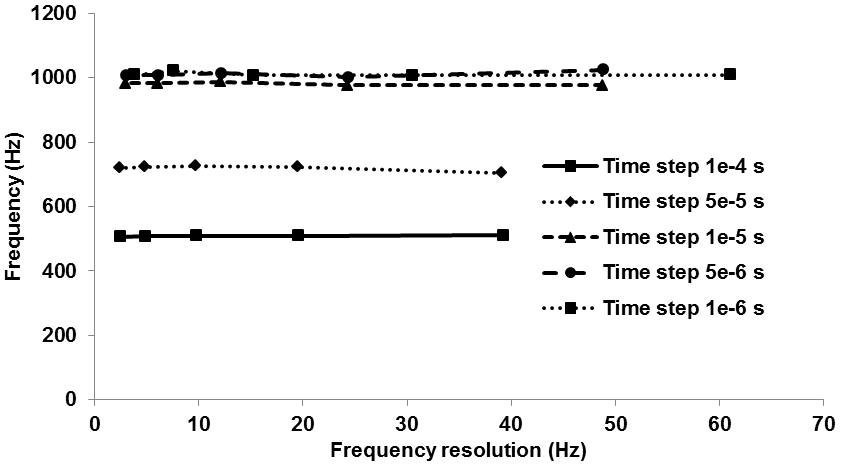

Figure 4.5 Sampling analysis using the SST-SAS turbulence model

A time step analysis is performed to evaluate its effects on the calculation of shedding frequency, as shown in Fig. 4.6. The oscillation frequency increases by decreasing the time step size, while the difference of the calculated frequency gradually reduces as the time step size gets smaller.

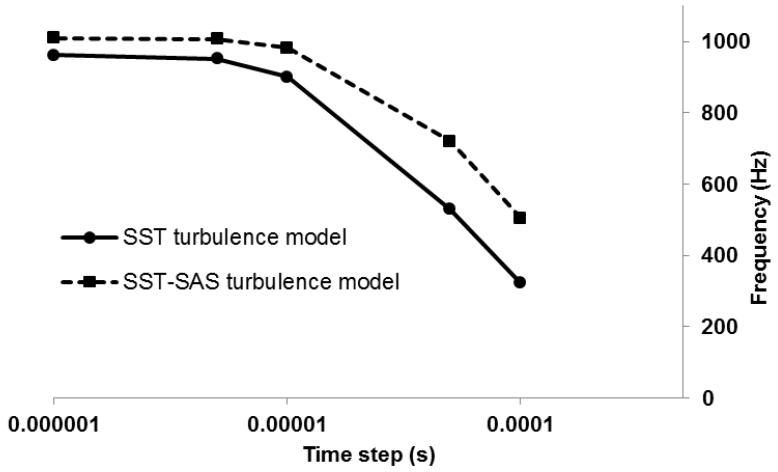

Figure 4.6 Time step effect on the lift coefficient frequency

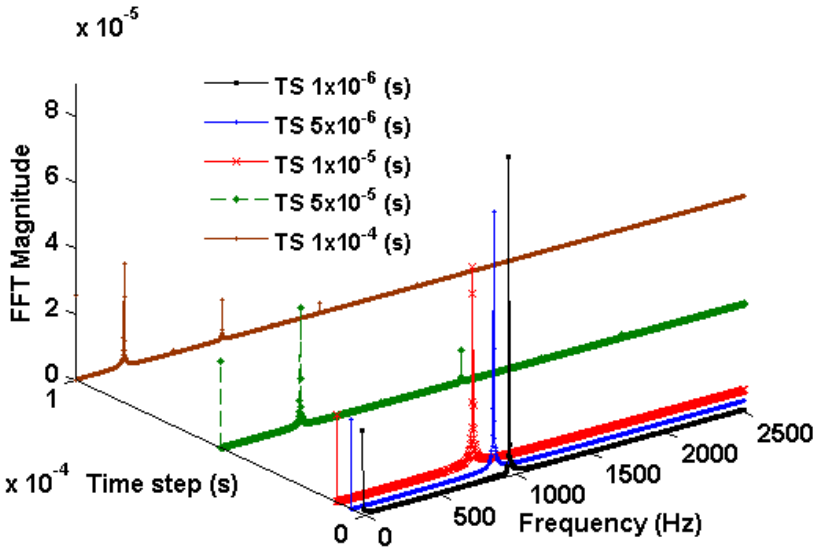

Figure 4.7 FFT at different time steps with the SST turbulence model

Figures 4.7 and 4.8 show FFT calculation results at different time steps using the SST and SST-SAS turbulence models. Even though there is less than 17% difference between the highest computed frequency and the experimental value (1214 Hz), the calculated values using SST-SAS turbulence model presents higher values than those estimated using the SST turbulence model.

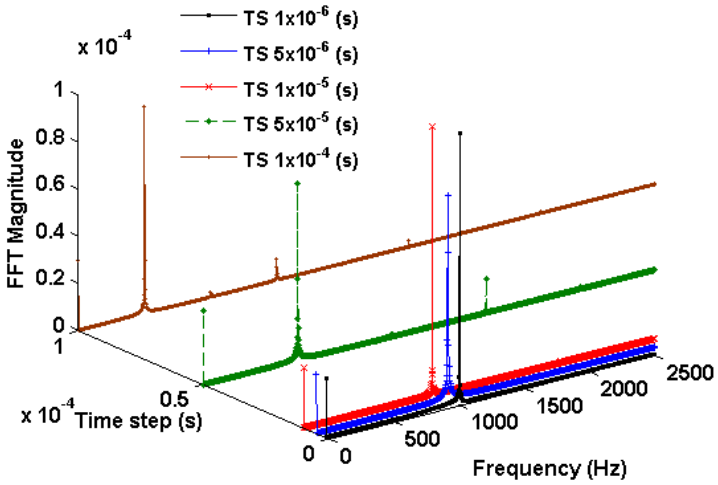

Figure 4.8 FFT at different time steps with the SST-SAS turbulence model

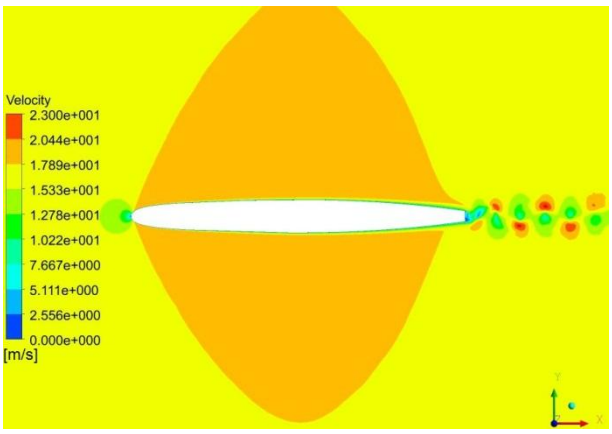

a) Instantanous velocity distribution
SST-SAS model

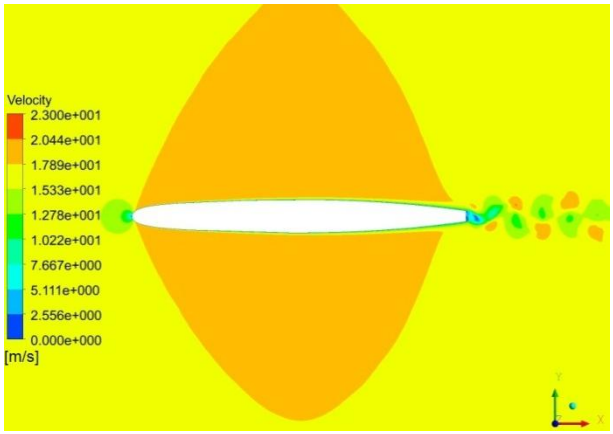

b) Instantanous velocity distribution
SST model

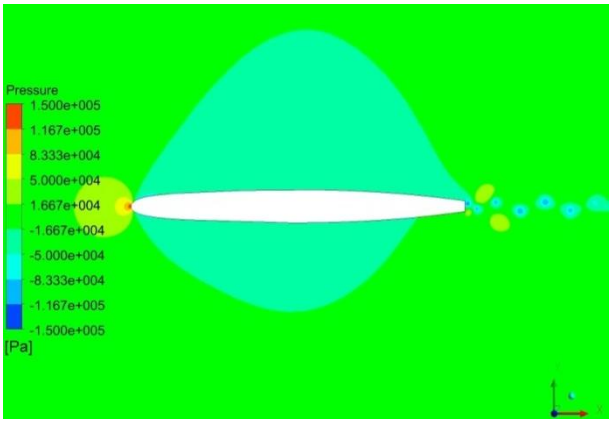

aa) Instantanous pressure distribution
SST-SAS model

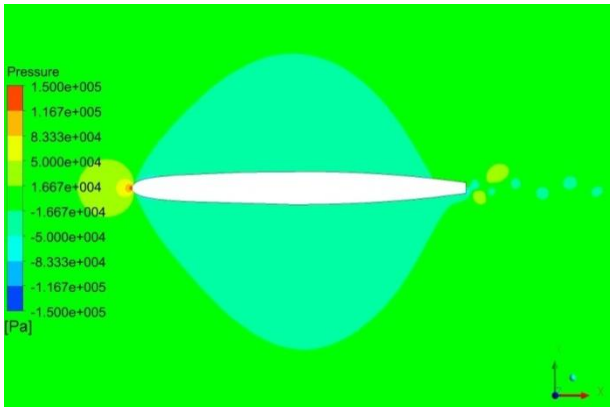

bb) Instantanous pressure distribution
SST model

Figure 4.9 Velocity and pressure distributions with the time step of 5e-6 s

As a sample, velocity and pressure distributions for the SST and SST-SAS turbulence models with the time step 5e-6 *s* are presented in Fig. 4.9. As indicated, the SST-SAS model predicts vortex cores at the trailing edge with higher velocities and much lower pressures than that predicted by the SST turbulence model. Accordingly, a time step of 5e-6 *s* can be selected for unsteady computations, which presents less than 1% difference in the frequency calculation when compared to the solutions with a time step of 1e-6 *s*.

4.6 Grid generation

A mesh that comprises adequate geometric quality and helps to control the discretization error is one of the significant components of the CFD modeling. Several commercial and inhouse meshing tools have been developed in recent years that can produce various types of meshes (e.g.: structured, unstructured and hybrid mesh). Vane-mesh is an automatic mesh generation software based on a mesh adaptation package named OORT (Dompierre & Labbé, 2001) that was developed in the MAGNU Laboratory (Laboratoire de Maillage et Géométrie Numérique, École Polytechnique de Montréal). This module was originally designed for mesh generation on hydrofoils and runner blades. It can quickly produce hybrid grids using various parameters. It offers high flexibility to fine-tune the grid resolution precisely and makes it easy to create uniformly refined structured grids in the boundary layers as well as unstructured tetrahedral grids in the core region of a flow domain.

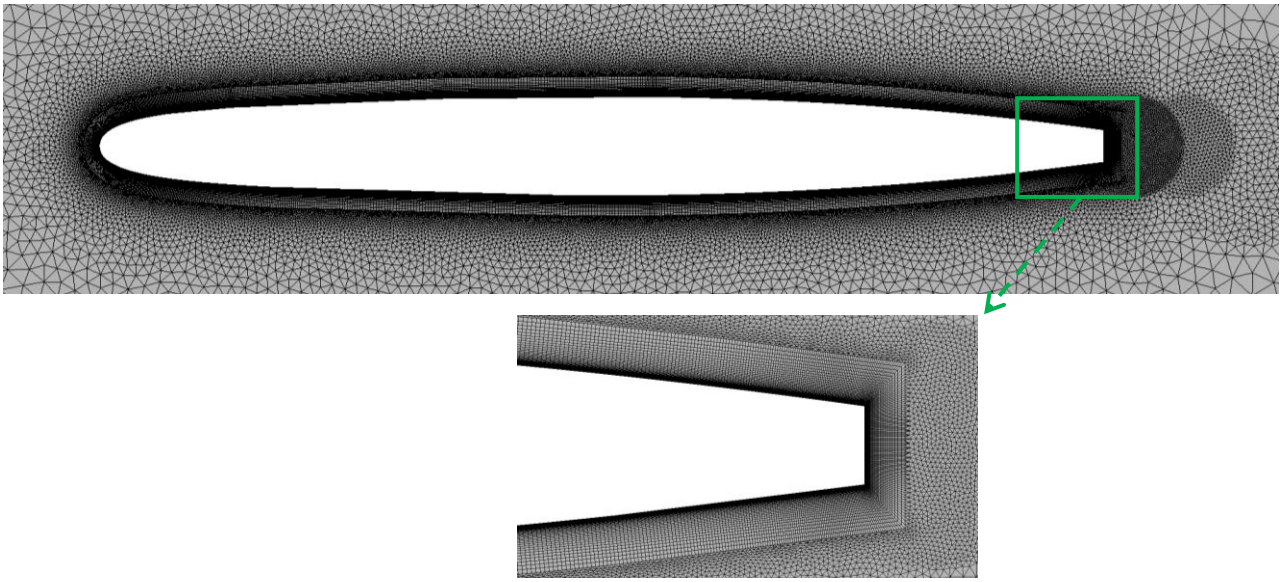

Figure 4.10 Hybrid mesh on the NACA0009 hydrofoil using the Vane-mesh tool

It is known that the bodies that shed span-wise vortices may be excited into oscillations by the fluctuation pressure forces resulting from the asymmetric formation of vortices (Sarpkaya, 2004; Williamson & Govardhan, 2004). Due to the shape of the truncated hydrofoil, a vortex street appears in the wake of the foil between the trailing edge and the outlet of the domain. Therefore, it is necessary to have fine meshes in this region to capture the phenomenon. In hybrid meshes, the size of the elements at the trailing edge can be managed by defining specific circular zones in the wake area using Vane-mesh. Related parameters for the circular zone in the wake are their locations, radius and their interior mesh size. It also provides several parameters (e.g.: first element size, growth ratio and boundary skin size) to control the boundary layer mesh characteristics. Figure 4.10 shows a representation of a hybrid mesh on the NACA0009 hydrofoil created by Vane-mesh.

4.7 Transition turbulence model on NACA0009 hydrofoil

The outcome of the turbulence model validation shows that the proposed approach adequately predicts flow properties over a flat plate. Given that, the implemented transition turbulence model is now considered to be applied to the NACA0009 hydrofoil. For mesh refinement, boundary layer mesh parameters were investigated, including the number of tangential elements on the foil, the first cell height, and the skin thickness. Their effect on calculation of shedding frequency is evaluated. The evaluation process and selected values for each parameter are detailed in the Appendix A and the output is used for the current simulations. A mesh refinement analysis is also performed to investigate the mesh dependency of the CFD solutions. The boundary layer mesh parameters are kept constant during the mesh refinement and only elements in the core region were refined.

Table 4.1 Frequency calculation using transition model

Model	**Mesh nodes**	**Frequency (Hz)**	**Error (%)**
Experiment	--	1214	~1.8
SST-Transition	~186 k	1190	1.9
	~480 k	1190	1.9
	~920 k	1193	1.7
SAS-Transition	~186 k	1217	-0.2
	~480 k	1220	-0.5
	~920 k	1220	-0.5

Table 4.1 shows numerical results of the computed frequency using both SST and SAS turbulence models combined with the transition model. According to experimental data (Ausoni, 2009), the excitation frequency error for the inlet velocity of 17 m/s can vary up to 1.8%. The highest computed frequency using the SST-Transition model is close to the lower limit of the experimental data. However, results show that there is 1.7% difference between the computed frequency using SST-Transition model on the finest mesh (~920 k nodes) compared to the experiment. The computed excitation frequency using the SAS-Transition model is much closer to the experimental data. With the coarsest mesh, the difference between the computed frequency using the SAS-Transition model shows a difference of 0.2% with the experiment. Mesh refinement shows a low impact in computing higher frequencies on both turbulence models. Overall, the SAS-Transition model predicts a higher and more accurate frequency than the SST-Transition turbulence model.

This is while, Vu et al. (2007) used the SST turbulence model combined with the $\gamma - \widetilde{Re}_{\theta t}$ transitional model using the ANSYS-CFX commercial solver to capture the excitation frequency. Their results show that the excitation frequency for the inlet velocity of 17 m/s is equal to 1220 Hz. Their result is very close to the value computed using the SAS-Transition model in the current investigation. However, there is almost 2% difference between the computed values using the SST-Transition model in the current study and their numerical results.

Figure 4.11 presents the FFT figures for the NACA hydrofoil using the SST-Transition model along with different mesh resolutions. The computed lift coefficient for different meshes is also provided in Fig. 4.11. The lift coefficient figures show a fully periodic structure for different meshes. The mesh refinement has a minor effect on the frequency calculation.

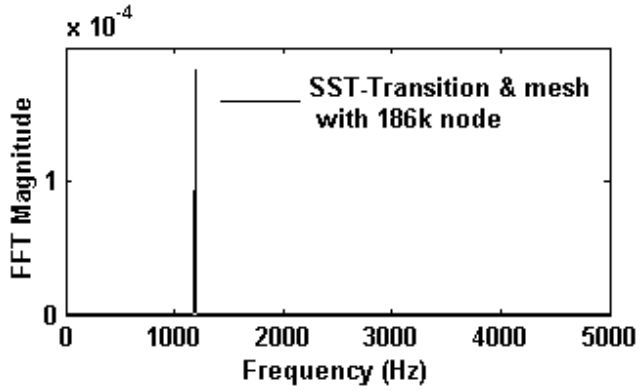

a) Frequency - mesh with 186 k nodes

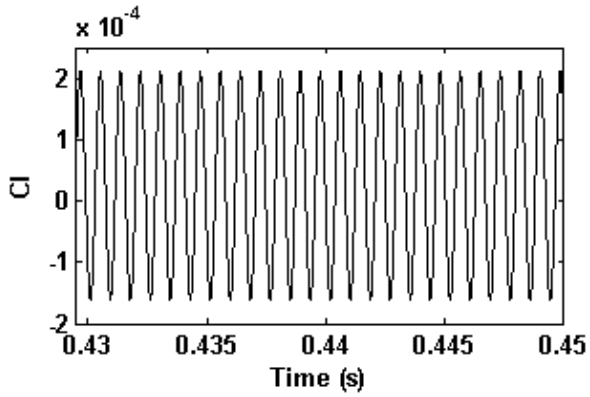

aa) Lift coefficient - mesh with 186 k nodes

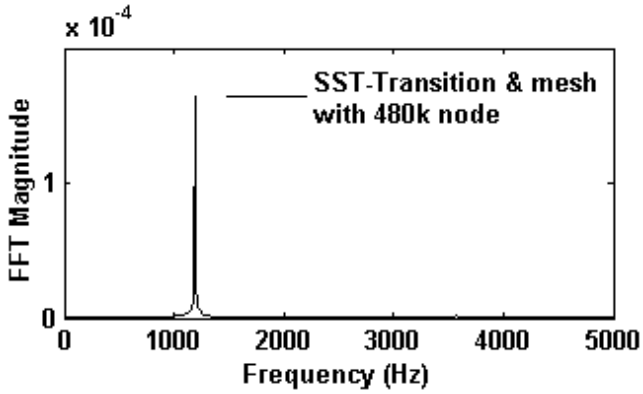

b) Frequency - mesh with 480 k nodes

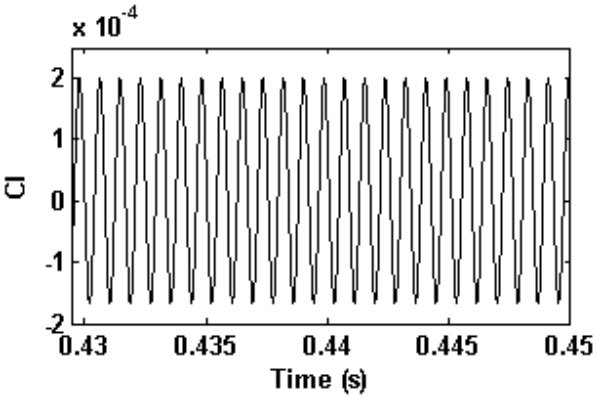

bb) Lift coefficient - mesh with 480 k nodes

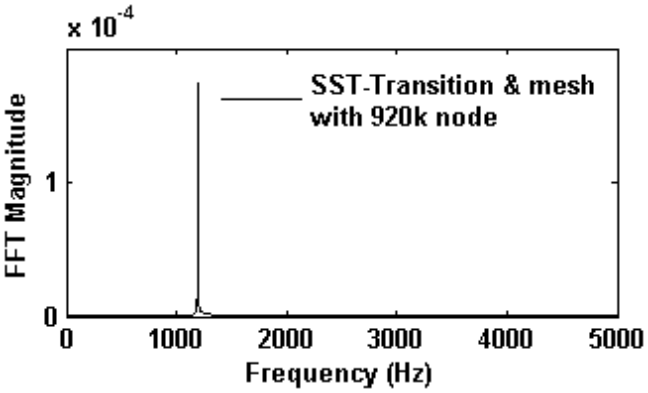

c) Frequency - mesh with 920 k nodes

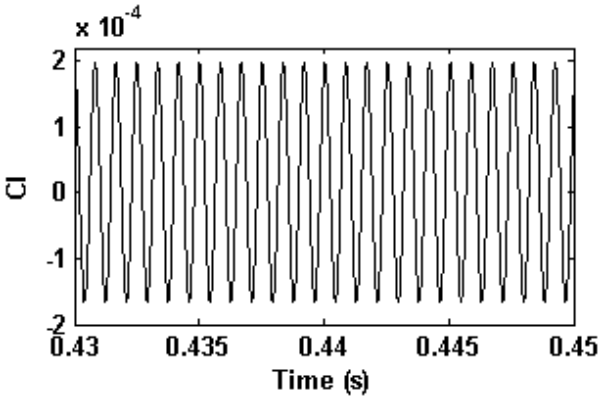

cc) Lift coefficient - mesh with 920 k nodes

Figure 4.11 Frequency and lift coefficient using the SST-Transition turbulence model

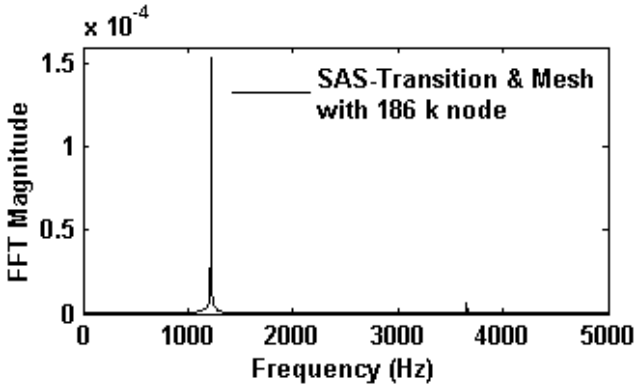

a) Frequency - mesh with 186 k nodes

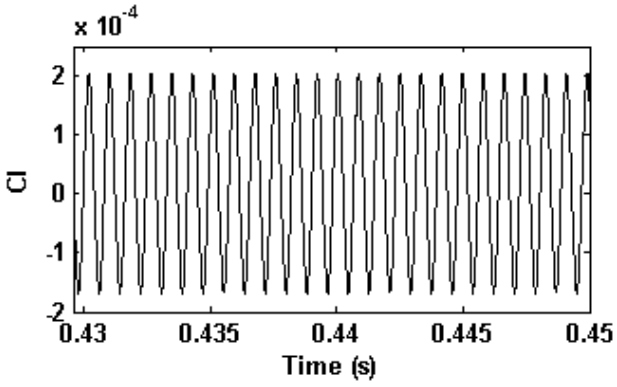

aa) Lift coefficient - mesh with 186 k nodes

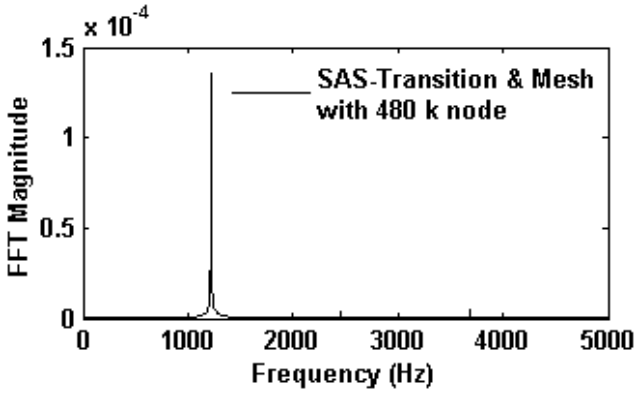

b) Frequency - mesh with 480 k nodes

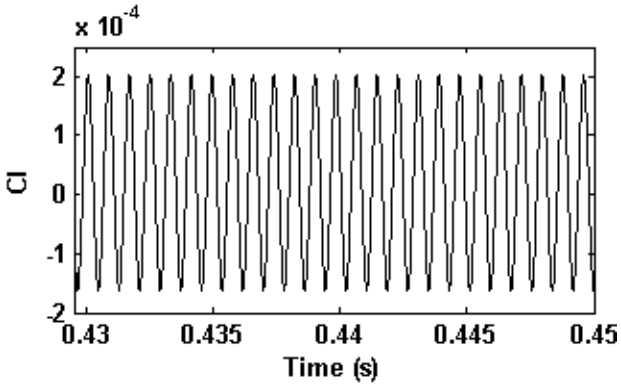

bb) Lift coefficient - mesh with 480 k nodes

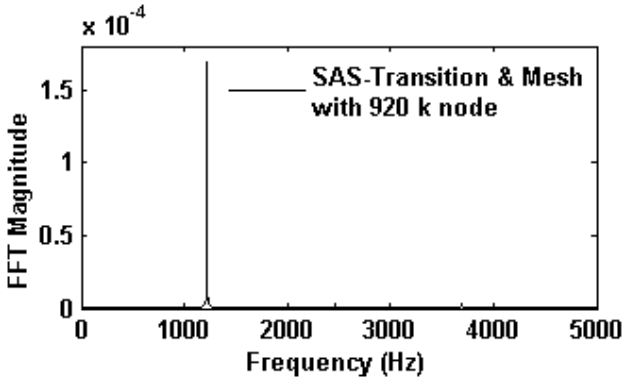

c) Frequency - mesh with 920 k nodes

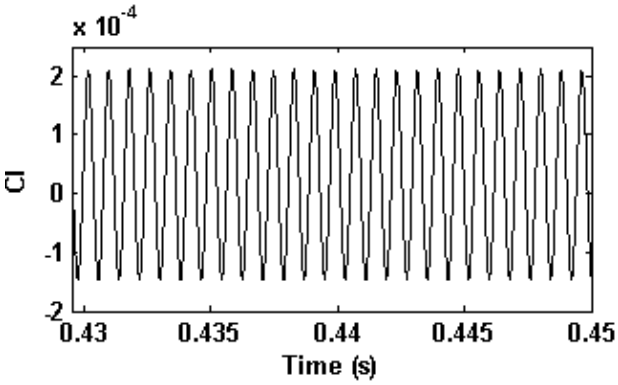

cc) Lift coefficient - mesh with 920 k nodes

Figure 4.12 Frequency and lift coefficient using the SAS-Transition turbulence model

Only 0.2% difference in frequency calculation can be observed by increasing the number of computational nodes from a mesh with 186 k nodes to almost 920 k nodes. However, this level of mesh refinement costs considerably in terms of computational time. Figure 4.12 presents computed frequencies over a NACA0009 hydrofoil using the SAS-Transition turbulence model

along with the lift coefficient for different mesh resolutions. Lift coefficient figures present a fully periodic behaviour for all mesh resolutions. According to the results, the computed frequency shows negligible dependency on the mesh resolution of the domain.

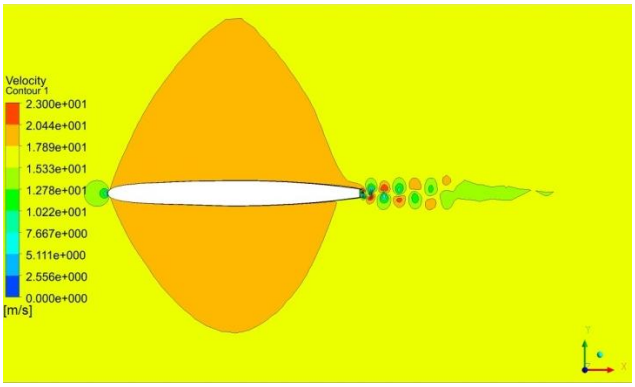

(a) 186 k nodes - SST-Transition

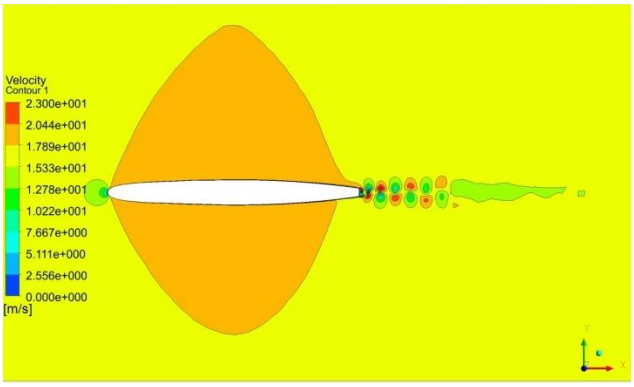

(d) 186 k nodes - SAS-Transition

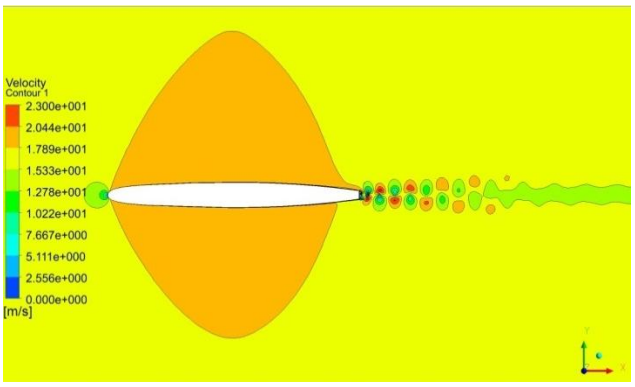

(b) 480 k nodes - SST-Transition

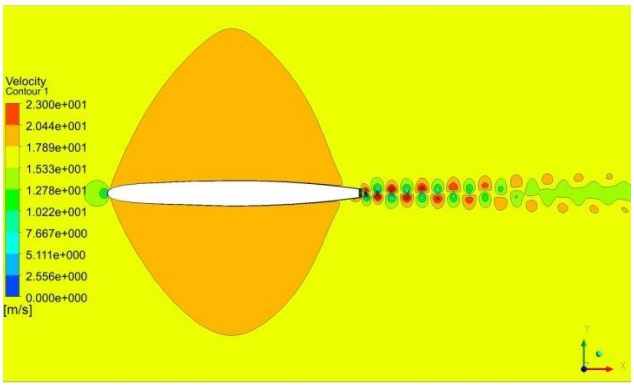

(e) 480 k nodes - SAS-Transition

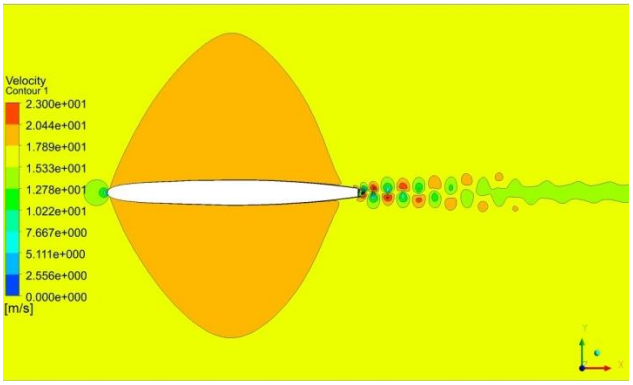

(c) 920 k nodes - SST-Transition

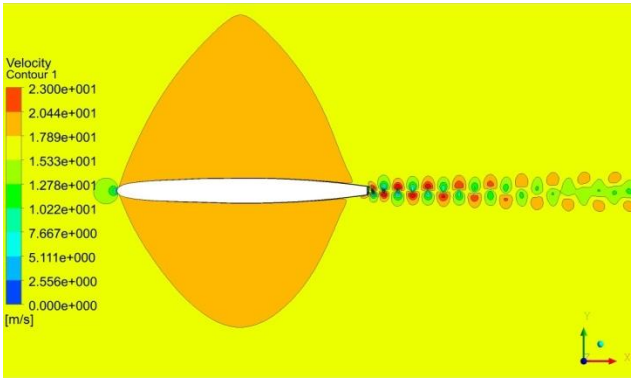

(f) 920 k nodes - SAS-Transition

Figure 4.13 Instantaneous velocity distribution for SST-Transition and SAS-Transition models

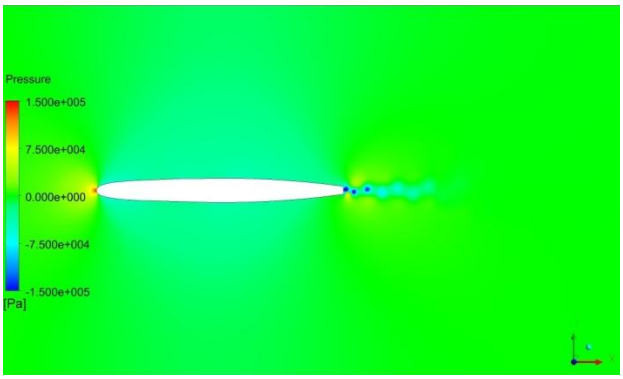

(a) 186 k nodes - SST-Transition

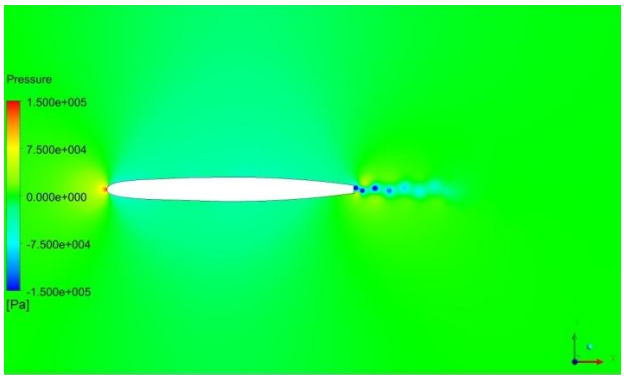

(d) 186 k nodes - SAS-Transition

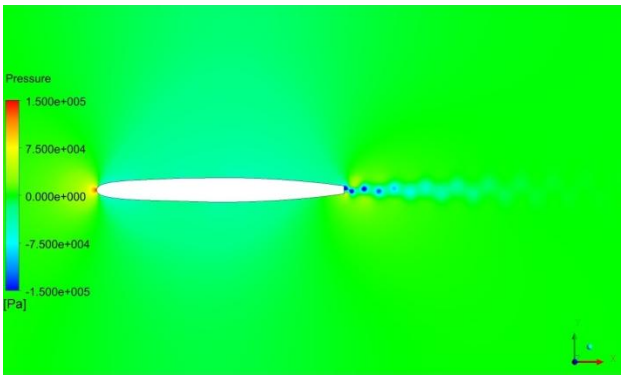

(b) 480 k nodes - SST-Transition

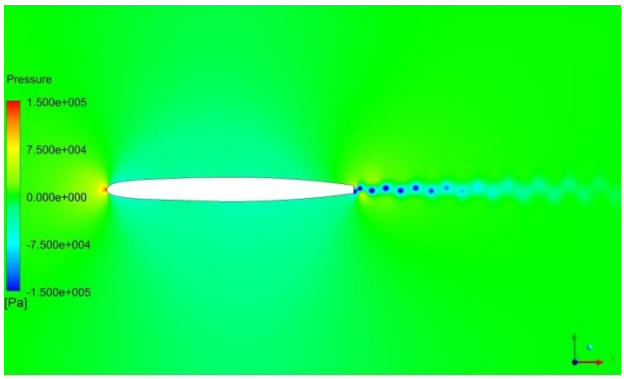

(e) 480 k nodes - SAS-Transition

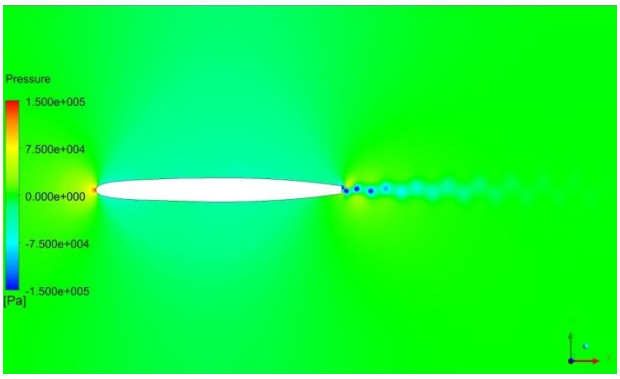

(c) 920 k nodes - SST-Transition

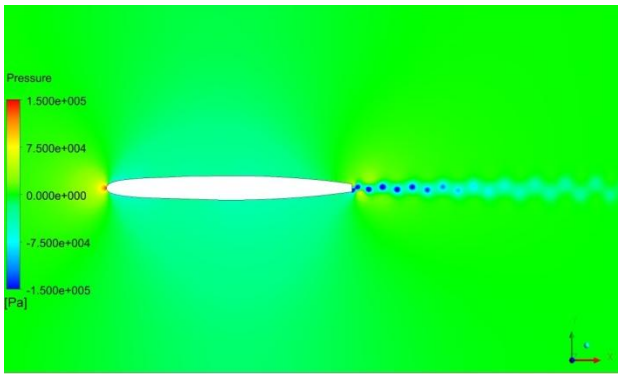

(f) 920 k nodes - SAS-Transition

Figure 4.14 Instantaneous pressure distribution for SST-Transition and SAS-Transition models

Figure 4.13 shows velocity contours for different meshes using both SST and SAS with the transition model. As indicated in the results, the SAS-Transition model predicts higher velocity distribution around the truncated hydrofoil than the SST-Transition model. As expected, the SAS-Transition model shows better capability to capture the relatively small flow structures in

the flow direction compare to the SST-Transition model. This is due to the additional source term in the SAS-Transition model, which helps the model to resolve small scale eddies.

Instantaneous pressure distribution using the SST-Transition and the SAS-Transition turbulence models along with different mesh resolutions are presented in Fig. 4.14. The pressure contours using the SST-Transition model indicate that vortices are rapidly damped at the trailing edge; while using the SAS-Transition model, the low-pressure regions, indicative of vortex streets, are slowly dissolved into the core stream.

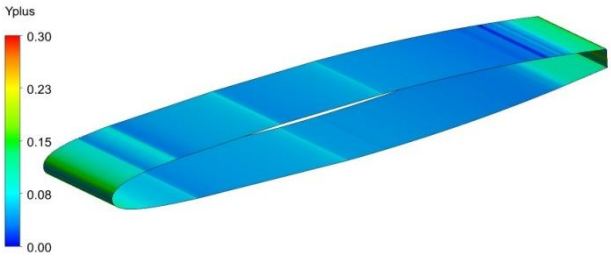

(a) 186 k nodes - SST-Transition

(d) 186 k nodes - SAS-Transition

(b) 480 k nodes - SST-Transition

(e) 480 k nodes - SAS-Transition

(c) 920 k nodes - SST-Transition

(f) 920 k nodes - SAS-Transition

Figure 4.15 y^+ distribution on the hydrofoil for SST-Transition and SAS-Transition models

Figure 4.15 presents the y^+ distribution on the NACA0009 hydrofoil with an inlet velocity of 17 m/s for the SST-Transition and the SAS-Transition model with different mesh resolutions. The

boundary layer mesh is consistent in all the meshes and almost similar behaviour of y^+ distribution can be observed on the different cases. The y^+ values on the hydrofoil for both turbulence models show approximately similar patterns. This is expected due to using a fixed boundary layer mesh in all the cases.

As the result shows, the SAS-Transition model predicts fluctuation frequency with an acceptable precision. However, it shows that the mesh dependency of the computed frequency is very low; a thorough validation of the flow properties over the NACA0009 is preferred. To do so, the mesh with 186 k nodes, which includes the minimum difference in terms of frequency calculation compared to the experimental results, is selected to study the transition onset location and shedding frequency of the implemented transition model for the flow over a NACA0009 hydrofoil with an inlet velocity of 20 m/s.

Table 4.2 Frequency analysis on the truncated hydrofoil with an inlet velocity of 20 m/s

Model	**Mesh nodes (kilo)**	**Frequency (Hz)**	**Error (%)**
Experiment	--	1440	~1.3
SAS-Transition	~186	1428	0.8

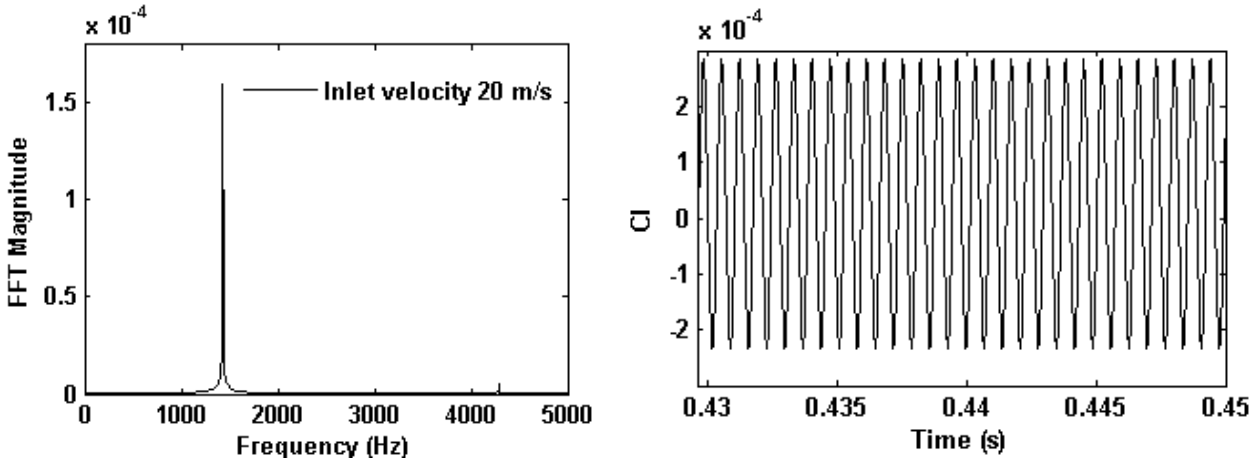

(a) **(b)**

Figure 4.16 (a) FFT analysis and (b) lift coefficient distribution for an inlet velocity of 20 m/s

Table 4.2 presents the computed frequency results using the SAS-Transition model with an inlet velocity of 20 m/s. The difference between the CFD solution and experimental data is less than

1%, which indicates that the model is in good agreement with the experiment. The lift coefficient distribution along the solution time and FFT analysis are shown in Figure 4.16.

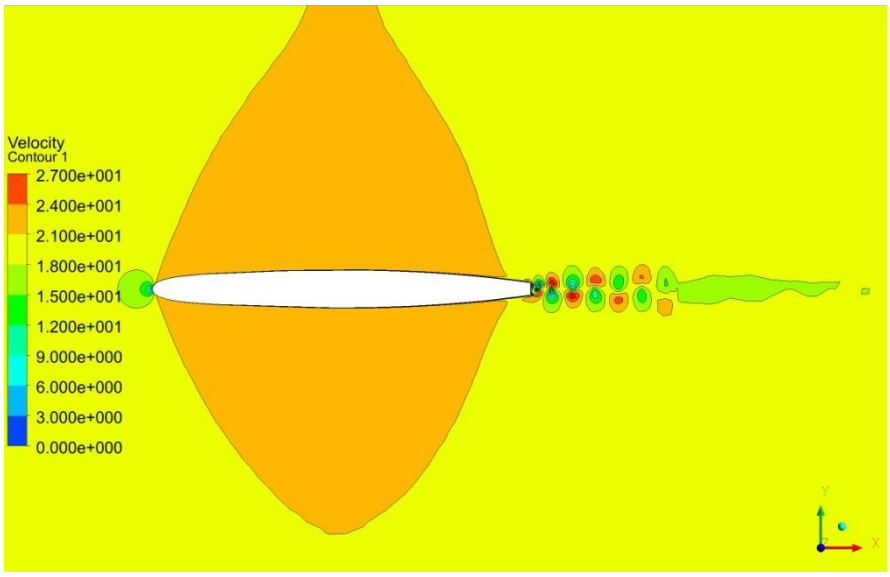

Figure 4.17 Instantaneous velocity distribution for the inlet velocity of 20 m/s

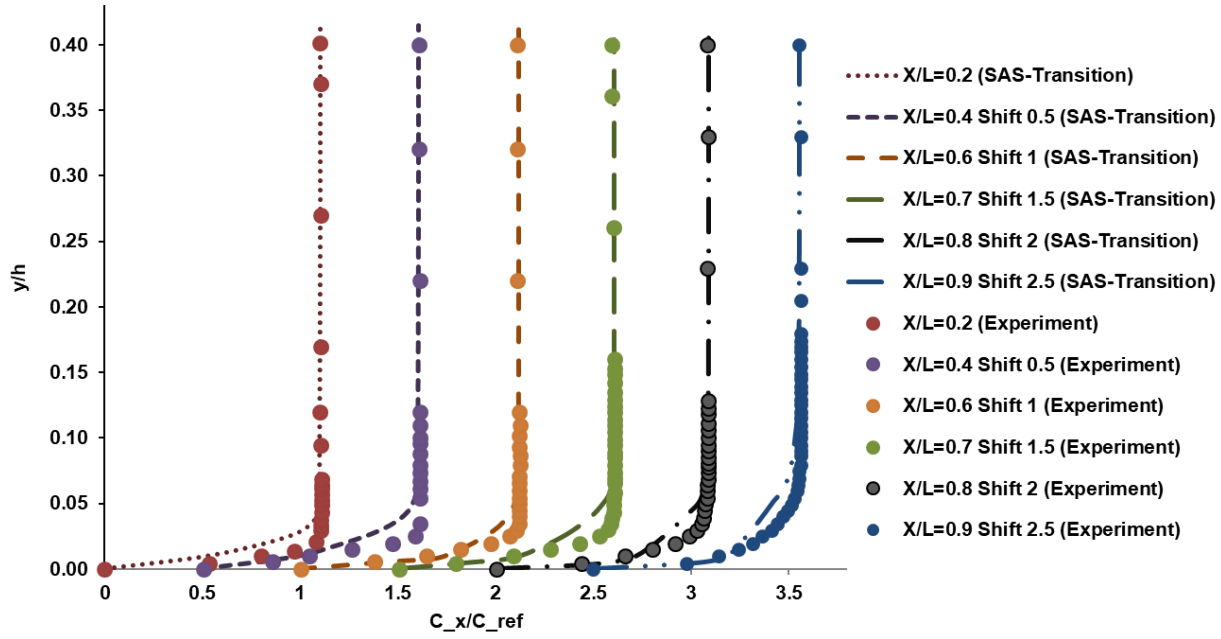

Figure 4.18 Comparison of instantaneous boundary layer velocity profile with the experimental data of time averaged velocity profile on the suction side for an inlet velocity of 20 m/s

Figure 4.17 shows the velocity magnitude distribution over the NACA0009 hydrofoil with the inlet velocity of 20 m/s at solution time t = 0.45 s. The instantaneous boundary layer velocity

profile using the SAS-Transition model at the solution time of 0.45 s is compared with the time-averaged boundary layer velocity profiles at 20, 40, 60, 70, 80 and 90% of the chord length of the available experimental data (Zobeiri, 2012) in Fig. 4.18. Results indicate that the CFD solution is closely capturing the flow properties when compared to the time averaged experimental data.

Pressure and y^+ distribution on the flow domain are presented in Figs. 4.19 and 4.20, respectively. The low-pressure points at the trailing edge indicate the vortex cores. The average y^+ on the hydrofoil wall is 0.09 and its maximum value is 0.32, which satisfies the requirement of the turbulence model of $y^+<1$.

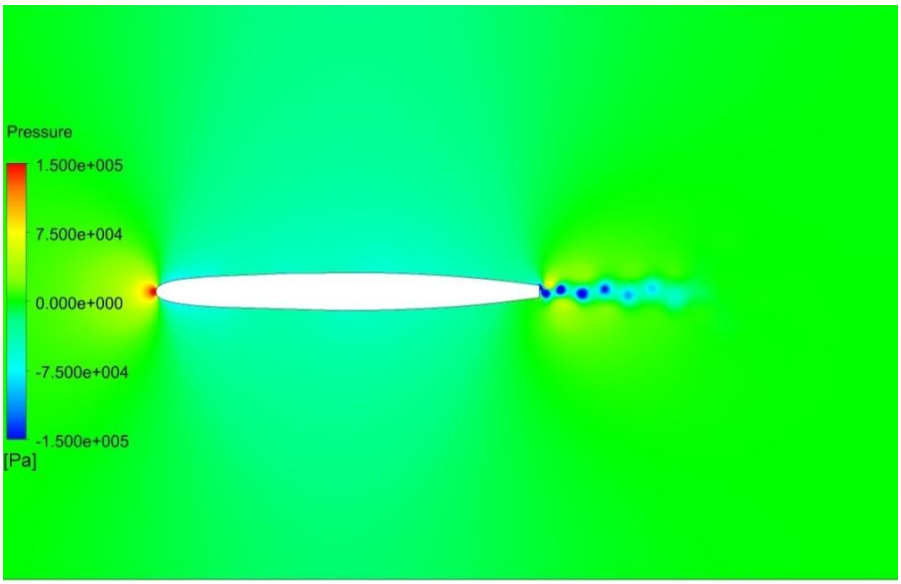

Figure 4.19 Instantaneous pressure distribution for an inlet velocity of 20 m/s

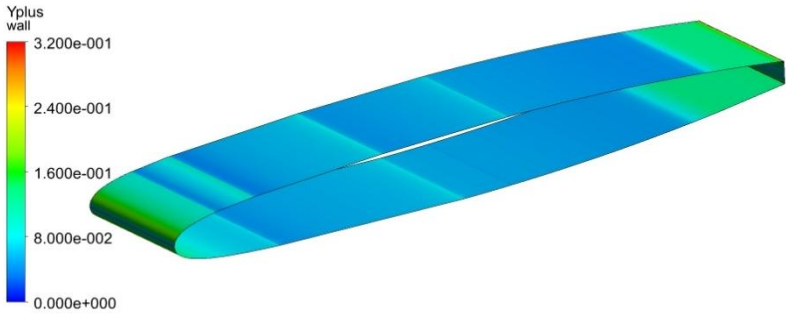

Figure 4.20 y^+ distribution on the truncated foil for an inlet velocity of 20 m/s

According to Zobeiri (2012), the transition process occurs in a region lying approximately between 80 to 90% of the chord length. The intermittency factor can be helpful to analyze the transition region. Based on its definition, locations where the intermittency is equal to zero are related to the laminar region and locations with intermittency equal to one identify fully turbulent regions. Figure 4.21 shows the intermittency contour along the hydrofoil. As indicated between the solid black lines, the captured transition region using the SAS-Transition model is located closely between 80 to 90% of the hydrofoil chord length, where the intermittency value in the boundary layer gradually rises from zero to one, Fig. 4. 21 (b).

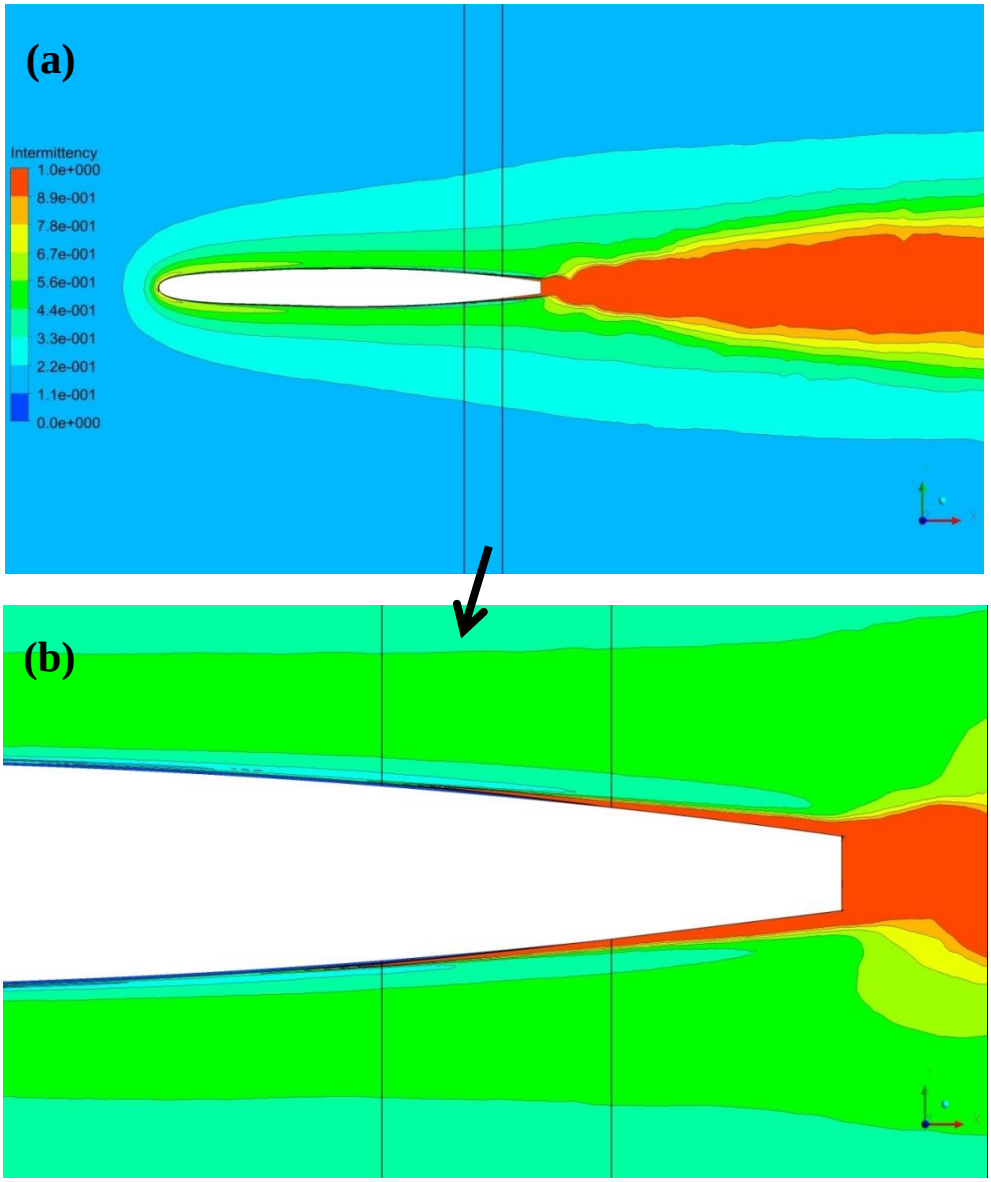

Figure 4.21 Intermittency distribution for an inlet velocity of 20 m/s

4.8 Summary

The $\gamma - \widetilde{Re}_{\theta t}$ transition model, which was originally adapted for the SST turbulence model is combined with the SST-SAS turbulence model. Flow around the NACA0009 hydrofoil was then evaluated using the SST-Transition and the SAS-Transition with various mesh refinements. Results indicate that the SAS-Transition model is in better agreement with experiment than the SST-Transition model in terms of shedding frequency prediction. Velocity profile around the NACA hydrofoil using the SAS-Transition model was also compared to the experimental data in order to validate the implemented SAS-Transition model in terms of flow properties. A good agreement between numerical solutions and experiment was observed in terms of velocity profile and transition onset location.

CHAPTER 5 RESULTS AND DISCUSSION

The successful adaptation of the $\gamma - \widetilde{Re}_{\theta t}$ transition model into the SST-SAS turbulence model and its validation justify investigating the implemented model in various geometric conditions. Due to the direct relation between vortex streets and boundary layer state along the hydrofoil, two types of trailing edge geometries are considered; first, the truncated TE and second, the Oblique TE. Both geometries will also be examined with a wide range of inlet velocities. Several researches have been devoted to the numerical analysis of transitional flow around the NACA0009 hydrofoil. Aït Bouziad (2005) investigated cavitation free transitional flows around the truncated NACA0009 hydrofoil using the SST turbulence model and the CFX commercial solver evaluating shedding frequencies at four different inlet velocities. His investigation showed a considerable difference between numerical solution and experimental data affected by inadequate turbulence modeling and wall treatment resolution. Vu et al. (2009; 2007) have studied flow around the 2D truncated hydrofoil using the CFX solver and SST turbulence model with $\gamma - \widetilde{Re}_{\theta t}$ transitional model. They have seen up to $\pm$15% difference between CFD simulation and experimental data in the lock-in region while, they have obtained accuracy within 1% of experimental results at lock-off condition.

Lee et al. (2015a) studied vortex shedding from the NACA0009 truncated hydrofoil using a 2D LES hybrid particle-mesh method and validated their numerical results at Reynolds 2×10^6. They found their proposed numerical method could reasonably calculate the shedding frequency and simulate the wakes of the hydrofoil. Lee et al. (2015b) have also numerically investigated vortex shedding from different beveled trailing edges at a Reynolds 10^6. To validate their numerical results, they have used experimental data from Zobeiri (2012), which showed a good agreement. Chen et al. (2018) have presented a LES numerical simulation of the truncated hydrofoil only for 20 m/s inlet velocity. They used a fine hexahedral mesh (approximately 5.0 million elements) to simulate transitional flow, which was designed to reach an average y^+ equal to 0.6 on the hydrofoil surface. The predicted transition process was validated by comparing the computed boundary layer velocity profiles with the experimental data of Ausoni (2009). However, they did not compare the shedding frequency with the experiment.

5.1 Truncated trailing edge

Excitation frequencies for a wide range of inlet velocities including lock-off and lock-in conditions over truncated NACA0009 hydrofoil were studied experimentally by Ausoni (2009). This thesis compares the CFD solutions of shedding frequencies using the SAS-Transition turbulence model with these experiments.

The mesh in the previous chapter, which presented acceptable results for the prediction of flow properties, oscillation frequency and transition onset location, is used to investigate the inlet velocity effect on shedding frequency computations.

The unsteady simulations are initialized with the steady state solution respective to their inlet velocities. All the cases were modeled with low turbulent intensity. Detailed FFT calculations for different inlet velocities are presented in Figs. 5.1 and 5.2. The calculated frequency using the SAS-Transition model for different inlet velocities are compared with experiments in Figure 5.3 and Table 5.1. The average uncertainty of the experimental data for shedding frequencies with different inlet velocities is less than 2%. There is an excellent agreement between the numerical results and experimental data except close to the inlet velocities that trigger the lock-in condition, where the resonance frequency is dominant. The maximum difference between experiment and the current simulations is observed at the inlet velocity of 10 m/s with approximately 10% error. This velocity is close to the lock-in region. Vu et al. (2007) recommended at least $\pm 20\%$ margin from the stay vane natural frequency to avoid resonance due to the vortex shedding. The lock-in frequency of the hydrofoil is close to 900 Hz. When one simulates flows with inlet velocities lower than lock-in region, this investigation shows that considering a -20% margin from the lock-in frequency is reasonable to avoid resonance effects. While for the upper limit considering a +10% margin from the lock-in frequency would be enough to avoid resonance using the SAS-Transition model. Results show that the minimum difference between the numerical results and the experiment happens close to the inlet velocity of 17 m/s. This could be due to the computational mesh that was originally designed for that inlet velocity and was used for the whole velocity range. This indicates that using one mesh can give fairly reasonable results for the whole velocity spectrum. However, if one requires to decrease the mesh discretization effect, it is recommended to customize the mesh for each specific inlet velocity.

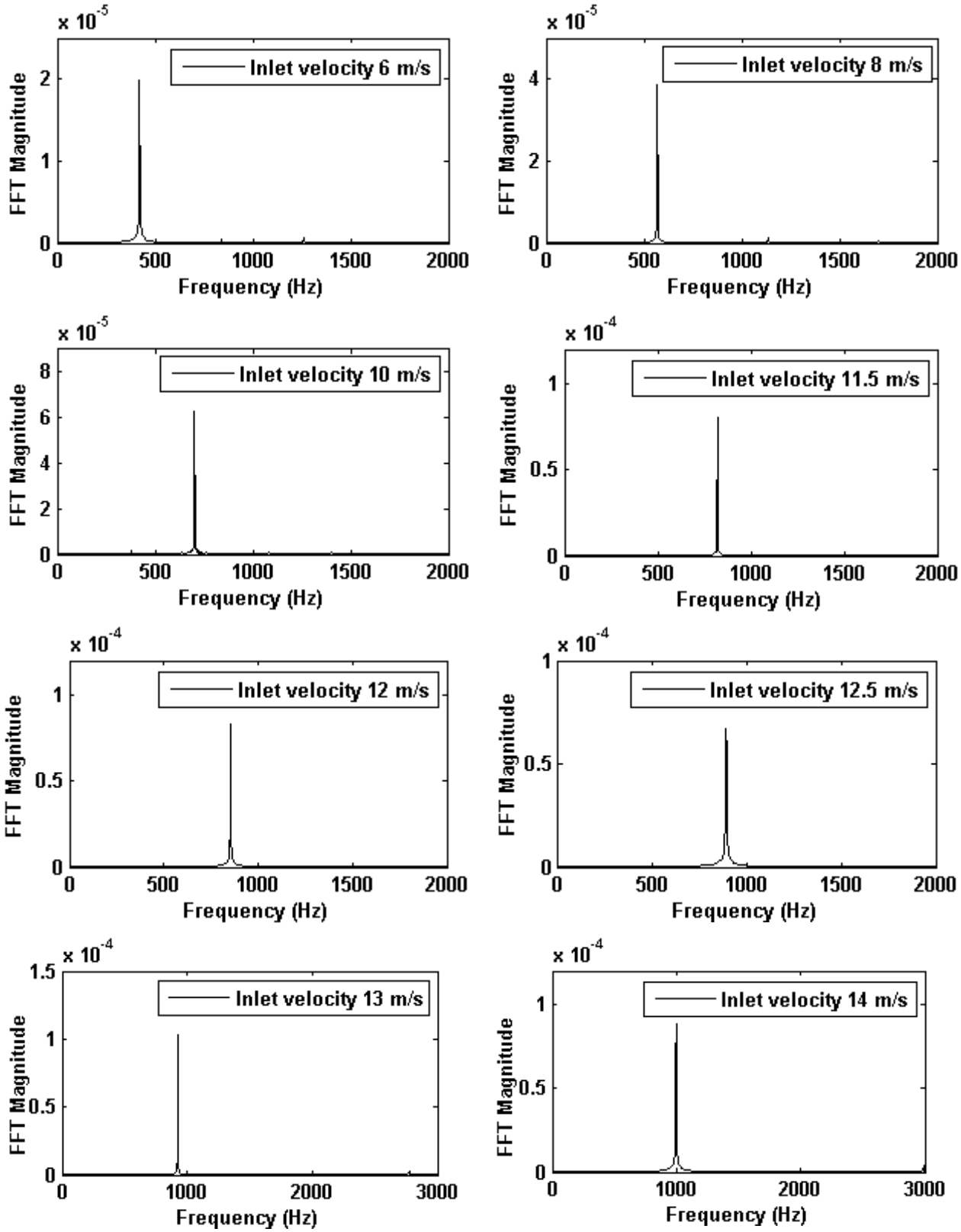

Figure 5.1 FFT calculation of inlet velocities from 8 to 14 m/s for the truncated TE

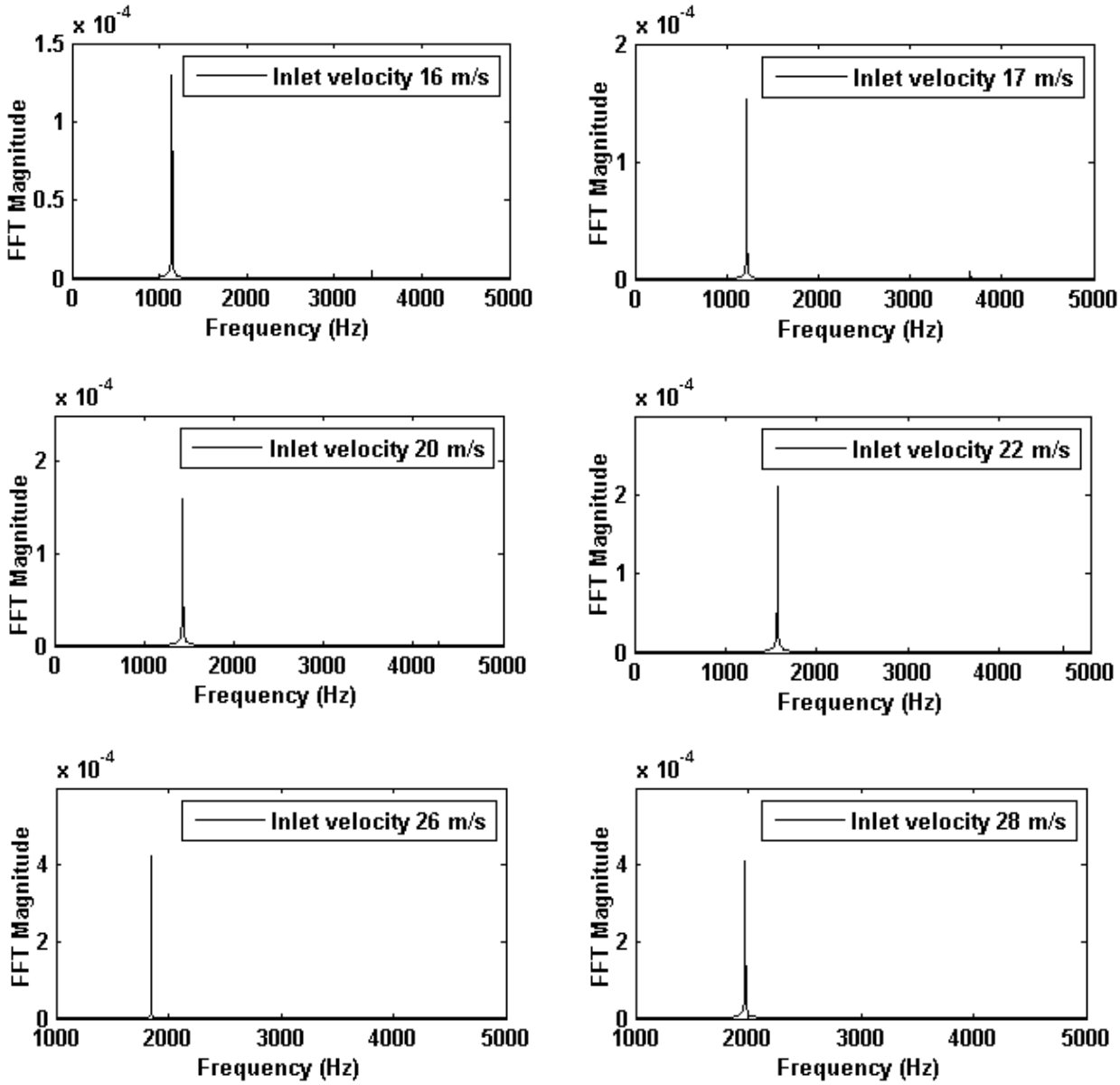

Figure 5.2 FFT calculation of inlet velocities from 16 to 28 m/s for the truncated TE

CFD solutions show a linear relationship between the fluctuation frequency and the inlet velocity. The linear relationship between excitation frequency and inlet velocity is defined in Eq. 5.1. The least square method is used for the correlation coefficient, which gives a $R^2 = 0.9997$. The coefficient measures the amount of linear association between the two variables. A very close coefficient comparing to the current analysis was found by Ausoni (2009), which was equal to 0.998.

$$F = 70.456U + 7.5366 \quad (5.1)$$

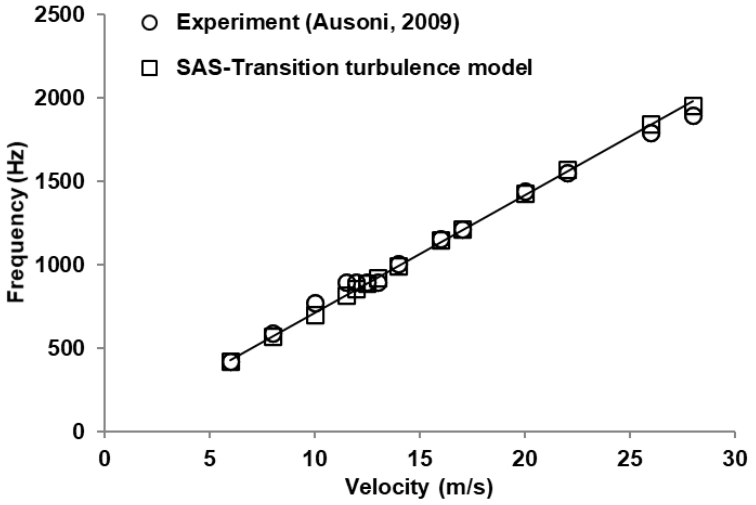

Figure 5.3 Shedding frequency versus inlet velocity for the truncated TE

Table 5.1 Shedding frequency versus inlet velocity for the truncated TE

Inlet Velocity (m/s)	Experimental Frequency (Hz)	SAS-Transition Frequency (Hz)	Error (%)
6	424	421	0.70
8	589	568	3.56
10	775	702	9.41
11.5	895	820	8.38
12	895	855	4.47
12.5	895	888	0.78
13	895	920	2.79
14	1003	994	0.89
16	1156	1147	0.77
17	1214	1217	0.24
20	1440	1428	0.83
22	1551	1568	1.09
26	1793	1843	2.78
28	1898	1953	2.89

Numerical solutions of the Strouhal number, fh_m/C_{ref}, versus chord wise Reynolds number at lock-off condition are compared to the experimental data of Zobeiri (2012) in Fig. 5.4, where h_m is the maximum thickness of the hydrofoil. As the inlet velocity increases, the Strouhal number shows a decreasing response, which is predicted by the experiments and current simulations. This

is due to the increase of the boundary layer thickness at the trailing edge of the truncated hydrofoil as the flow stream velocity increases, (Zobeiri, 2012).

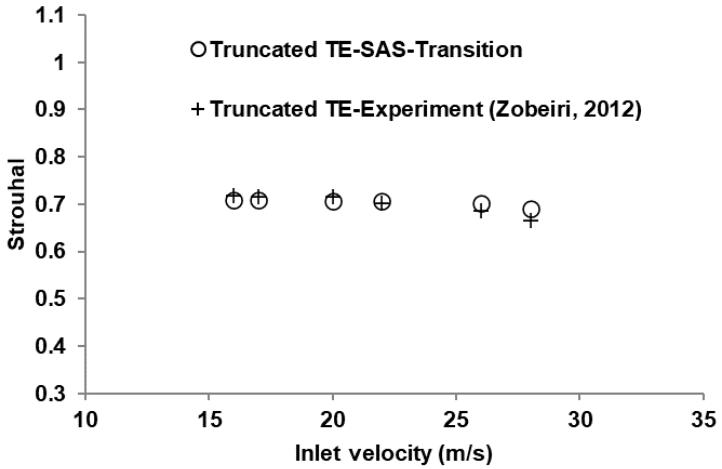

Figure 5.4 Strouhal number versus inlet velocity at lock-off condition

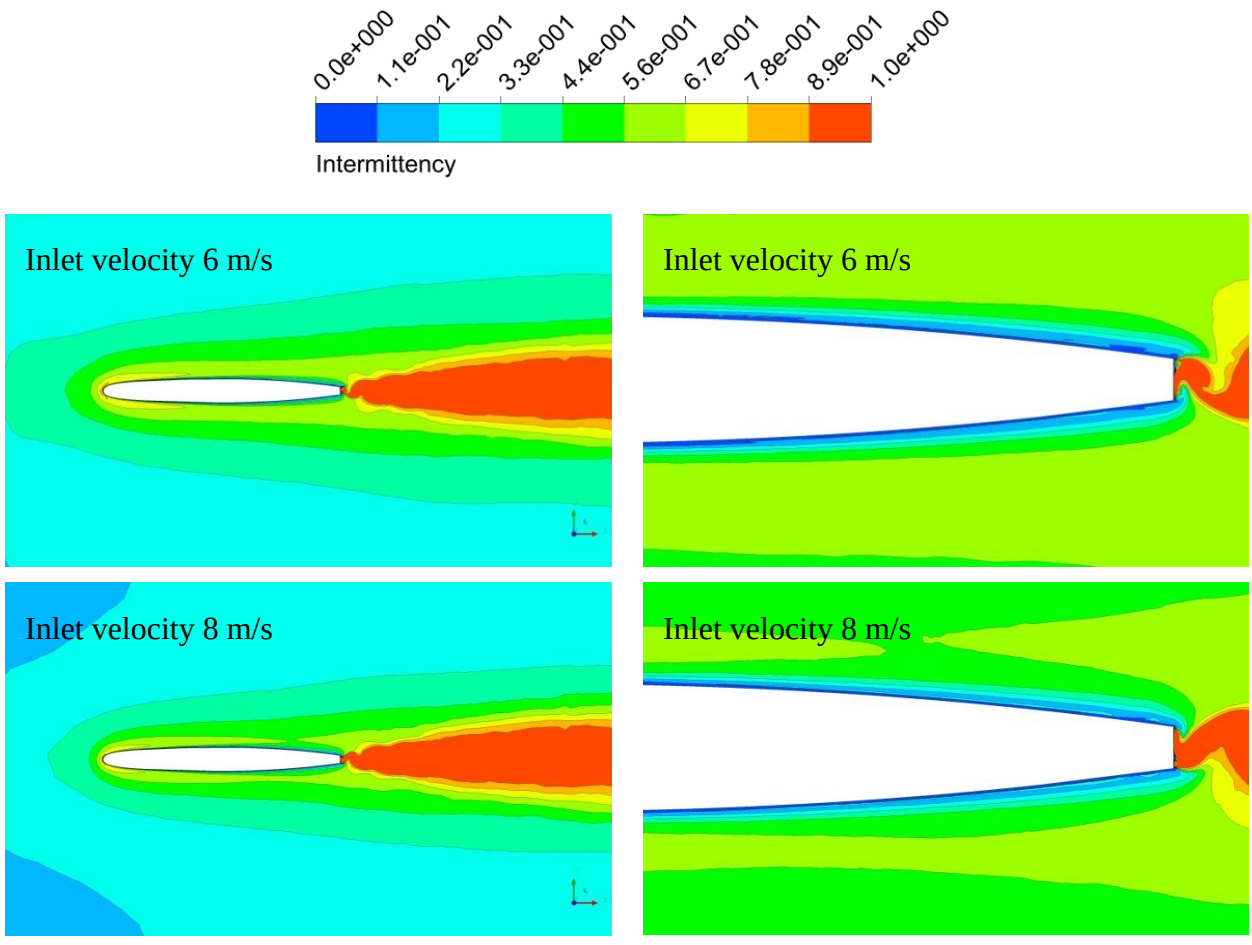

Figure 5.5 Instantaneous intermittency over the truncated hydrofoil for inlet velocities 6 and 8 m/s

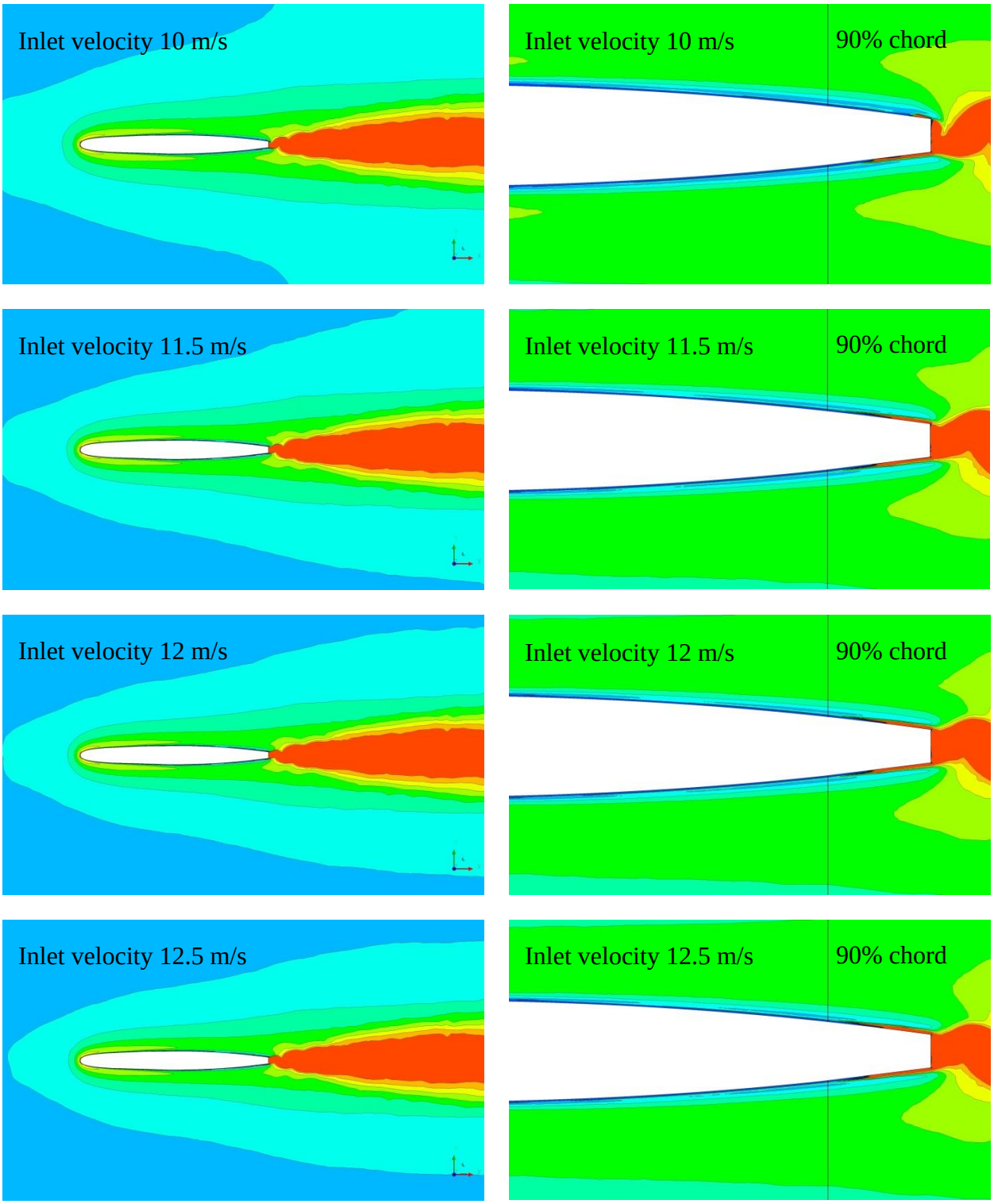

Figure 5.6 Instantaneous intermittency over the truncated hydrofoil for inlet velocities from 10 to 12.5 m/s

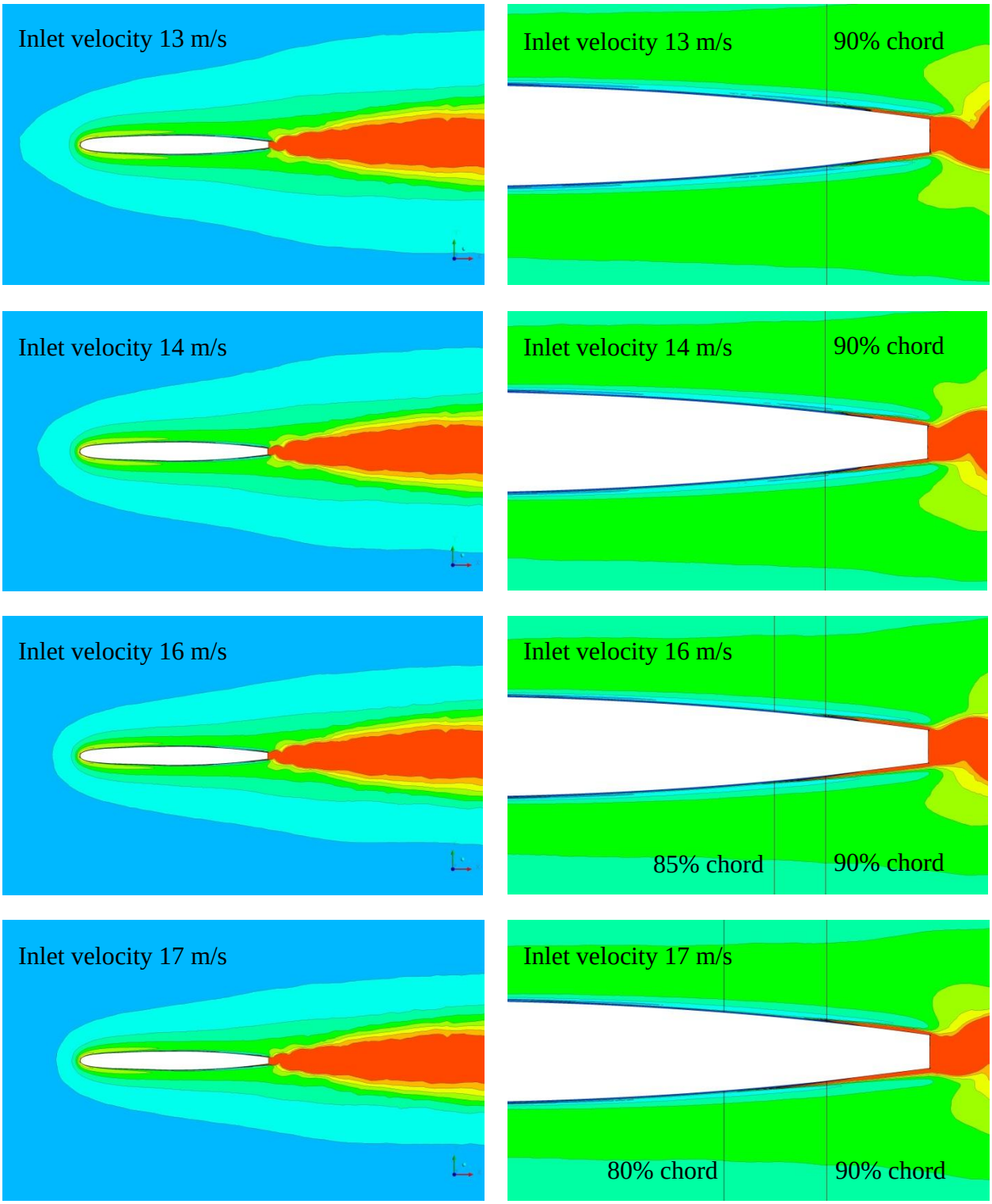

Figure 5.7 Instantaneous intermittency over the truncated hydrofoil for inlet velocities from 13 to 17 m/s

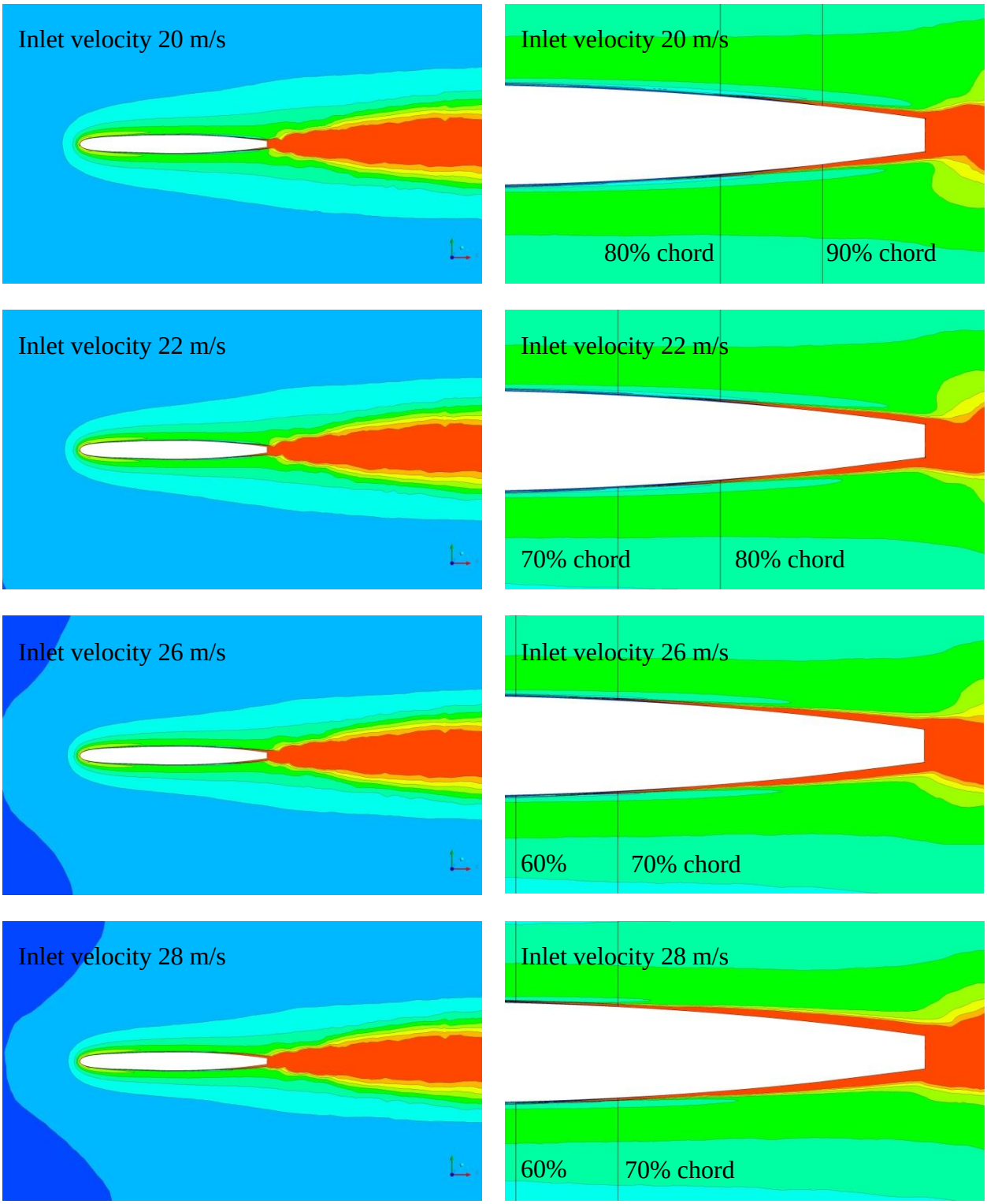

Figure 5.8 Instantaneous intermittency over the truncated hydrofoil for inlet velocities from 20 to 28 m/s

Figure 5.5 to 5.8 present the instantaneous intermittency on the truncated TE hydrofoil for several inlet velocities. The solid vertical lines shown in Figs 5.5 to 5.8 determine the percentages of the chord length showing the approximate location of the transition process on the hydrofoil. As the results show, the laminar boundary layer is dominant on the hydrofoil for inlet velocities of 6 and 8 m/s. A first sign of the turbulent boundary layer is diagnosed for an inlet velocity of 10 m/s, where there is a sharp transformation of the laminar to turbulent boundary layer at almost 95% of the chord length. The distance from where the turbulence boundary layer initiates to the trailing edge of the hydrofoil is not long enough to capture the complete transition behaviour. Although the first sign of transition was captured at this inlet velocity, the computed frequency is far from the experiment with 10% difference. This shows that the implemented model can predict the transition even in a short space at the end of trailing edge. However, due to the proximity to the lock-in region, the computed frequency is not accurate.

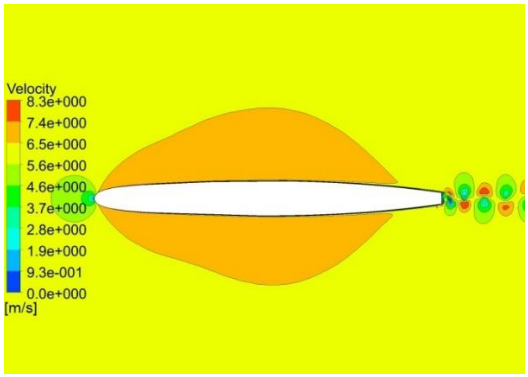

Inlet velocity: 6 m/s

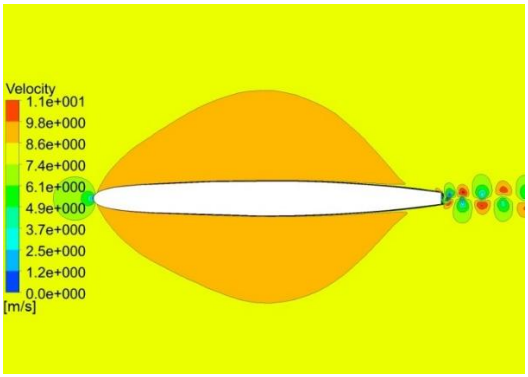

Inlet velocity: 8 m/s

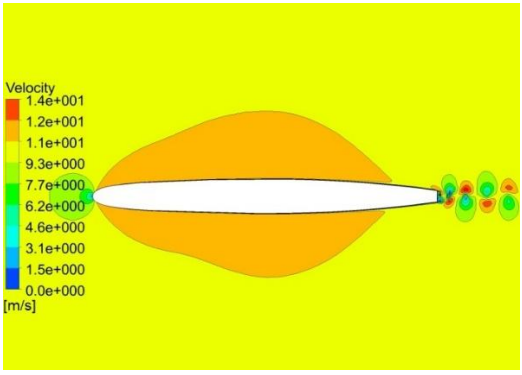

Inlet velocity: 10 m/s

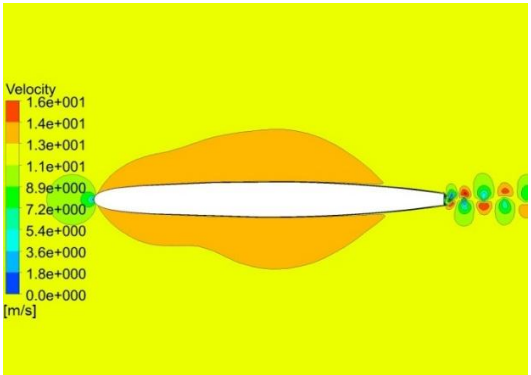

Inlet velocity: 11.5 m/s

Figure 5.9 Instantaneous velocity distribution for inlet velocities between 6 to 11.5 m/s

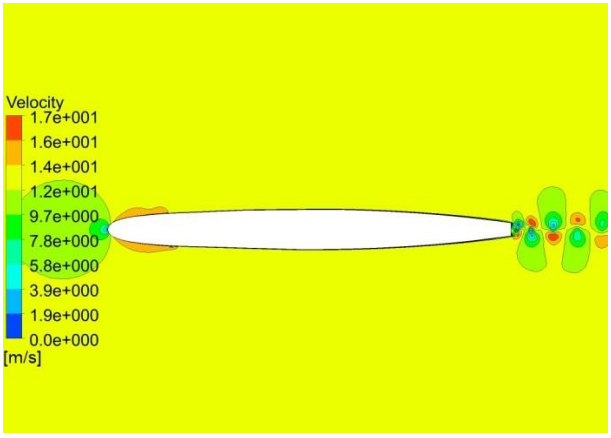

Inlet velocity: 12 m/s

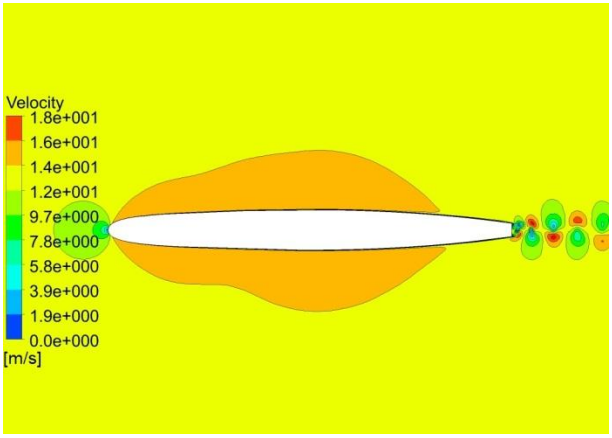

Inlet velocity: 12.5 m/s

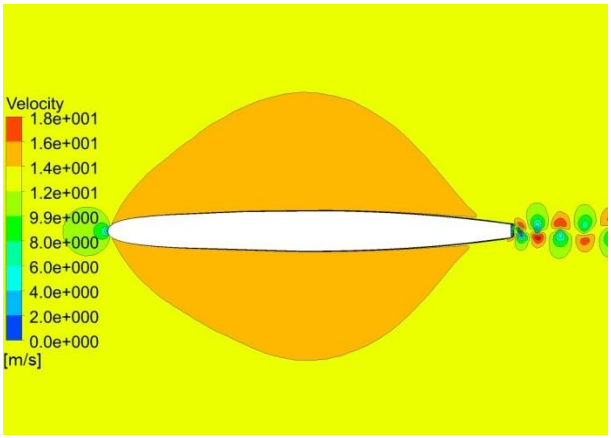

Inlet velocity: 13 m/s

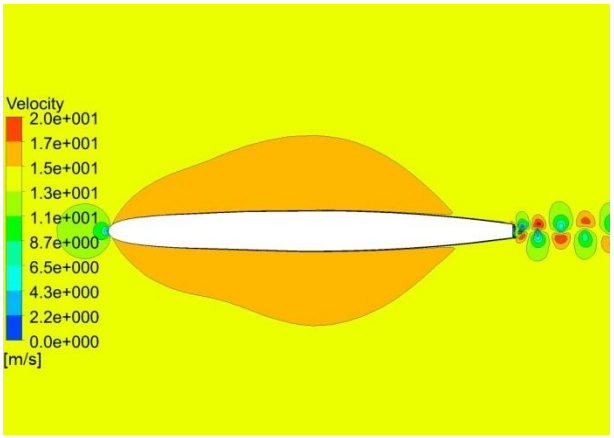

Inlet velocity: 14 m/s

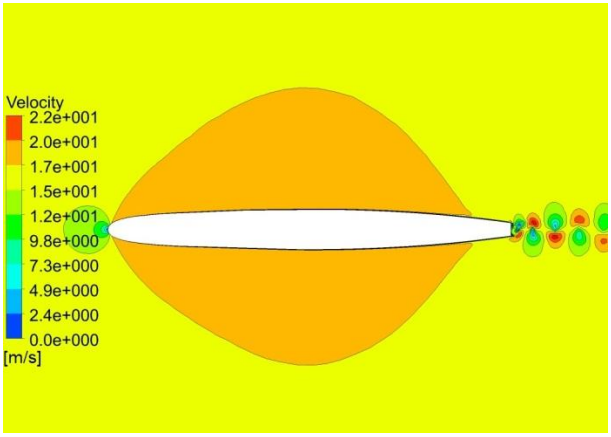

Inlet velocity: 16 m/s

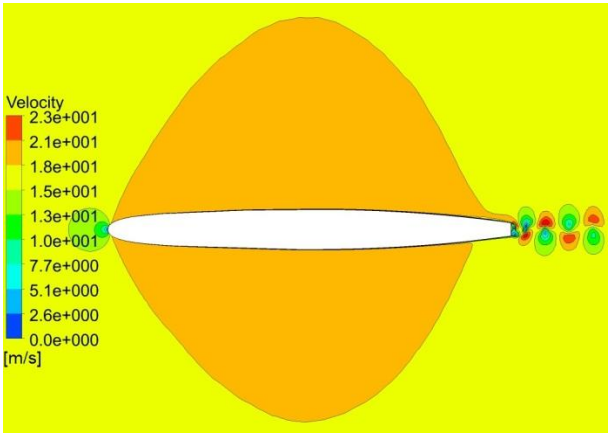

Inlet velocity: 17 m/s

Figure 5.10 Instantaneous velocity distribution on the truncated hydrofoil for inlet velocities between 12 to 17 m/s

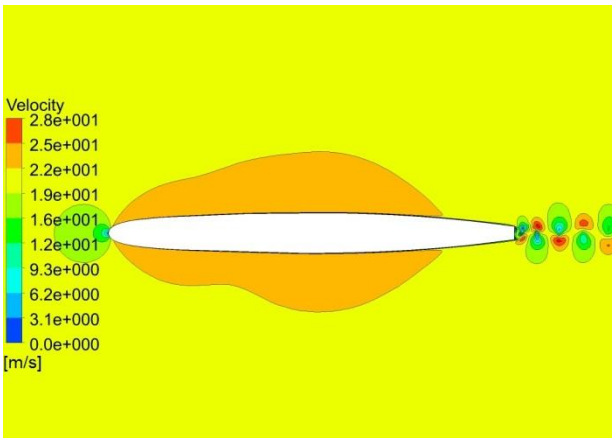

Inlet velocity: 20 m/s

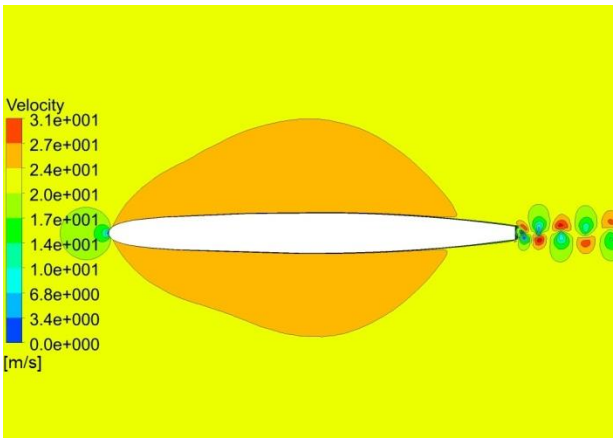

Inlet velocity: 22 m/s

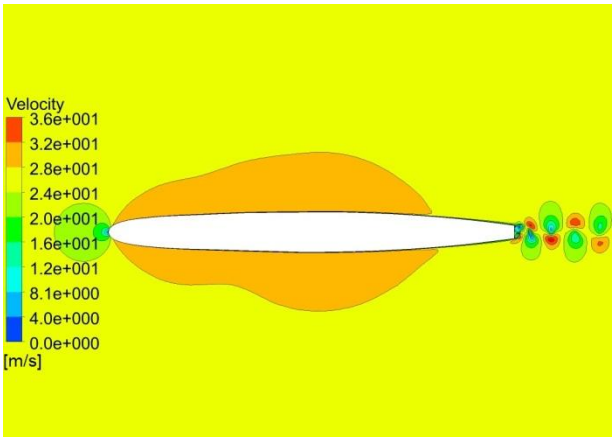

Inlet velocity: 26 m/s

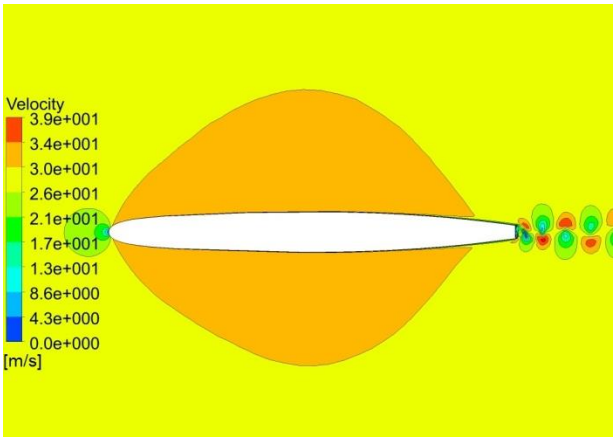

Inlet velocity: 28 m/s

Figure 5.11 Instantaneous velocity distribution on the truncated hydrofoil for inlet velocities between 20 to 28 m/s

As indicated in Figs. 5.5 to 5.8, the transition onset location moves towards the leading edge with increasing inlet velocity. For inlet velocities between 10 to 14 m/s, the transition occurs between 90 to 100% of the chord length, and for inlet velocities between 16 to 20 m/s, transition starts between 80 to 90% of the chord length. For inlet velocities between 26 to 28 m/s, initiation of the transition is observed in a region between 60 to 70% of the chord length. The distance where the transition process takes place is longer for higher inlet velocities.

Instantaneous velocity distribution at time t=0.45 s for different inlet velocities on a truncated hydrofoil are presented in Figs. 5.9 to 5.11. Vortex streets appear at the trailing edge of the hydrofoil. An equal distance between a vortex generated from lower section and two neighbouring vortices generated from the upper section is observed. The core size is equal for

vortices generated from the upper and lower sections of the hydrofoil. The size of vortices increases as they move along the wake.

Average y^+ value for different Reynolds numbers is presented in Fig. 5.12. As it shows, average y^+ values are less than one for the complete range of inlet velocities. It shows that the boundary layer mesh provides the characteristics required by the turbulence model in terms of having a y^+ value less than one. However, an ascending trend is observed when increasing the Reynolds number. This is due to the use of a single mesh with constant boundary layer mesh properties while the inlet velocity increases.

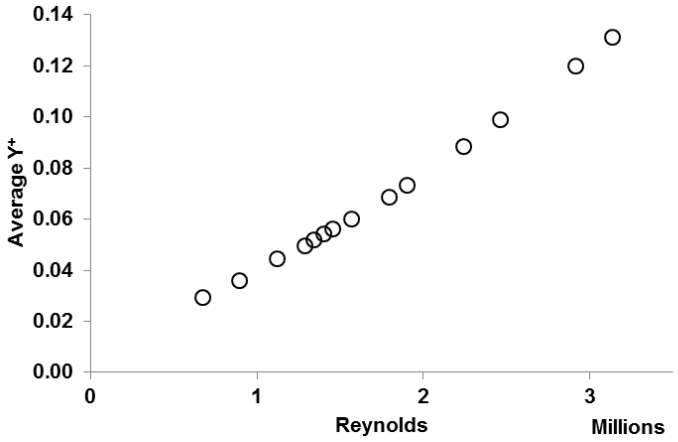

Figure 5.12 Average y^+ on the hydrofoil versus Reynolds number for the truncated trailing edge

5.2 Oblique trailing edge

Flow and frequency analysis on the NACA0009 hydrofoil with an oblique trailing edge was conducted by Zobeiri (2012), experimentally. A geometry similar to that for the truncated hydrofoil was used, except at the trailing edge, which was cut at around 93% of the chord length with an angle of 30^o, (see Fig. 5.13). Trailing edge thickness for the oblique trailing edge is almost a quarter of the one for the truncated trailing edge. Domain geometry and its discretization are similar to those used for the truncated trailing edge. Several inlet velocity conditions were simulated using the SAS-Transition turbulence model. Frequency predictions of the lift coefficient for a wide range of inlet velocities are presented in Figs. 5.14 and 5.15. Results indicate that the higher is the inlet velocity, the bigger is the vortex shedding frequency.

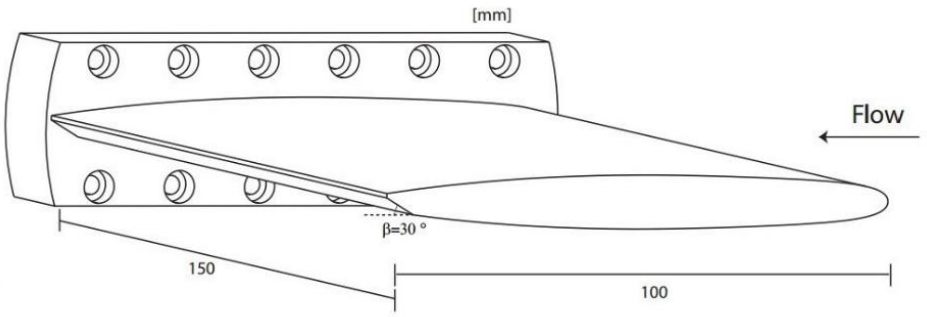

Figure 5.13 NACA0009 hydrofoil with oblique trailing edge (Zobeiri et al., 2012)

Figure 5.16 and Table 5.2 present a comparison between calculated frequencies for different inlet velocities and experimental data of Zobeiri (2012). All cases were modeled with low turbulent intensity. The unsteady simulations are initialized with a steady state solution with the same inlet velocity. As the results show, the numerical model predicts a linear relation between shedding frequency and inlet velocity, which is in a good agreement with the quasi-linear experimental data. The linear relationship between excitation frequency and inlet velocity is defined in Eq. 5.3. The least square method is used for the correlation coefficient, with a R^2 value of 0.9994.

$$F = 66.744U - 9.0907 \tag{5.2}$$

Based on the experiment, frequency trend shows two flat ranges, one between inlet velocities of 7 to 9 m/s and another between inlet velocities of 12 to 14 m/s. Zobeiri (2012) observed that when the inlet velocity is between 7 to 9 m/s, the vortex shedding frequency corresponds to half of the hydrofoil lock-in frequency. It was found that the oblique TE presents more vibration than the truncated hydrofoil due to the non-symmetric TE, which produces stronger harmonics and as a result of that, more excitation at resonance frequency. Resonant objects can have several resonance frequencies, especially at harmonics (multiples) of their strongest resonance frequency. The resonance frequency is related to different characteristics including, shape, size and material.

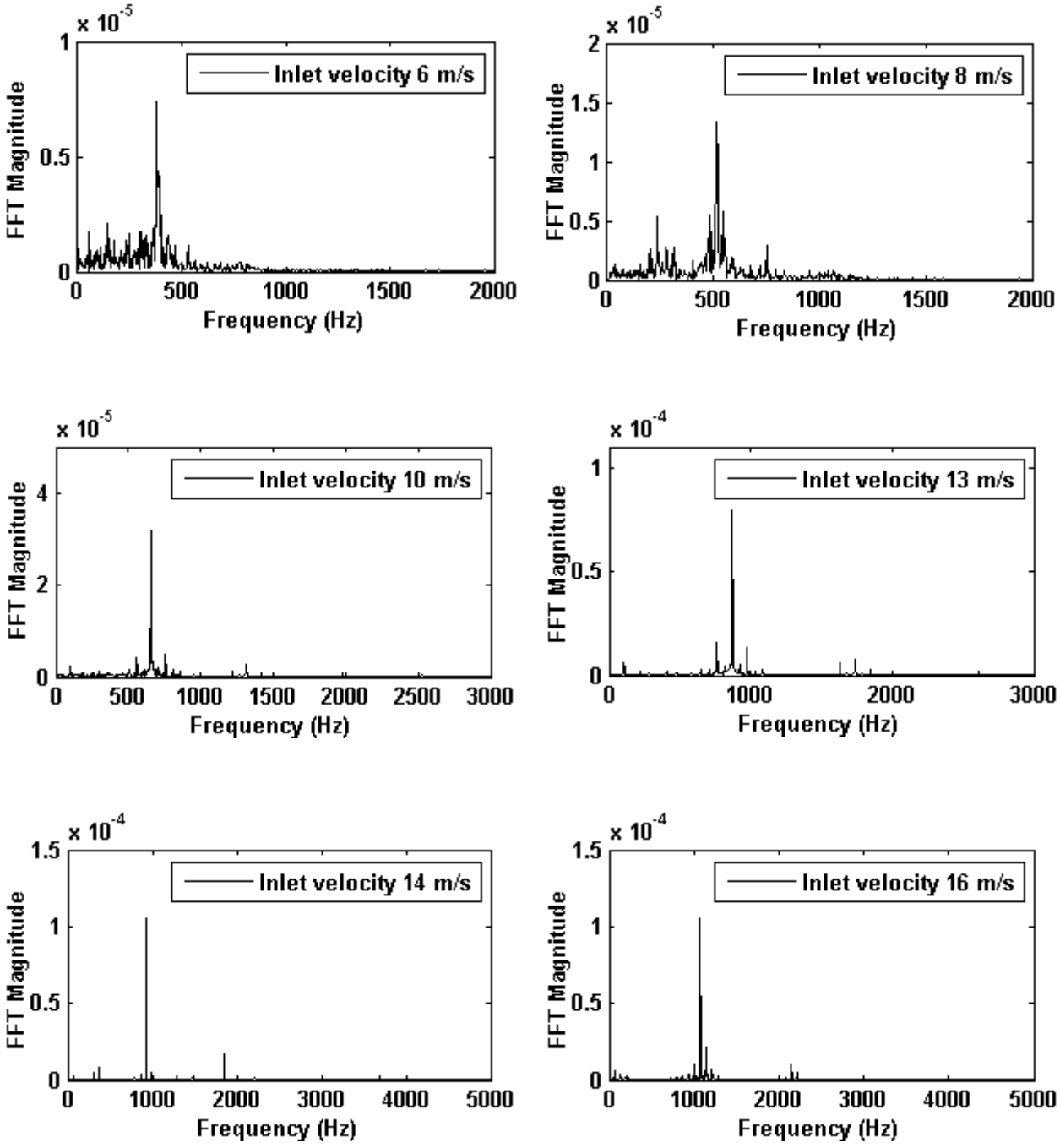

Figure 5.14 FFT calculation on the oblique trailing edge for inlet velocities from 6 to 16 m/s

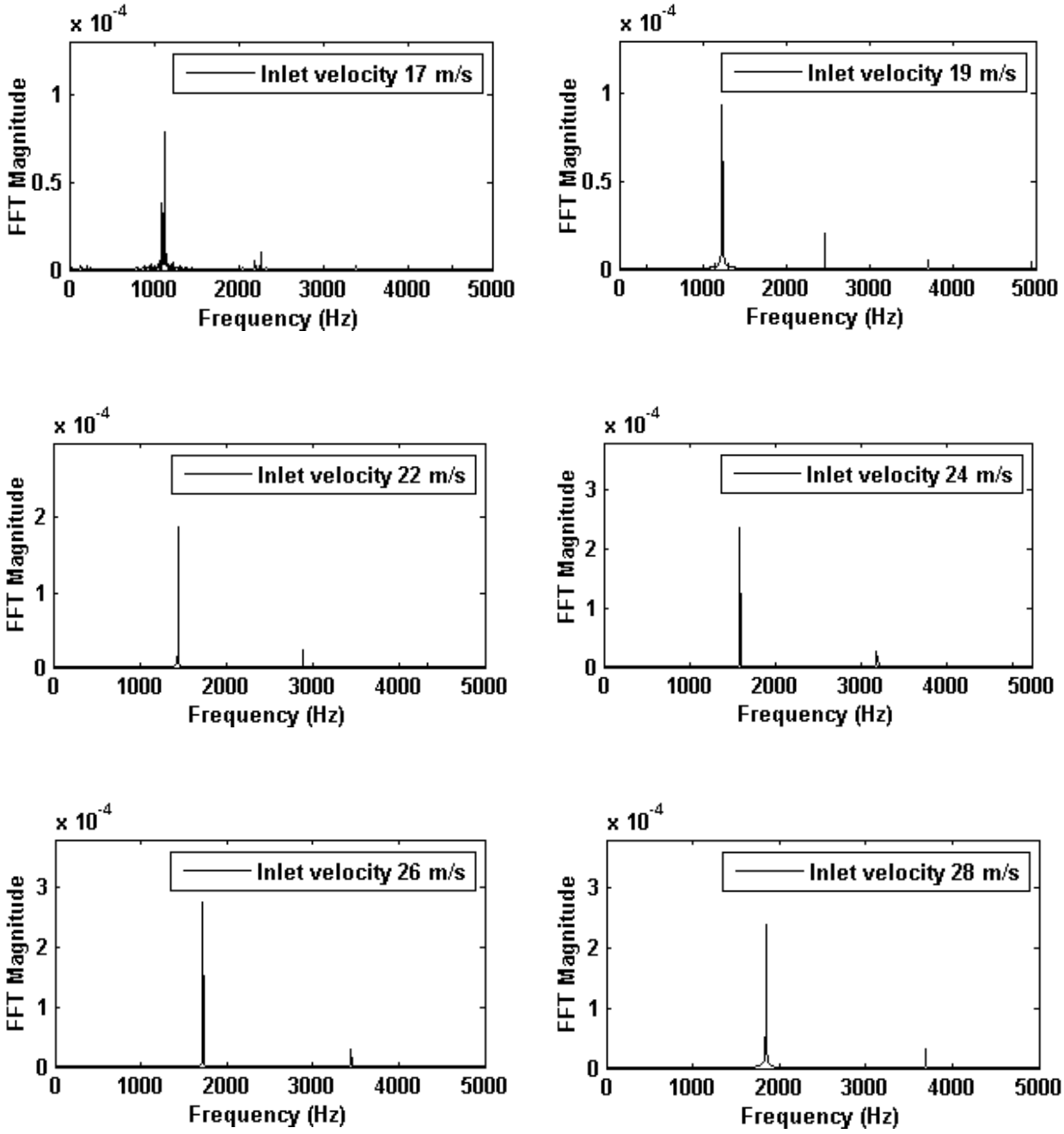

Figure 5.15 FFT calculation on the oblique trailing edge for inlet velocities from 17 to 28 m/s

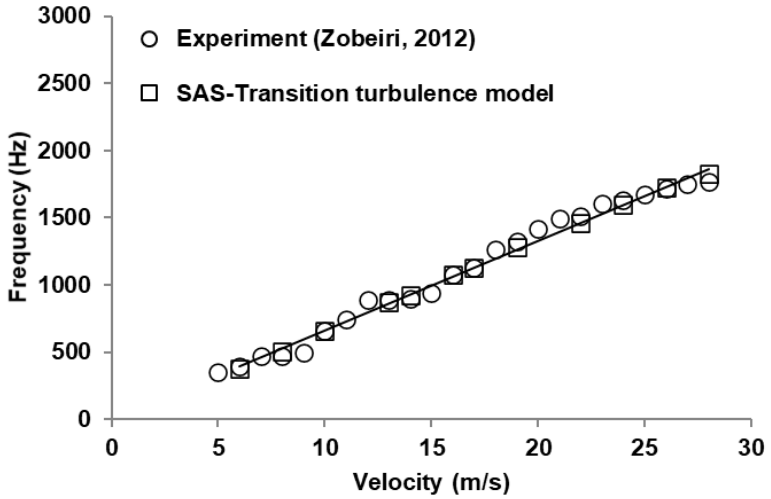

Figure 5.16 Frequency versus velocity for oblique TE

Table 5.2 Frequency versus velocity for oblique TE

Inlet Velocity (m/s)	Experimental Frequency (Hz)	SAS-Transition Frequency (Hz)	Error (%)
6	393	379	3.56
8	474	504	6.32
10	655	659	0.61
13	889	870	2.13
14	900	925	2.78
16	1075	1074	0.09
17	1128	1132	0.35
19	1324	1283	3.09
22	1511	1465	3.04
24	1635	1596	2.38
26	1720	1724	0.23
28	1768	1829	3.45

The maximum difference between CFD solutions and available data is observed at 8 m/s inlet velocity, with 6.3% error. The current investigation only includes CFD results, in which fluid-structure interaction is not considered. The highest difference between numerical results and experimental data could be due to the fact that the hydrofoil solid material and its interaction with the fluid are not modeled in the simulation. The lock-in region for the oblique TE happens for velocities around 12 to 14 m/s and the identified lock-off region is for inlet velocities higher than 15 m/s. It is suggested to consider higher inlet velocity flows when using oblique trailing edge to avoid dominant or lock-in frequency.

The Strouhal number, which is calculated using the hydrofoil maximum thickness versus inlet velocity, is presented in Fig. 5.17 at lock-off condition for an oblique trailing edge. Results show that there is a good agreement between numerical solution and available data. Both CFD solutions and experiment predict a maximum value for the Strouhal number with increasing the flow stream velocity. This is due to the development and evolution of the boundary layer shape with an increasing free stream velocity at the oblique TE in comparison to the truncated hydrofoil (Zobeiri, 2012). This is while the Strouhal number decreases with increasing flow inlet velocity for the truncated hydrofoil, as shown in Fig 5.4.

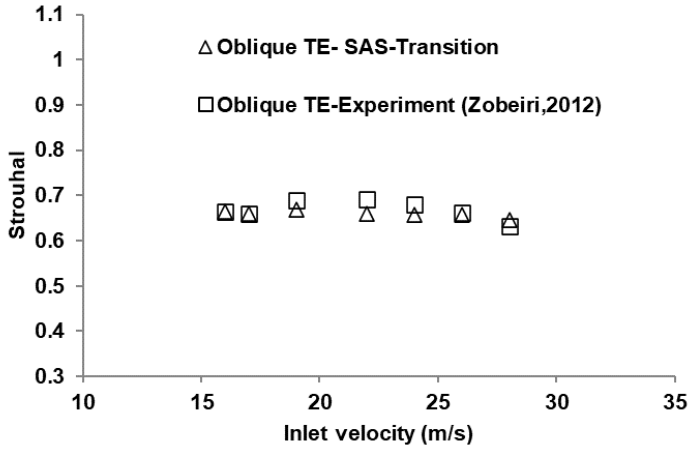

Figure 5.17 Strouhal versus inlet velocity at lock-off region for oblique TE

Instantaneous intermittency at time t=0.45 s for different inlet velocities over the oblique trailing edge is presented in Figs. 5.18 to 5.21. As shown, a laminar boundary layer is predicted for inlet velocities of 6 and 8 m/s. The first sign of a turbulent boundary layer is observed for an inlet velocity of 10 m/s, where the intermittency begins to increase at more than 90% of the chord length over the suction side of the hydrofoil. Transitional behavior on the pressure side of the hydrofoil happens at a much larger inlet velocity compared to that on the suction side. As an illustration, the first transitional sign on the pressure side of the hydrofoil is found for an inlet velocity of 16 m/s.

Increasing the inlet velocity above the lock-off area shows that the transitional boundary layer over the pressure side starts much closer to the leading edge compared to that initiated on the suction side. For example, the transition process for an inlet velocity of 28 m/s on the pressure side of the oblique trailing edge starts at more than 30% of the chord length, while it happens at

more than 70% of the chord length on the suction side. Thickness of the layer with the maximum intermittency, which represents the turbulent boundary layer, on the pressure side is higher than that on the suction side. It could be due to the collision between the vortices that are initiating from the suction and pressure sides of the oblique trailing edge, as observed by Zobeiri (2012). On the contrary, the transition processes take place at the same chord-wise locations over both sides of the truncated trailing edge.

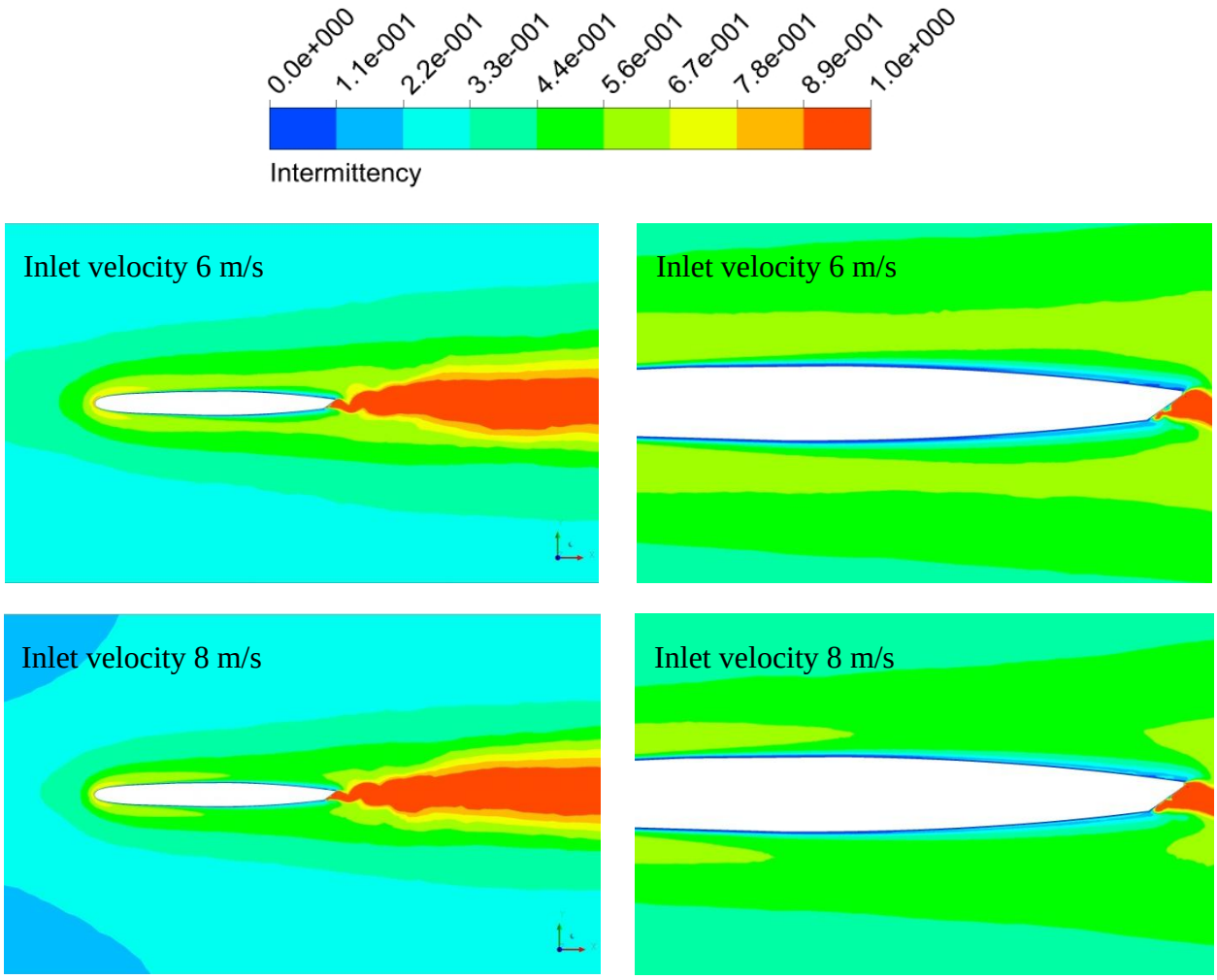

Figure 5.18 Instantaneous intermittency for oblique trailing edge for inlet velocities 6 and 8 m/s

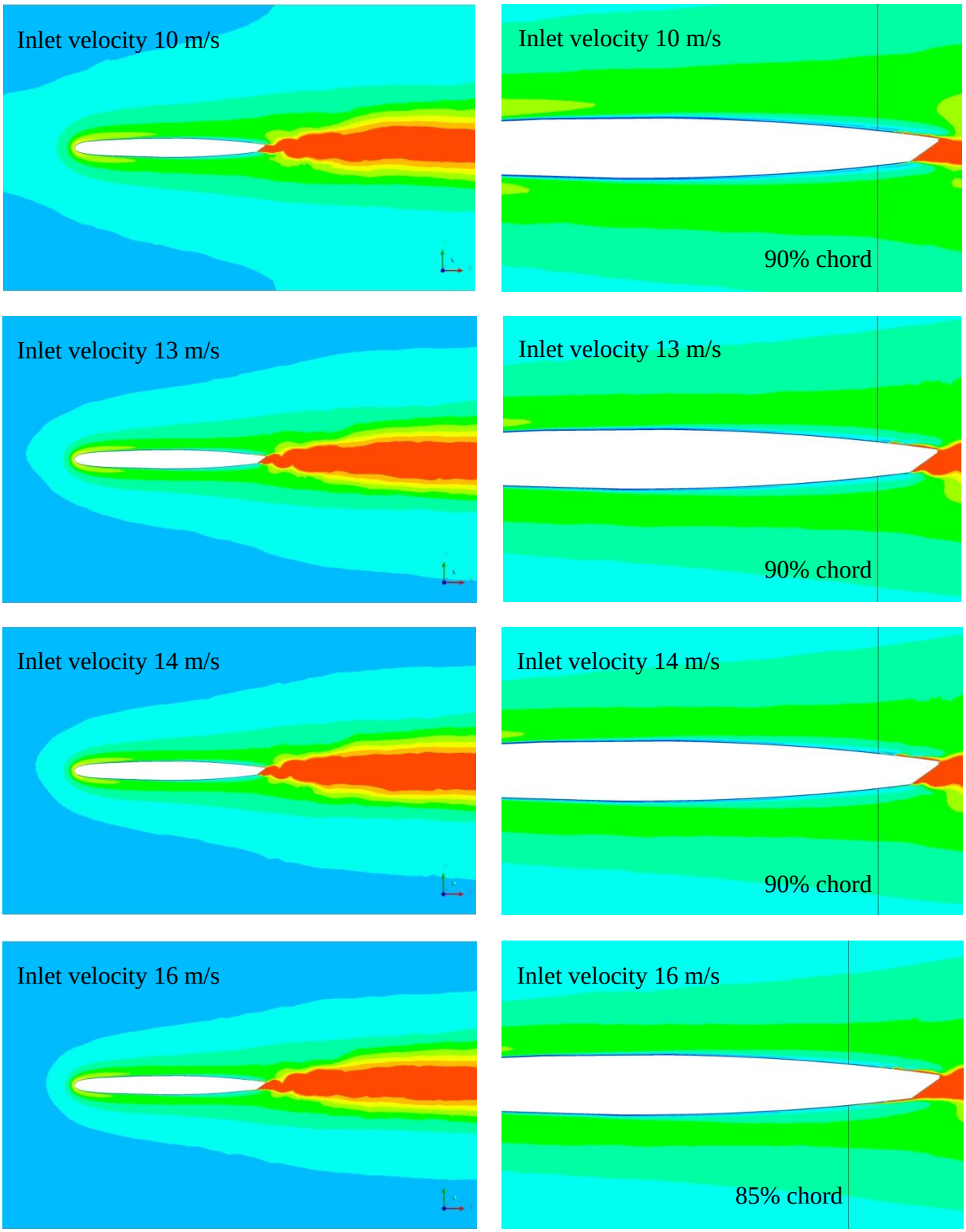

Figure 5.19 Instantaneous intermittency for oblique trailing edge for inlet velocities 10 to 16 m/s

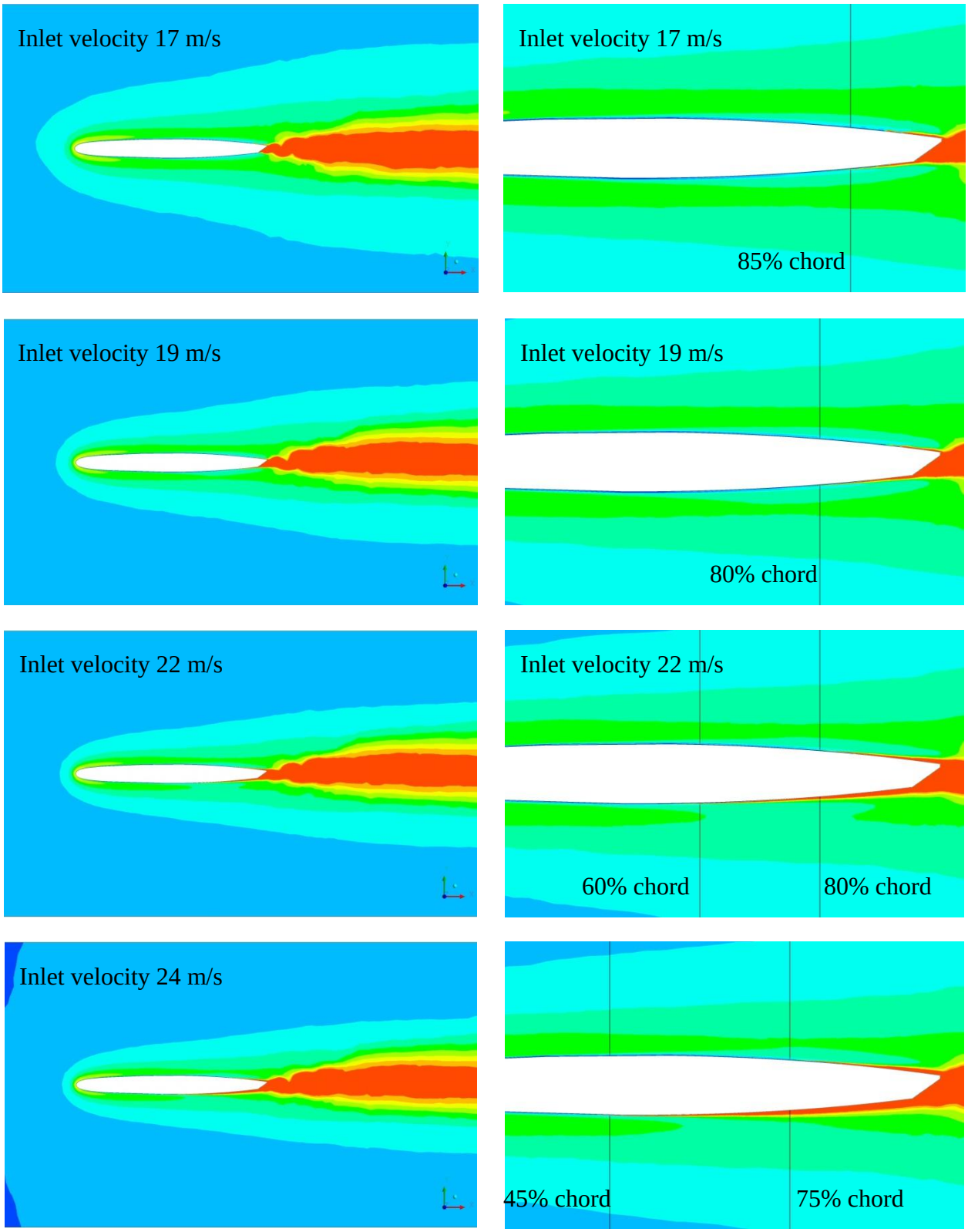

Figure 5.20 Instantaneous intermittency for oblique trailing edge for inlet velocities 17 to 24 m/s

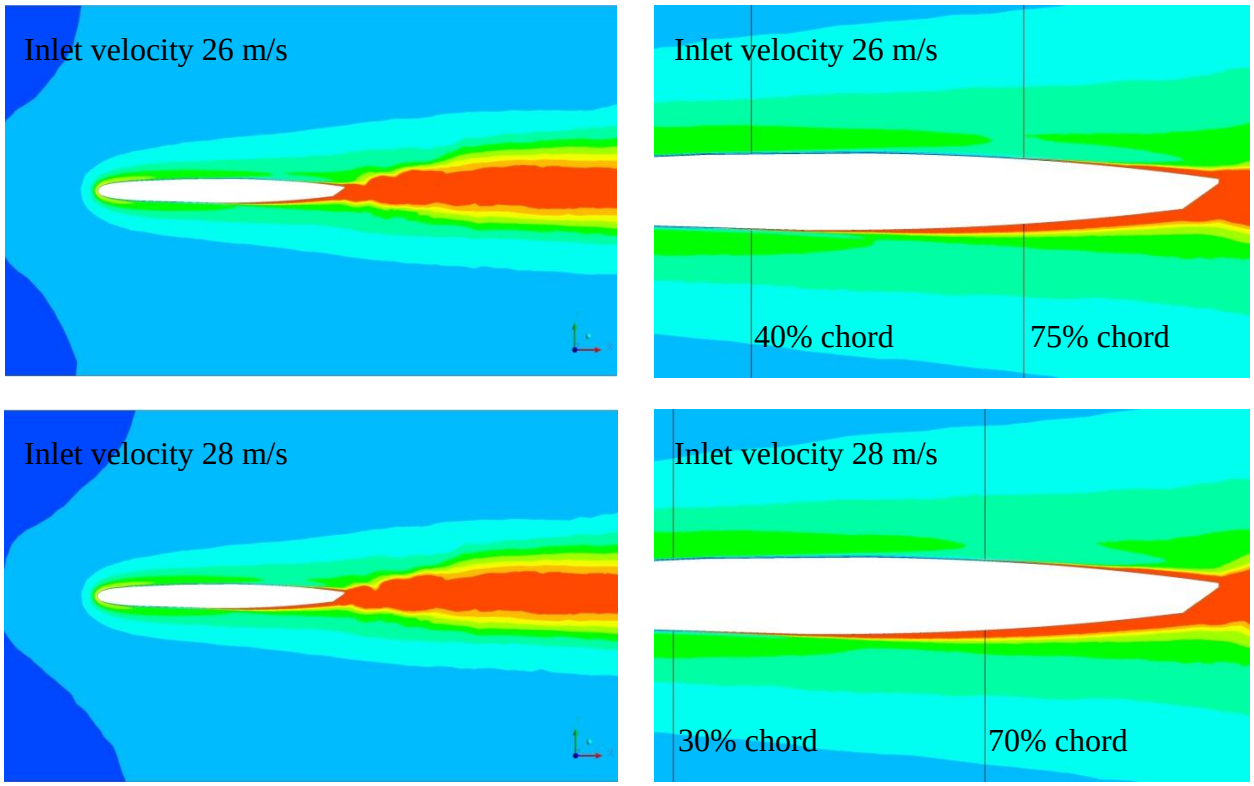

Figure 5.21 Instantaneous intermittency for oblique trailing edge for inlet velocities 26 and 28 m/s

Instantaneous velocity distributions at time t=0.45 s are presented in Fig. 5.22 to 5.23. Results show that the vortices detach from both sides of the trailing edge. The velocity distribution outside the boundary layer of the hydrofoil shows higher values on the pressure side than the one on the suction side. In contrary to the truncated trailing edge, an unequal distance between a vortex generated from the lower section and two neighbouring vortices generated from the upper section is observed near the Oblique trailing edge. However, these unequal distances diminish far from the oblique trailing edge and reorganize an alternate shedding similar to the ones originating from a blunt trailing edge. In addition, the size of vortices generated from the lower section of the hydrofoil is bigger than the ones originating from the upper section for the oblique trailing edge.

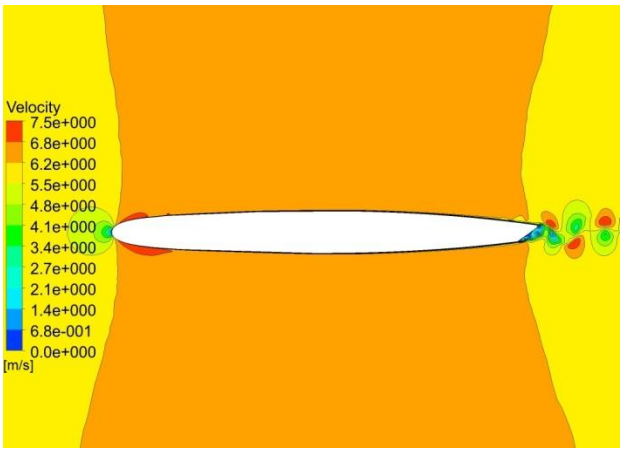

Inlet velocity: 6 m/s

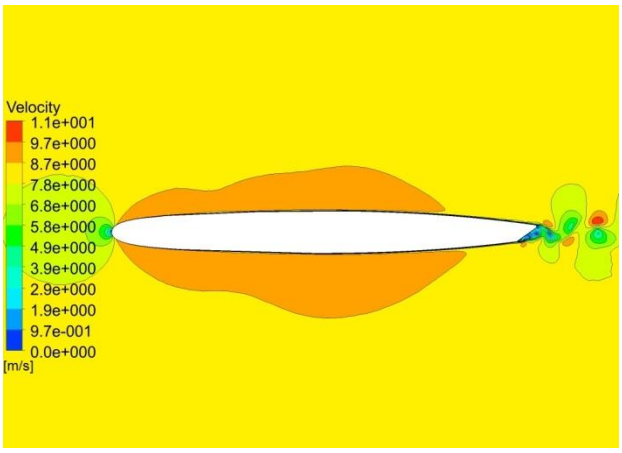

Inlet velocity: 8 m/s

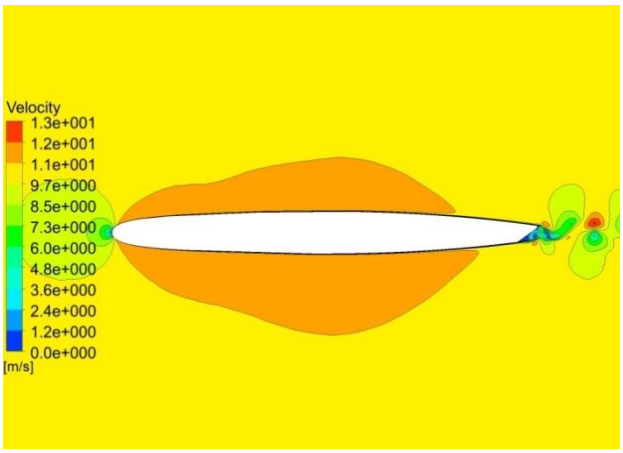

Inlet velocity: 10 m/s

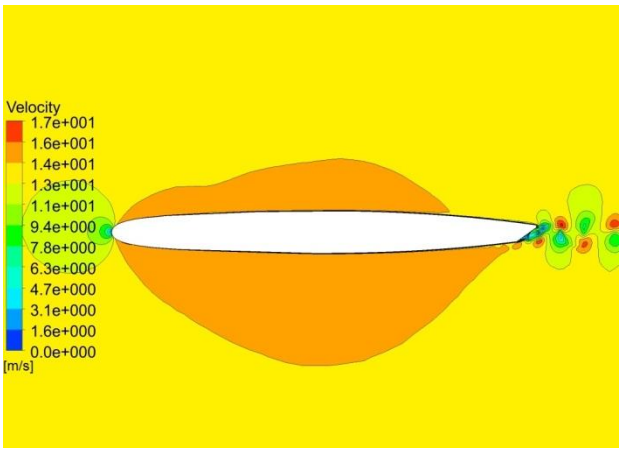

Inlet velocity: 13 m/s

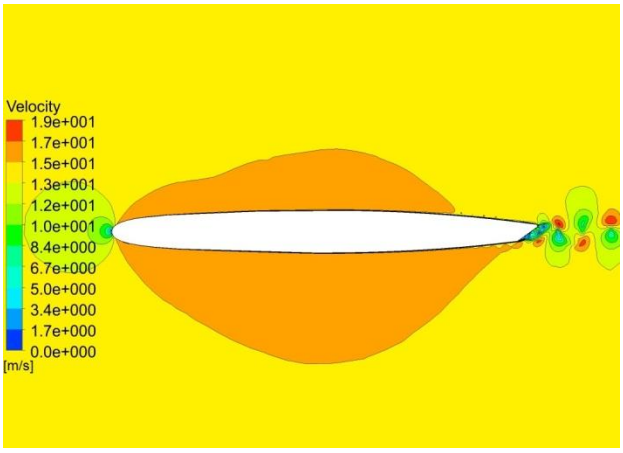

Inlet velocity: 14 m/s

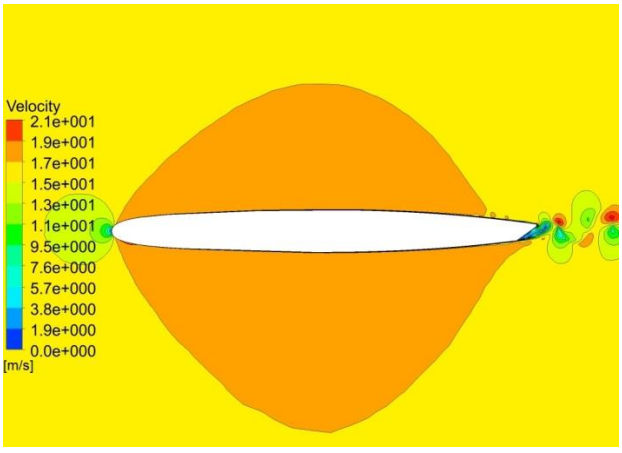

Inlet velocity: 16 m/s

Figure 5.22 Instantaneous velocity distribution over the oblique trailing edge for inlet velocities 6 to 16 m/s

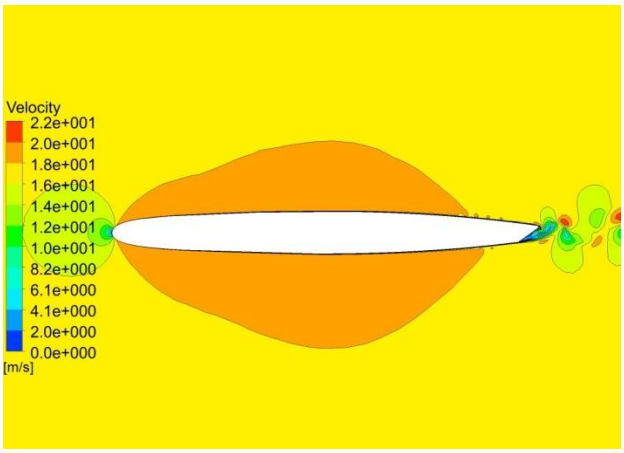

Inlet velocity: 17 m/s

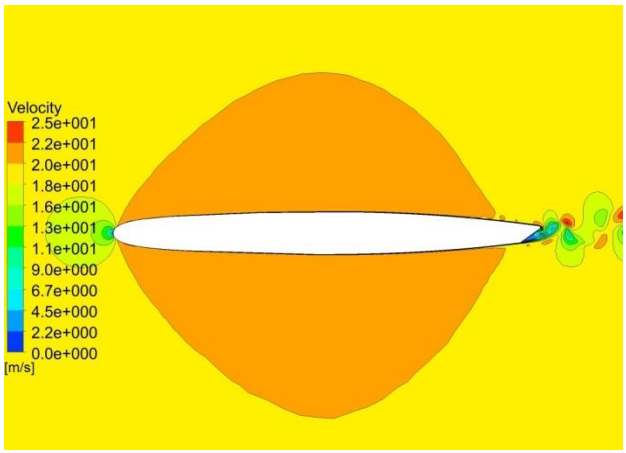

Inlet velocity: 19 m/s

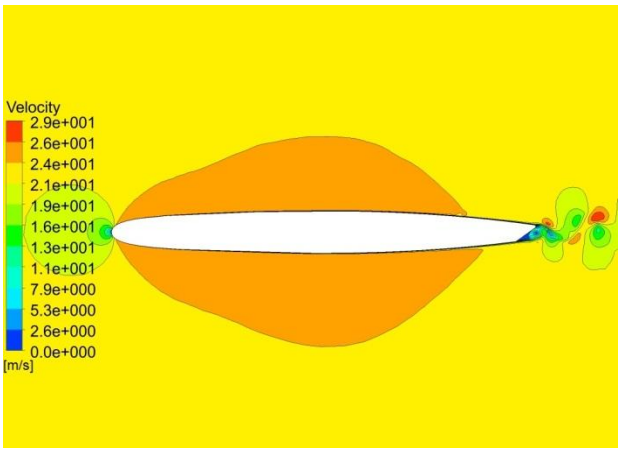

Inlet velocity: 22 m/s

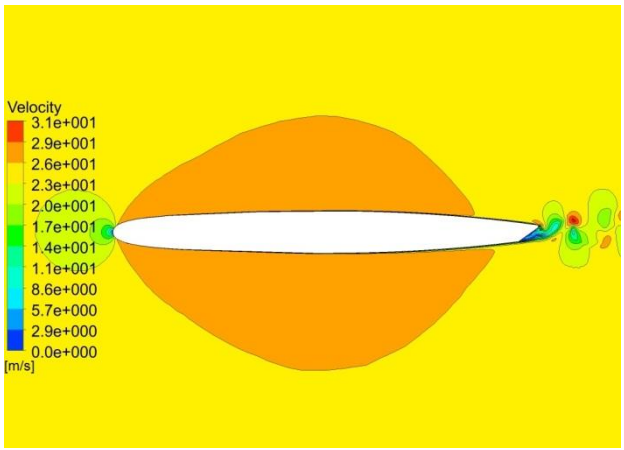

Inlet velocity: 24 m/s

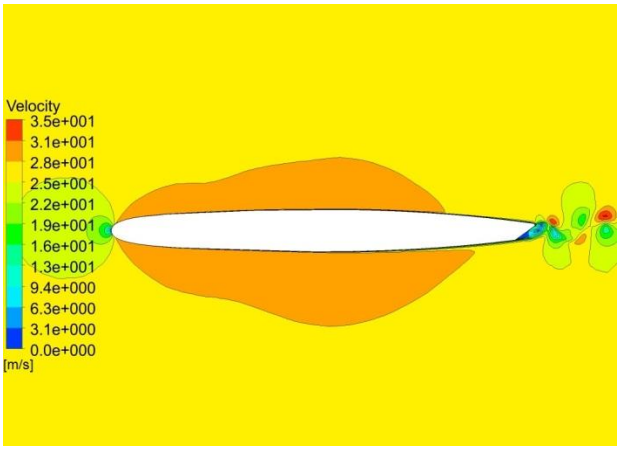

Inlet velocity: 26 m/s

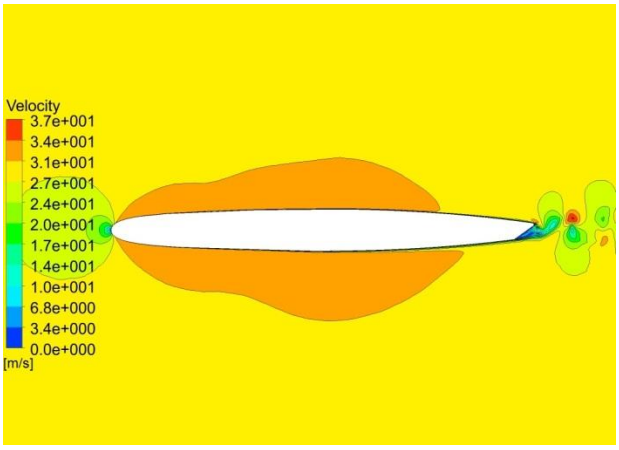

Inlet velocity: 28 m/s

Figure 5.23 Instantaneous velocity distribution over the oblique trailing edge for inlet velocities 17 to 28 m/s

The average y^+ values for different Reynolds numbers over the oblique trailing edge are presented in Fig. 5.24. As it shows, the average y^+ values are less than one for the complete range of considered inlet velocities. It shows that the boundary layer mesh matches the requirement of the turbulence model in terms of having a y^+ value less than one. A similar behaviour was observed for the truncated trailing edge.

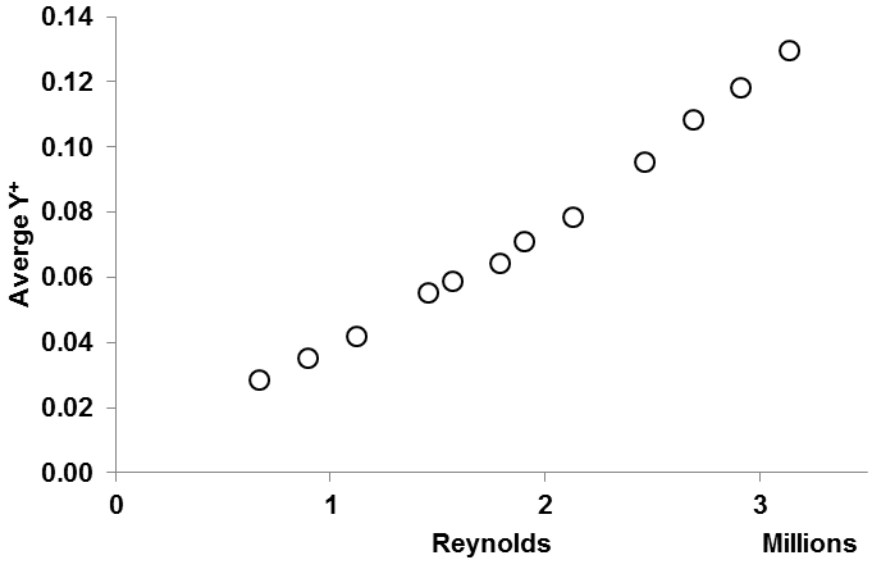

Figure 5.24 Average y^+ versus Reynolds over oblique TE

5.3 Limitations

The implemented transitional model includes a limitation in terms of domain with moving frame of reference. The $\gamma - \widetilde{Re}_{\theta t}$ model is not considered to satisfy the Galilean invariance, which limits the transitional model to be used for walls that are moving (Sheng, 2017).

In general, the implemented model shows a high protentional in capturing the laminar to turbulent transition process. It requires a fine boundary layer mesh to capture the small-scale transitional flow characteristics. Mesh dependency was observed in capturing the transition region over the steady state flat plate in chapter 4. However, the implemented transitional model presented an acceptable performance on capturing the transitional region for unsteady flows over the stay vane with two different trailing edges.

The implemented model combines two more equations into the SST-SAS turbulence model. This increases the computational time and cost. Using a model that can predict all the three stages of a

flow (laminar, transitional, and turbulent) is beneficial, when the nature of the flow is unknown. Depending on the domain and mesh, one needs to consider the additional computational time that the implemented model brings.

5.4 Summary

The implemented transition model was tested with two different trailing edge geometries on the NACA0009 hydrofoil over a wide range of inlet velocities. Results show that the implemented model can successfully predict the transition onset location with both geometries and different inlet conditions. Even though one mesh is used for all the geometries and inlet condition, the shedding frequencies were predicted with an excellent agreement compared to the experimental data especially in the lock-off region for both trailing edge geometries. The major differences were observed close to the lock-in region where the resonance frequency is dominant. This could be due to solving only the flow effect and not considering the fluid-structure interaction during numerical simulations.

CHAPTER 6 CONCLUSION AND RECOMMENDATIONS FOR FUTURE WORK

6.1 Conclusion

This thesis has proposed and evaluated the implementation of a transitional turbulence model by coupling an advanced transitional model, $\gamma - \widetilde{Re}_{\theta t}$, with the dynamically adapted turbulence model SST-SAS to capture the transitional flow features and shedding frequencies over a (NACA0009) hydrofoil. The transitional turbulence model was implemented within an open-source finite volume-based CFD code, OpenFOAM. The implemented model was first validated and verified with different transitional flows, including natural and bypass transition over a flat plate. Numerical results were compared to experimental data on calculation of friction coefficient and turbulence intensity. A very good agreement was observed between the current results and available data.

The main outcome of the current investigation was to investigate the transition onset location and shedding frequency of two-dimensional hydrofoils in URANS viscous flows at high Reynolds numbers. Flow properties such as shedding frequency, transition onset location and velocity profile were evaluated during the validation process. In general, very good agreement was observed when comparing to available experimental data. Results determined that the present methodology has been able to improve the accuracy of the numerical simulations compared to a similar transitional model coupled with the primarily adapted URANS turbulence model, SST.

Wide range of flow velocities with two different trailing edge configurations have been evaluated to investigate the response of the implemented transitional turbulence model on shedding frequency prediction and transition onset location with respect to different operating conditions and geometries. Results show that the implemented model predicts a linear relationship between the inlet velocity and shedding frequency, while experimental data shows a quasi-linear relation. The major differences were observed close to the lock-in region where the resonance frequency is dominant. This could be due to solving only the flow effect and not considering the fluid-structure interaction during numerical simulations. However, the implemented model presented acceptable results for predicting the Strouhal number in the lock-off region. The implemented transitional turbulence model has also shown that it can distinguish laminar, laminar-turbulent

transition and turbulent boundary layers. A good agreement has been observed for the prediction of the transition onset location compared to the experiment.

The implemented transitional model includes a limitation in terms of domain with moving frame of reference. The $\gamma - \widetilde{Re}_{\theta t}$ model is not considered to satisfy the Galilean invariance. It also requires a fine boundary layer mesh to capture the small-scale transitional flow characteristics. Mesh dependency was observed in capturing the transition region over the steady state flat plate.

6.2 Recommendations for future work

Regarding the proposed methodology for modeling transitional flow and its implementation for shedding frequency prediction at high Reynolds numbers, the following subjects are recommended for future works;

- To extend the verification and validation process, it is recommended to use the method of manufactured solution in another thesis. The future study could be extended by investigating the order of accuracy.
- For industrial applications, additional studies are needed to analyze the flow induced vibration over a complete 3D geometry using the proposed methodology and investigate the shedding frequency prediction and transitional flow characteristics.
- The maximum difference in excitation frequency between current numerical modeling and experimental data was observed close to the lock-in condition, where the vortex-induced vibration frequency coincide with the hydrofoil natural frequency; and it is locked on a range of free-stream velocities. Employing a fluid-structure interaction methodology could provide more insight about the prediction of resonance and prevent any possible hazard in industrial applications. Utilizing a fluid-structure interaction methodology could involve a less costly approach, one-way coupling, or a more detailed analysis such as two-way coupling.
- Further investigation is needed to optimize the shape of hydrofoil trailing edge using the proposed method to find the minimum flow-induced vibration without changing the hydrodynamic performances. The future study can be extended by evaluating the performance of implemented model with a Donaldson TE and compare the results with

the available experimental data. This can be considered as a replacement for costly experimental investigations.

- Although the transitional flow was relatively complex, the unsteady flow simulations were considered as cavitation free regimes. Saying that, for industrial applications the cavitation process is inevitable. Further studies are suggested to analyze the cavitation process synchronized with transitional features at high Reynolds number and investigate the shedding frequency prediction.

BIBLIOGRAPHY

Aït Bouziad, Y. (2005). *Physical modelling of leading edge cavitation computational methodologies and application to hydraulic machinery.* (PhD), EPFL,

Anagnostopoulos, P. (2003). Flow-Induced Vibrations in Engineering Practice. Edited by P. ANAGNOSTOPOULOS. WIT Press, 2002. 388 pp. ISBN 1-85312-644-6. *Journal of Fluid Mechanics, 475*, 409-412. doi:10.1017/s0022112002293374

Anagnostopoulos, P., & Bearman, P. W. (1992). Response characteristics of a vortex-excited cylinder at low reynolds numbers. *Journal of Fluids and Structures, 6*(1), 39-50. doi:10.1016/0889-9746(92)90054-7

Aslam Noon, A., & Kim, M.-H. (2017). Erosion wear on Francis turbine components due to sediment flow. *Wear, 378-379*, 126-135. doi:https://doi.org/10.1016/j.wear.2017.02.040

Ausoni, P. (2009). *Turbulent vortex shedding from a blunt trailing edge hydrofoil.* (Ph.D. Theses), Lausanne, EPFL, (4475)

Bahrami, S. (2015). *Multi-Fidelity Design Optimization of Francis Turbine Runner Blades.* (PhD thesis), École Polytechnique de Montréal,

Bearman, P. W. (1984). Vortex Shedding from Oscillating Bluff Bodies. *Annual Review of Fluid Mechanics, 16*(1), 195-222. doi:10.1146/annurev.fl.16.010184.001211

Bernard, P. S. (2013). Vortex Dynamics in Transitional and Turbulent Boundary Layers. *AIAA Journal, 51*(8), 1828-1842. doi:10.2514/1.j051811

Bernd, J., & Riedelbauch, S. (2015). *Numerical investigation of influence of runner gap for a low head turbine using hybrid RANS-LES turbulence model*. Paper presented at the Cavitation and dynamic problems.

Boris, J. P., & Book, D. L. (1973). Flux-corrected transport. I. SHASTA, a fluid transport algorithm that works. *Journal of Computational Physics, 11*(1), 38-69. doi:https://doi.org/10.1016/0021-9991(73)90147-2

Bredberg, J. (2000). *On the wall boundary condition for turbulence models*. Retrieved from CHALMERS UNIVERSITY OF TECHNOLOGY:

Cadiou, A., Hanjalić, K., & Stawiarski, K. (2004). A two-scale second-moment turbulence closure based on weighted spectrum integration. *Theoretical and Computational Fluid Dynamics, 18*(1), 1-26. doi:10.1007/s00162-004-0118-4

Castro, O., Ferretti, A. P., & Devinar, L. (2008). *The application of state of art CFD tools at the hydraulic turbine design*. Paper presented at the 24th Symposium on Hydraulic Machinery and Systems, , FOZ DO IGUASSU.

Chen, J., Li, Y. J., & Liu, Z. Q. (2018). Large eddy simulation of boundary layer transition flow around NACA0009 blunt trailing edge hydrofoil at high Reynolds number. *IOP Conference Series: Earth and Environmental Science, 163*(1), 012044.

Chen, T., Zhang, Y., & Li, S. (2016). Instability of large-scale prototype Francis turbines of Three Gorges power station at part load. *Proceedings of the Institution of Mechanical*

Engineers, Part A: Journal of Power and Energy, 230(7), 619-632. doi:10.1177/0957650916661638

Choi, H.-J., Zullah, M. A., Roh, H.-W., Ha, P.-S., Oh, S.-Y., & Lee, Y.-H. (2013). CFD validation of performance improvement of a 500 kW Francis turbine. *Renewable Energy, 54*, 111-123. doi:https://doi.org/10.1016/j.renene.2012.08.049

Coles, D. (1956). The law of the wake in the turbulent boundary layer. *Journal of Fluid Mechanics, 1*(2), 191-226. doi:Doi: 10.1017/s0022112056000135

D'Agostini Neto, A., & Saltara, F. (2009). Study of Stay Vanes Vortex-Induced Vibrations with different Trailing-Edge Profiles Using CFD. *International Journal of Fluid Machinery and Systems, 2*(4), 363-374. doi:10.5293/ijfms.2009.2.4.363

D'Alessandro, V., Binci, L., Montelpare, S., & Ricci, R. (2018). On the development of OpenFOAM solvers based on explicit and implicit high-order Runge–Kutta schemes for incompressible flows with heat transfer. *Computer Physics Communications, 222*, 14-30. doi:https://doi.org/10.1016/j.cpc.2017.09.009

Devals, C., Vu, T. C., Zhang, Y., Dompierre, J., & Guibault, F. (2016). Mesh convergence study for hydraulic turbine draft-tube. *IOP Conference Series: Earth and Environmental Science, 49*(8), 082021.

Di Domenico, N., Groth, C., Wade, A., Berg, T., & Biancolini, M. E. (2018). Fluid structure interaction analysis: vortex shedding induced vibrations. *Procedia Structural Integrity, 8*, 422-432. doi:https://doi.org/10.1016/j.prostr.2017.12.042

Dick, E., & Kubacki, S. (2017). Transition Models for Turbomachinery Boundary Layer Flows: A Review. *International Journal of Turbomachinery, Propulsion and Power, 2*(2). doi:10.3390/ijtpp2020004

Dompierre, J., & Labbé, P. (2001). *Object-Oriented Remeshing Toolkit (OORT)*. Retrieved from Montréal, QC, Canada.:

Dörfler, P., Sick, M., & Coutu, A. (2013). *Flow-Induced Pulsation and Vibration in Hydroelectric Machinery*: Springer, London.

Dreeben, T. D., & Pope, S. B. (1997). Wall-function treatment in pdf methods for turbulent flows. *Physics of Fluids, 9*(9), 2692-2703. doi:10.1063/1.869381

Durbin, P. A., Jacobs, R. G., & Wu, X. (2002). DNS of Bypass Transition. In B. E. Launder & N. D. Sandham (Eds.), *Closure Strategies for Turbulent and Transitional Flows* (pp. 449-463). Cambridge: Cambridge University Press.

Egorov, Y., & Menter, F. (2008, 2008//). *Development and Application of SST-SAS Turbulence Model in the DESIDER Project.* Paper presented at the Advances in Hybrid RANS-LES Modelling, Berlin, Heidelberg.

Egorov, Y., Menter, F. R., Lechner, R., & Cokljat, D. (2010). The Scale-Adaptive Simulation Method for Unsteady Turbulent Flow Predictions. Part 2: Application to Complex Flows. *Flow, Turbulence and Combustion, 85*(1), 139-165. doi:10.1007/s10494-010-9265-4

Eichhorn, M., Doujak, E., & Waldner, L. (2016). Investigation of the fluid-structure interaction of a high head Francis turbine using OpenFOAM and Code_Aster. *IOP Conference Series: Earth and Environmental Science, 49*(7), 072005.

Feng, J. J., Li, W. F., Wu, H., Lu, J. L., Liao, W. L., & Luo, X. Q. (2014). Investigation on pressure fluctuation in a Francis turbine with improvement measures. *IOP Conference Series: Earth and Environmental Science, 22*(3), 032006.

Fernholz, H. H., & Finleyt, P. J. (1996). The incompressible zero-pressure-gradient turbulent boundary layer: An assessment of the data. *Progress in Aerospace Sciences, 32*(4), 245-311. doi:https://doi.org/10.1016/0376-0421(95)00007-0

Fontanals, A., Guardo, A., Zobeiri, A., Egusquiza, E., Farhat, M., & Avellan, F. (2014). Boundary layer effects on the vortex shedding in a Donaldson- type hydrofoil. *IOP Conference Series: Earth and Environmental Science, 22*(3), 032045.

Gavrilov, A. A., Sentyabov, A. V., Dekterev, A. A., & Hanjalić, K. (2017). Vortical structures and pressure pulsations in draft tube of a Francis-99 turbine at part load: RANS and hybrid RANS/LES analysis. *International Journal of Heat and Fluid Flow, 63*, 158-171. doi:https://doi.org/10.1016/j.ijheatfluidflow.2016.05.007

Geng, J., Yuan, X.-l., Li, D., & Du, G.-s. (2017). Simulation of cavitation induced by water hammer. *Journal of Hydrodynamics, Ser. B, 29*(6), 972-978. doi:https://doi.org/10.1016/S1001-6058(16)60811-9

Gong, R.-z., Trivedi, C., Dahlhaug, O. G., & Nielsen, T. K. (2017). Blade passage modeling strategy for hydraulic turbine. *International Journal of Fluid Machinery and Systems, 10*(4), 345-354. doi:10.5293/ijfms.2017.10.4.345

Gong, R.-Z., Wang, H.-J., Liu, Q.-Z., Shu, L.-F., & Li, F.-C. (2013). Numerical simulation and rotor dynamic stability analysis on a large hydraulic turbine. *Computers & Fluids, 88*, 11-18. doi:https://doi.org/10.1016/j.compfluid.2013.08.014

Goyal, R., & Gandhi, B. K. (2018). Review of hydrodynamics instabilities in Francis turbine during off-design and transient operations. *Renewable Energy, 116*, 697-709. doi:https://doi.org/10.1016/j.renene.2017.10.012

Halstead, D. E., Wisler, D. C., Okiishi, T. H., Walker, G. J., Hodson, H. P., & Shin, H. W. (1997a). Boundary Layer Development in Axial Compressors and Turbines: Part 1 of 4—Composite Picture. *Journal of Turbomachinery, 119*(1), 114-127. doi:10.1115/1.2841000

Halstead, D. E., Wisler, D. C., Okiishi, T. H., Walker, G. J., Hodson, H. P., & Shin, H. W. (1997b). Boundary Layer Development in Axial Compressors and Turbines: Part 2 of 4—Compressors. *Journal of Turbomachinery, 119*(3), 426-444. doi:10.1115/1.2841142

Halstead, D. E., Wisler, D. C., Okiishi, T. H., Walker, G. J., Hodson, H. P., & Shin, H. W. (1997c). Boundary Layer Development in Axial Compressors and Turbines: Part 3 of 4—LP Turbines. *Journal of Turbomachinery, 119*(2), 225-237. doi:10.1115/1.2841105

Halstead, D. E., Wisler, D. C., Okiishi, T. H., Walker, G. J., Hodson, H. P., & Shin, H. W. (1997d). Boundary Layer Development in Axial Compressors and Turbines: Part 4 of 4—Computations and Analyses. *Journal of Turbomachinery, 119*(1), 128-139. doi:10.1115/1.2841001

Hink, R. (2015). Validation of the k–ω turbulence model for the thermal boundary layer profile of effusive cooled walls. *CEAS Space Journal, 7*(3), 389-398. doi:10.1007/s12567-015-0089-x

Hirsch, C. (2007). *Numerical Computation of Internal and External Flows: The Fundamentals of Computational Fluid Dynamics* (Vol. 1): Butterworth-Heinemann.

Hoskoti, L., Misra, A., & Sucheendran, M. M. (2018). Frequency lock-in during vortex induced vibration of a rotating blade. *Journal of Fluids and Structures, 80*, 145-164. doi:https://doi.org/10.1016/j.jfluidstructs.2018.03.011

Kachanov, Y. S. (1994). Physical Mechanisms of Laminar-Boundary-Layer Transition. *Annual Review of Fluid Mechanics, 26*(1), 411-482. doi:10.1146/annurev.fl.26.010194.002211

Kocak, E., Karaaslan, S., Yucel, N., & Arundas, F. (2017). A Numerical Case Study: Bovet Approach to Design a Francis Turbine Runner. *Energy Procedia, 111*, 885-894. doi:https://doi.org/10.1016/j.egypro.2017.03.251

Kovenya, V., Cherny, S., Sharov, S., Karamyshev, V., & Lebedev, A. (2001). On some approaches to solve CFD problems. *Computers & Fluids, 30*(7), 903-916. doi:https://doi.org/10.1016/S0045-7930(01)00034-2

Krappel, T., Ruprecht, A., & Riedelbauch, S. (2013, 2013//). *Flow Simulation of a Francis Turbine Using the SAS Turbulence Model.* Paper presented at the High Performance Computing in Science and Engineering ‘13, Cham.

Krappel, T., Ruprecht, A., Riedelbauch, S., Jester-Zuerker, R., & Jung, A. (2014). Investigation of Francis Turbine Part Load Instabilities using Flow Simulations with a Hybrid RANS-LES Turbulence Model. *IOP Conference Series: Earth and Environmental Science, 22*(3), 032001.

Kujansuu, U. (2017). *Implementation of a One-equation Local Correlation-Based Transition Model.* (Master), Aalto University,

Laín, S., García, M. J., Quintero, B., & Orrego, S. (2013). CFD Numerical simulations of Francis turbines. *Revista Facultad de Ingeniería; No 51 (2010): Revista Facultad de Ingeniería*.

Langtry, R. B. (2006). *A correlation-based transition model using local variables for unstructured parallelized CFD codes.* (Dr.–Ing Thesis), University of Stuttgart,

Langtry, R. B., & Menter, F. R. (2009). Correlation-Based Transition Modeling for Unstructured Parallelized Computational Fluid Dynamics Codes. *AIAA Journal, 47*(12), 2894-2906. doi:10.2514/1.42362

Langtry, R. B., Menter, F. R., Likki, S. R., Suzen, Y. B., Huang, P. G., & Völker, S. (2004). A Correlation-Based Transition Model Using Local Variables—Part II: Test Cases and Industrial Applications. *Journal of Turbomachinery, 128*(3), 423-434. doi:10.1115/1.2184353

Lardeau, S., Leschziner, M., & Zaki, T. (2012). Large Eddy Simulation of Transitional Separated Flow over a Flat Plate and a Compressor Blade. *Flow, Turbulence and Combustion, 88*(1), 19-44. doi:10.1007/s10494-011-9353-0

Lee, S.-J., Lee, J.-H., & Suh, J.-C. (2015a). Further validation of the hybrid particle-mesh method for vortex shedding flow simulations. *International Journal of Naval Architecture and Ocean Engineering, 7*(6), 1034-1043. doi:https://doi.org/10.1515/ijnaoe-2015-0072

Lee, S.-J., Lee, J.-H., & Suh, J.-C. (2015b). Numerical Investigation on Vortex Shedding from a Hydrofoil with a Beveled Trailing Edge. *Modelling and Simulation in Engineering, 10.1155/2015/565417*, 13.

Magnan, R., Cupillard, S., Gauthier, G., Giroux, A. M., Page, M., & Deschênes, C. (2014). Challenges in assessing the grid sensitivity of hydro-turbine CFD simulations. *IOP Conference Series: Earth and Environmental Science, 22*(2), 022010.

Marusic, I., Monty, J. P., Hultmark, M., & Smits, A. J. (2013). On the logarithmic region in wall turbulence. *Journal of Fluid Mechanics, 716*, R3. doi:DOI: 10.1017/jfm.2012.511

Maruzewski, P., Hayashi, H., Munch, C., Yamaishi, K., Hashii, T., Mombelli, H. P., . . . Avellan, F. (2010). Turbulence modeling for Francis turbine water passages simulation. *IOP Conference Series: Earth and Environmental Science, 12*(1), 012070.

Mayle, R. E. (1991). The Role of Laminar-Turbulent Transition in Gas Turbine Engines. *113*, 509-537. doi:10.1115/91-gt-261

Medic, G., Zhang, V., Wang, G., Joo, J., & Sharma, O. P. (2016). Prediction of Transition and Losses in Compressor Cascades Using Large-Eddy Simulation. *Journal of Turbomachinery, 138*(12), 121001-121001-121009. doi:10.1115/1.4033514

Mehdizadeh, A., Foroutan, H., Vijayakumar, G., & Sadiki, A. (2014). A new formulation of scale-adaptive simulation approach to predict complex wall-bounded shear flows. *Journal of Turbulence, 15*(10), 629-649. doi:10.1080/14685248.2014.927580

Menezes, P. H. B. (2016). Studies on hydrodynamic torque on guide vanes of Francis turbines under steady state operation. *Revista Interdisciplinar de Pesquisa em Engenharia - RIPE, 2*(4).

Menter, F. R. (1994). Two-equation eddy-viscosity turbulence models for engineering applications. *AIAA Journal, 32*(8), 1598-1605. doi:10.2514/3.12149

Menter, F. R., & Egorov, Y. (2010). The Scale-Adaptive Simulation Method for Unsteady Turbulent Flow Predictions. Part 1: Theory and Model Description. *Flow, Turbulence and Combustion, 85*(1), 113-138. doi:10.1007/s10494-010-9264-5

Menter, F. R., Langtry, R. B., Likki, S. R., Suzen, Y. B., Huang, P. G., & Völker, S. (2004). A Correlation-Based Transition Model Using Local Variables—Part I: Model Formulation. *Journal of Turbomachinery, 128*(3), 413-422. doi:10.1115/1.2184352

Minakov, A. V., Platonov, D. V., Dekterev, A. A., Sentyabov, A. V., & Zakharov, A. V. (2015). The analysis of unsteady flow structure and low frequency pressure pulsations in the high-head Francis turbines. *International Journal of Heat and Fluid Flow, 53*, 183-194. doi:https://doi.org/10.1016/j.ijheatfluidflow.2015.04.001

Moukalled, F., Mangani, L., & Darwish, M. (2016). The Finite Volume Method In Computational Fluid Dynamics. *Springer International Publishing*(113). doi:10.1007/978-3-319-16874-6

NASA. (2019). Turbulence modeling resource. Retrieved from https://turbmodels.larc.nasa.gov/

Naudascher, E., & Rockwell, D. (1994). *Flow-Induced Vibrations: An Engineering Guide.* (Vol. 282): Blakema publishers, Cambridge University Press.

Noriega, H., Guibault, F., Reggio, M., & Magnan, R. (2018a). A case-study in open-source CFD code verification, Part I: Convergence rate loss diagnosis. *Mathematics and Computers in Simulation, 147*, 152-171. doi:https://doi.org/10.1016/j.matcom.2017.12.002

Noriega, H., Guibault, F., Reggio, M., & Magnan, R. (2018b). A case-study in open-source CFD code verification. Part II: Boundary condition non-orthogonal correction. *Mathematics and Computers in Simulation, 147*, 172-193. doi:https://doi.org/10.1016/j.matcom.2017.12.001

Okuducu, M. B., & Aral, M. M. (2018). Performance Analysis and Numerical Evaluation of Mixing in 3-D T-Shape Passive Micromixers. *Micromachines, 9*(5), 210. doi:10.3390/mi9050210

Petit, O. (2012). *Towards Full Predictions of the Unsteady Incompressible Flow in Rotating Machines, Using OpenFOAM*. (Doctor of Philosophy), Chalmers University of Technology, Gothenburg, Sweden.

Qian, Z.-d., Yang, J.-d., & Huai, W.-x. (2007). Numerical simulation and analysis of pressure pulsation in francis hydraulic turbine with air admission. *Journal of Hydrodynamics, Ser. B, 19*(4), 467-472. doi:https://doi.org/10.1016/S1001-6058(07)60141-3

Reshotko, E. (2001). Transient growth: A factor in bypass transition. *Physics of Fluids, 13*(5), 1067-1075. doi:10.1063/1.1358308

Rockwell, D. (1998). Vortex-body Interactions. *Annual Review of Fluid Mechanics, 30*(1), 199-229. doi:10.1146/annurev.fluid.30.1.199

Rotta, J. C. (1972). *Turbulente Strömungen* Stuttgart: BG Teubner.

Saeed, R. A. (2015). Numerical Simulation of Three-Dimensional Cavitating Turbulent Flow in Francis Turbines with ANSYS. *International Journal of Mechanical, Aerospace, Industrial, Mechatronic and Manufacturing Engineering, 9*, 1572-1578.

Saeed, R. A., Galybin, A. N., & Popov, V. (2010). Modelling of flow-induced stresses in a Francis turbine runner. *Advances in Engineering Software, 41*(12), 1245-1255. doi:https://doi.org/10.1016/j.advengsoft.2010.09.001

Sarpkaya, T. (2004). A critical review of the intrinsic nature of vortex-induced vibrations. *Journal of Fluids and Structures, 19*(4), 389-447. doi:https://doi.org/10.1016/j.jfluidstructs.2004.02.005

Schilling, R. A. (2009). *Numerical simulation of pressure oscillations in Francis turbine runners*. Paper presented at the Numerical Simulation in Turbomachinery, , St. Petersburg.

Schlichting, H., & Gersten, K. (1979). *Boundary layer theory*. McGraw-Hill.: McGraw-Hill Series in Mechanical Engineering.

Schubauer, G. B., & Klebanoff, P. (1956). Contributions on the mechanics of boundary-layer transition.

Schultz, M. P., Finlay, J. A., Callow, M. E., & Callow, J. A. (2003). Three Models to Relate Detachment of Low Form Fouling at Laboratory and Ship Scale. *Biofouling, 19*(sup1), 17-26. doi:10.1080/0892701031000089516

Sheng, C. (2016). *Advances in Transitional Flow Modeling: Applications to Helicopter Rotors*: Springer International Publishing.

Sheng, C. (2017). Transition Prediction. In C. Sheng (Ed.), *Advances in Transitional Flow Modeling: Applications to Helicopter Rotors* (pp. 9-19). Cham: Springer International Publishing.

Shi, Q. H., Xu, W. W., & Gong, L. (2008). *Noise reduction in a low head Francis turbine caused by runner inter-blade vortices*.

Smith, A. M. O., & Gamberoni, N. (1956). *Transition, Pressure Gradient and Stability Theory*. El Segundo, California: Douglas Aircraft Company.

Sosa, J. B., Urquiza, G., García, J. C., & Castro, L. L. (2015). Computational fluid dynamics simulation and geometric design of hydraulic turbine draft tube. *Advances in Mechanical Engineering, 7*(10). doi:10.1177/1687814015606307

Squire, L. C. (1991). Boundary Layers. By A. D. YOUNG. BSP Professional Books, 1989. 269 pp. £16.95. *Journal of Fluid Mechanics, 226*, 656-657. doi:10.1017/S0022112091222557

Stefan, D., & Rudolf, P. (2015). Proper Orthogonal Decomposition of Pressure Fields in a Draft Tube Cone of the Francis (Tokke) Turbine Model. *Journal of Physics: Conference Series, 579*(1), 012002.

Stoessel, L., & Nilsson, H. (2015). Steady and unsteady numerical simulations of the flow in the Tokke Francis turbine model, at three operating conditions. *Journal of Physics: Conference Series, 579*(1), 012011.

Suzen, Y. B., Huang, P. G., Hultgren, L. S., & Ashpis, D. E. (2003). Predictions of Separated and Transitional Boundary Layers Under Low-Pressure Turbine Airfoil Conditions Using an Intermittency Transport Equation. *Journal of Turbomachinery, 125*(3), 455-464. doi:10.1115/1.1580159

Sweby, P. K. (1984). High resolution schemes using flux limiters for hyperbolic conservation laws. *SIAM journal on numerical analysis, 21*(5), 995–1011. doi:https://doi.org/10.1137/0721062

Teran, L. A., Larrahondo, F. J., & Rodríguez, S. A. (2016). Performance improvement of a 500-kW Francis turbine based on CFD. *Renewable Energy, 96*, 977-992. doi:https://doi.org/10.1016/j.renene.2016.05.044

Trivedi, C. (2015). *Investigations of Transient Pressure Loading on a High Head Francis Turbine.* (Doctoral thesis, comprehensive summary), Luleå tekniska universitet, DiVA database.

Tysell, L. (2010). *Hybrid grid generation for viscous flow computations around complex geometries.* Royal Institute of Technology, Stockholm, Sweden.

van Leer, B. (1973, 1973//). *Towards the ultimate conservative difference scheme I. The quest of monotonicity.* Paper presented at the Proceedings of the Third International Conference on Numerical Methods in Fluid Mechanics, Berlin, Heidelberg.

Versteeg, H., & Malalasekera, W. (2007). *An Introduction to Computational Fluid Dynamics*: Prentice Hall

Volino, R. J., & Hultgren, L. S. (2000). Measurements in Separated and Transitional Boundary Layers Under Low-Pressure Turbine Airfoil Conditions. *Journal of Turbomachinery, 123*(2), 189-197. doi:10.1115/1.1350408

Vu, T. C., Nennemann, B., Ausoni, P., Farhat, M., & Avellan, F. (2007). *Unsteady CFD Prediction of von Kármán Vortex Shedding in Hydraulic Turbine Stay Vanes*. Paper presented at the Hydro, Granada, Spain.

Walker, G. J. (1993). The Role of Laminar-Turbulent Transition in Gas Turbine Engines: A Discussion. *Journal of Turbomachinery, 115*(2), 207-216. doi:10.1115/1.2929223

Walters, D. K., & Cokljat, D. (2008). A Three-Equation Eddy-Viscosity Model for Reynolds-Averaged Navier–Stokes Simulations of Transitional Flow. *Journal of Fluids Engineering, 130*(12). doi:10.1115/1.2979230

Wang, J., & Sheng, C. (2014). Validations of a Local Correlation-Based Transition Model Using an Unstructured Grid CFD Solver. In *7th AIAA Theoretical Fluid Mechanics Conference*: American Institute of Aeronautics and Astronautics.

Wang, J., & Sheng, C. (2015). A Comparison of a Local Correlation-Based Transition Model Coupled with SA and SST Turbulence Models. In *53rd AIAA Aerospace Sciences Meeting*: American Institute of Aeronautics and Astronautics.

Weyburne, D. W. (2006). A mathematical description of the fluid boundary layer. *Applied Mathematics and Computation, 175*(2), 1675-1684. doi:https://doi.org/10.1016/j.amc.2005.09.012

Weyburne, D. W. (2016). Schematic drawing of a boundary layer created by fluid flowing over a flat plate. Retrieved from https://upload.wikimedia.org/wikipedia/commons/8/85/Wickipedia_Picture_Boundary_Layer_Thickness.jpg

Wheeler, A. P. S., Sandberg, R. D., Sandham, N. D., Pichler, R., Michelassi, V., & Laskowski, G. (2016). Direct Numerical Simulations of a High-Pressure Turbine Vane. *Journal of Turbomachinery, 138*(7), 071003-071003-071009. doi:10.1115/1.4032435

White, F. M., & Corfield, I. (2006). *Viscous fluid flow* (Vol. 3): McGraw-Hill New York.

Wilcox, D. C. (1994). *Turbulence Modeling for CFD*: DCW Industries, Inc. La Canada, California.

Williamson, C. H. K., & Govardhan, R. (2004). Vortex-induced vibrations. *Annual Review of Fluid Mechanics, 36*(1), 413-455. doi:10.1146/annurev.fluid.36.050802.122128

Yao, Z., Wang, F., Dreyer, M., & Farhat, M. (2014). Effect of trailing edge shape on hydrodynamic damping for a hydrofoil. *Journal of Fluids and Structures, 51*, 189-198. doi:https://doi.org/10.1016/j.jfluidstructs.2014.09.003

You, J. Y., & Kwon, O. J. (2012). Numerical assessment of turbulent models at a critical regime on unstructured meshes. *Journal of Mechanical Science and Technology, 26*(5), 1363-1369. doi:10.1007/s12206-012-0319-5

You, J. Y., & Kwon, O. J. (2013). Blending of SAS and correlation-based transition models for flow simulation at supercritical Reynolds numbers. *Computers & Fluids, 80*, 63-70. doi:https://doi.org/10.1016/j.compfluid.2012.05.016

Zaki, T. A. (2013). From Streaks to Spots and on to Turbulence: Exploring the Dynamics of Boundary Layer Transition. *Flow, Turbulence and Combustion, 91*(3), 451-473. doi:10.1007/s10494-013-9502-8

Zaki, T. A., & Durbin, P. A. (2005). Mode interaction and the bypass route to transition. *Journal of Fluid Mechanics, 531*, 85-111. doi:10.1017/s0022112005003800

Zhang, Y., Chen, T., Li, J., & Yu, J. (2017). Experimental Study of Load Variations on Pressure Fluctuations in a Prototype Reversible Pump Turbine in Generating Mode. *Journal of Fluids Engineering, 139*(7), 074501-074501-074504. doi:10.1115/1.4036161

Zhang, Y., Liu, K., Xian, H., & Du, X. (2018). A review of methods for vortex identification in hydroturbines. *Renewable and Sustainable Energy Reviews, 81*, 1269-1285. doi:https://doi.org/10.1016/j.rser.2017.05.058

Zhang, Y., Qian, Z., Ji, B., & Wu, Y. (2016). A review of microscopic interactions between cavitation bubbles and particles in silt-laden flow. *Renewable and Sustainable Energy Reviews, 56*, 303-318. doi:https://doi.org/10.1016/j.rser.2015.11.052

Zobeiri, A. (2012). *Effect of Hydrofoil Trailing Edge Geometry on the Wake Dynamics.* (Ph.D. Theses, Lausanne), EPFL,

Zobeiri, A., Ausoni, P., Avellan, F., & Farhat, M. (2012). How oblique trailing edge of a hydrofoil reduces the vortex-induced vibration. *Journal of Fluids and Structures, 32*, 78-89. doi:https://doi.org/10.1016/j.jfluidstructs.2011.12.003

APPENDIX A – DISCRETIZATION

In this Appendix, the spatial discretization effects on the shedding frequency computation is presented. The outcome of the discretization analysis was used to investigate the effect of a transitional turbulence model. The transitional model was implemented in combination with the SST-SAS turbulence model by taking advantage of the OpenFOAM-1706 open source CFD tool.

Grid analysis

A mesh convergence study is desired to investigate the discretization effect on the CFD solution. Taking advantage of the robust and automatic inhouse meshing tool, a thoroughly customized grid can be constructed on the geometry by specifying user defined parameters. The parameters available to control the grid generation procedure are the element size in the core flow, the height of the first element of the boundary layer, the number of elements tangential to the hydrofoil and the boundary layer skin ratio.

Mesh resolution

Due to the shape of the truncated hydrofoil, a vortex street appears in the wake of the foil. So, it is necessary to have fine meshes in this region to capture the phenomenon. Using the Vane-mesh tool, concentration and size of the elements in the wake region can be managed by defining specific circular zones identified by their locations, radius and their interior mesh size. The element size at inlet and far field regions can also be easily set with the Vane-mesh environment. Figure A.1 presents an example of a pattern of circular zone to control mesh density at the trailing edge.

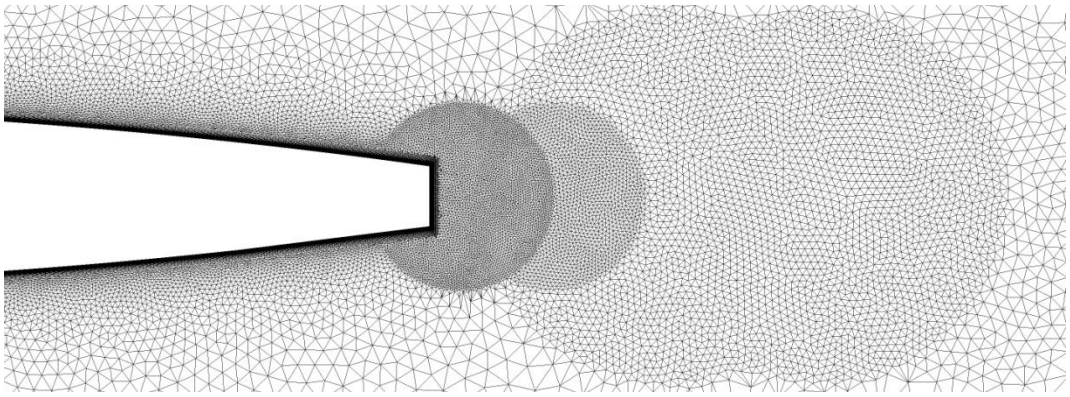

Figure A.1 Increasing mesh density at the trailing edge using the Vane-mesh meshing tool

The hybrid mesh includes hexahedral elements in the boundary layer region and tetrahedral elements in the core flow. Mesh convergence study is performed by dividing the element size in half in the boundary layer (only tangential elements to the foil) and in the core flow. This approach is approximately equal to the usual mesh doubling procedure.

At this stage, the distances of the first node next to the hydrofoil and boundary layer skin thickness were kept constant for all mesh resolution levels in order to keep an absolute control on the y^+ value for all mesh densities. All meshes generated have near wall resolution of $y^+ < 1$. Figure A.2 shows the mesh refinement effect on the frequency calculation using the SST and SST-SAS turbulence models. It is noted that the mesh resolution plays an important role in the CFD computation. The mesh elements need to be fine enough in order to resolve the flow properties. However, comparing the results from mesh resolution study to experimental data indicates that there is still a considerable difference (17% difference using the SST-SAS turbulence model) in terms of fluctuation frequency. As shown in Fig A.2, when using the SST turbulence model for all meshes, the computed frequency is under predicted compared to the SST-SAS model. The finest mesh with more than 1.2 million elements predicts slightly (less than 0.5% difference) higher frequency than the second finest mesh. This is while computational time for the finest mesh is much higher than the second finest mesh. The mesh with the second highest element count and the SAS-SST turbulence model are selected for further boundary layer mesh analysis.

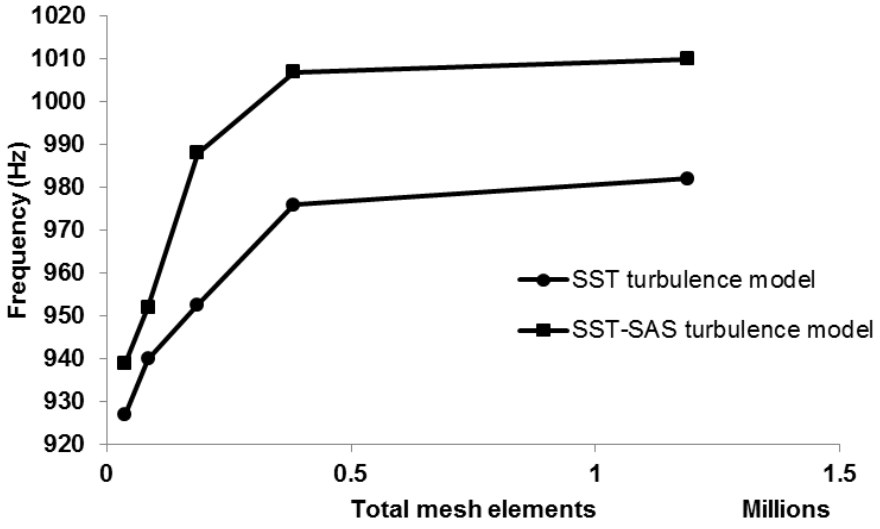

Figure A.2 Mesh resolution effect on frequency calculation

Tangential elements on the hydrofoil

According to experimental studies of Ausoni (2009) and Zobeiri (2012), water flow over the considered NACA0009 hydrofoil with inlet velocity of 17 m/s presents a transitional behaviour. It is desired to investigate the boundary layer mesh parameters from which the transitional flow initiates. Fluctuating lift forces are applied normal to the flow direction on the hydrofoil surface. A boundary layer mesh parameter that can be analyzed, is the number of elements tangential to the hydrofoil, using the SST-SAS turbulence model.

Figure A.3 presents the mesh distribution for different number of tangential elements in boundary layer skin while keeping all other properties constant. Figure A.4 presents the corresponding computed frequency. It shows that increasing the number of mesh elements on the hydrofoil will not result in a considerable difference in terms of frequency calculation. Thus, a mesh with 1200 elements was selected as the reference value for this study.

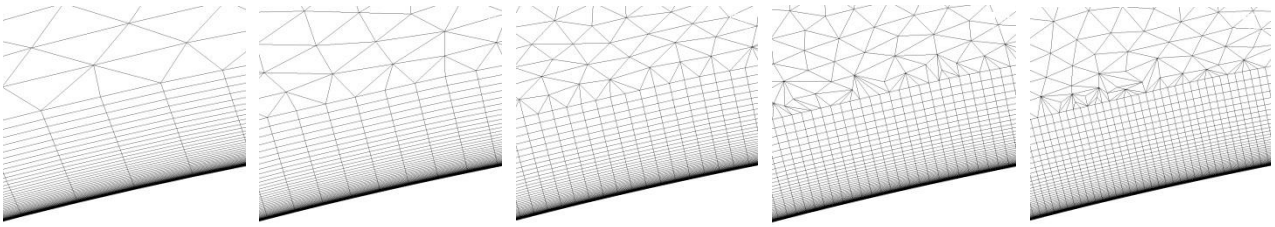

a) 300 elements b) 600 elements c) 1200 elements d) 1800 elements e) 2400 elements

Figure A.3 Tangential elements in boundary layer mesh

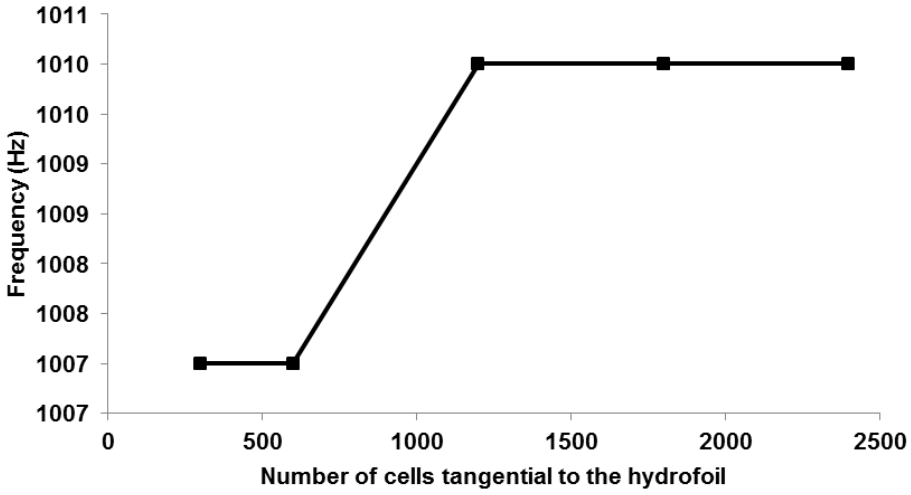

Figure A.4 Effect of number of cells tangential to the foil on frequency calculation

First cell height

The SST-SAS turbulence model is used without wall function treatment in order to investigate the boundary layer mesh effect on shedding frequency calculations. It is suggested to have a mesh with $y^+ \approx 1$ when using the SST-SAS model resolving the boundary layer (Egorov, Menter, Lechner, & Cokljat, 2010). Figure A.5 shows the variation of the computed frequency as a function of the first cell height. Results show that the higher the element size the lower the frequency, until it reaches a plateau region where there is no frequency change.

Figure A.6 presents the average y^+ for different first cell heights. Decreasing the first cell height results in a lower average y^+. Based on the results, a first cell with a height of 0.000025 m, which results in an average y^+ less than 0.2 is selected for further mesh analysis. There is less than 0.5% difference between the frequency of the selected first cell height and the one for minimum first cell height.

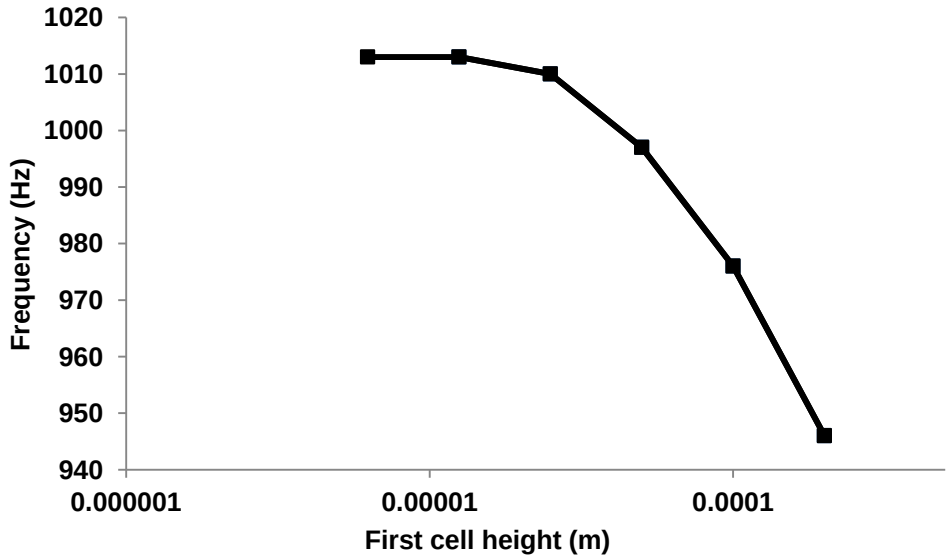

Figure A.5 First cell height size effect on oscillation frequency

Figure A.7 shows y^+ on the NACA hydrofoil with the first cell height of 0.000025 m. As indicated, the maximum y^+ value is close to 0.2 and the average y^+ is near 0.1.

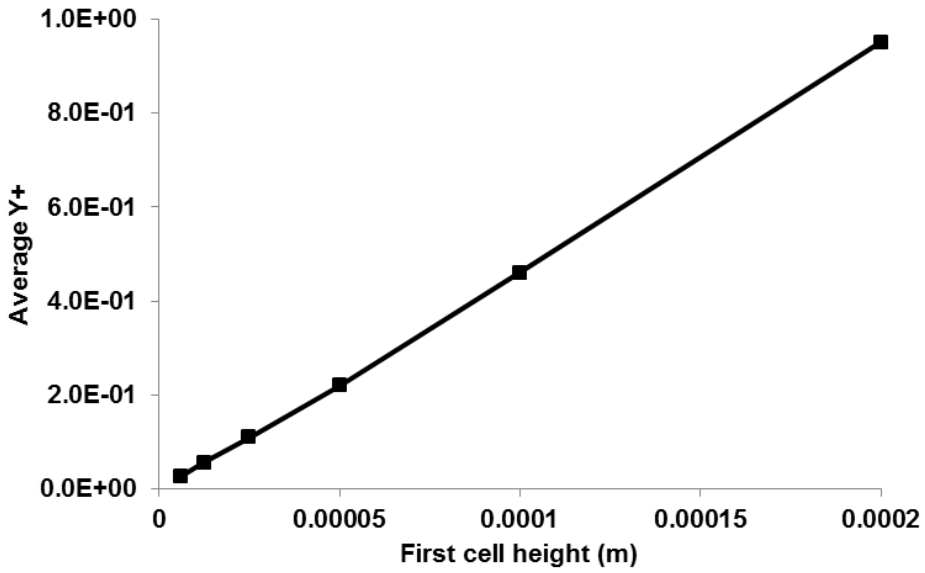

Figure A.6 Average y^+ for different first cell height

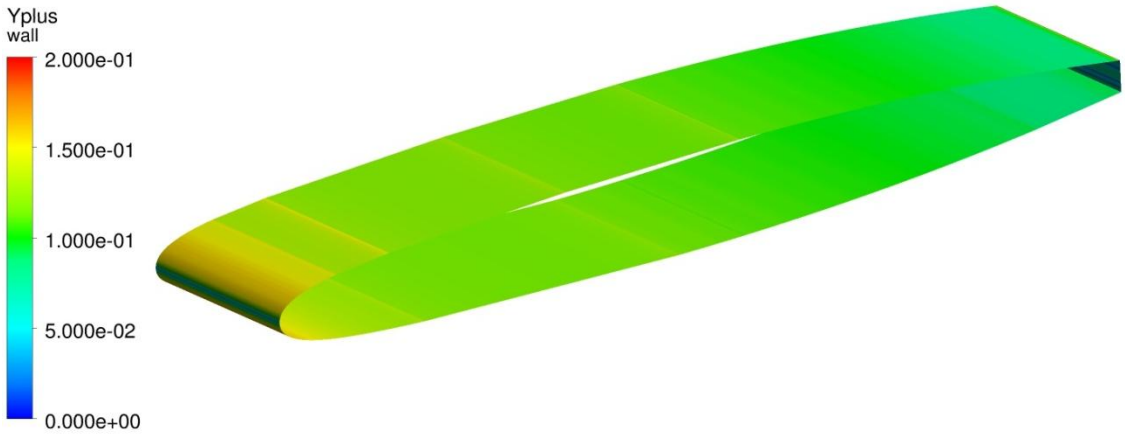

Figure A.7 y^+ on the foil with the first cell height of 0.000025 m

Skin thickness

The variation of the skin thickness ratio near the wall region is evaluated in this section. Vane-Mesh meshing tool provides a projection method that scales the geometry by a user defined ratio around the body to create the boundary layer mesh. Figure A.8 presents the meshes generated for various skin thicknesses while keeping the first cell size constant at 0.000025 m, and the mesh expansion ratio at 1.1.

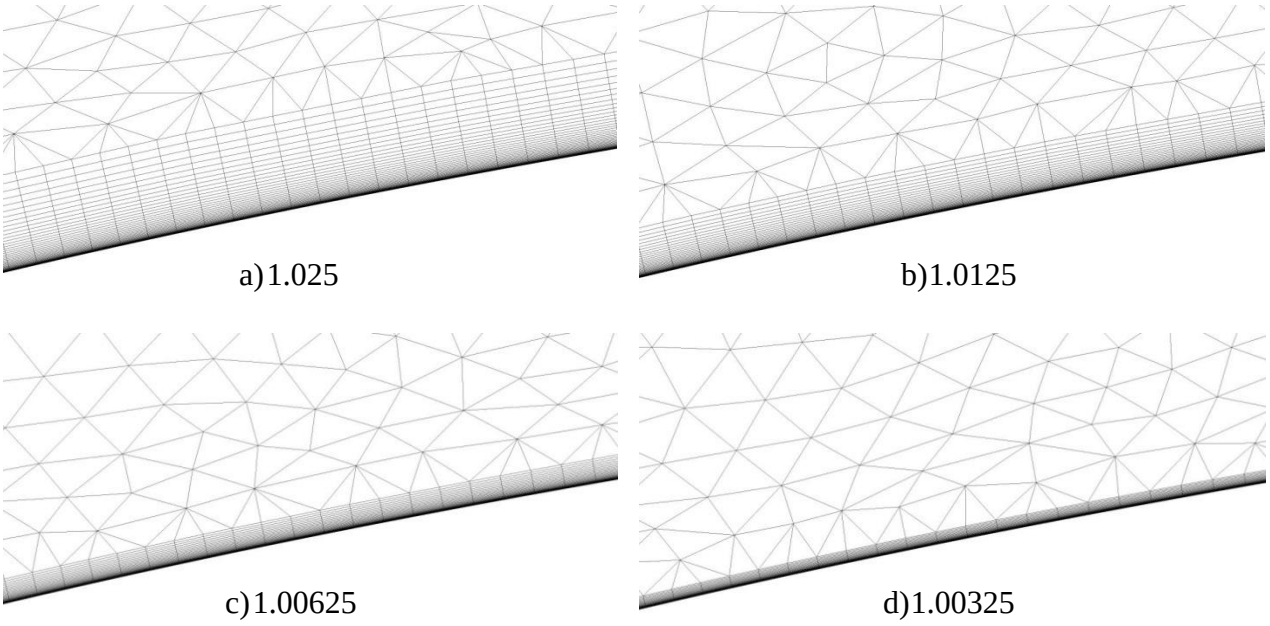

Figure A.8 Skin thickness mesh

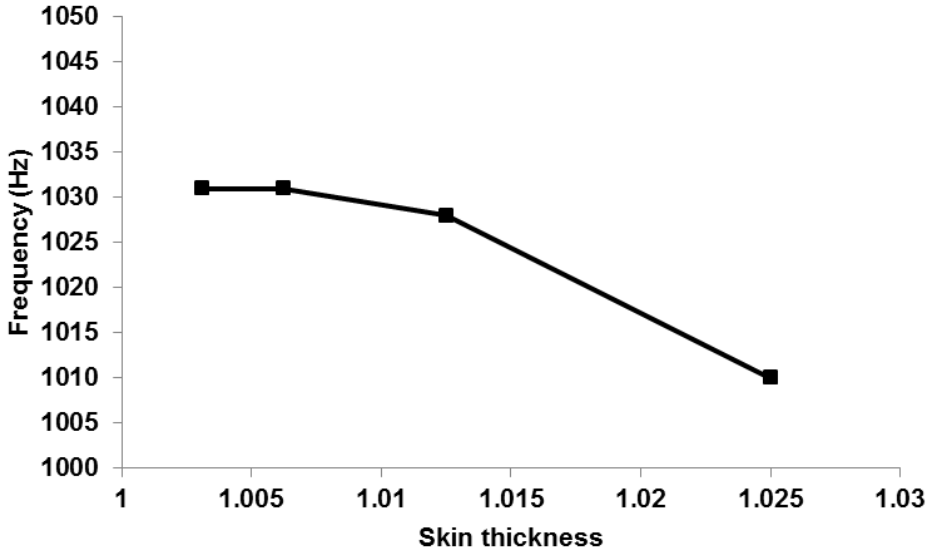

Figure A.9 Vibration frequency and various skin thickness ratio

Figure A.9 shows the frequency calculated with various skin thicknesses corresponding to the Fig. A.8. Decreasing the skin thickness ratio results in a higher frequency; however, this effect diminishes for smaller skin thickness. The skin ratio of 1.0125 is selected for the current study.

Summary

A thorough mesh study using hybrid meshes was carried out on the NACA0009 hydrofoil focussed on the mesh effect in terms of shedding frequency calculation. The findings are summarized as follows:

- The number of mesh elements tangential to the hydrofoil does not present a strong influence in terms of frequency calculation and mesh with 1200 elements tangential to the foil is selected as the reference value.
- The first element size shows a considerable effect in frequency calculation. The smaller the element size the higher the frequency, until it reaches a plateau region where there is no change in frequency due to the first cell height size. Based on the results, a first cell with a height of 0.000025 m, which results in an average y^+ less than 0.2 is selected.
- Decreasing the skin thickness ratio results in a higher frequency; however, this effect decreases for smaller skin thickness. The skin ratio of 1.0125 is selected for the current study.

Results show that boundary layer mesh could be an influential parameter on the accuracy of the simulation. However, there remains a considerable difference between numerical results and experimental data. In chapter 3, the influence of the transitional model was investigated in combination with the SST-SAS turbulence model.